



THE HONG KONG  
POLYTECHNIC UNIVERSITY

香港理工大學

Pao Yue-kong Library

包玉剛圖書館

---

## Copyright Undertaking

This thesis is protected by copyright, with all rights reserved.

**By reading and using the thesis, the reader understands and agrees to the following terms:**

1. The reader will abide by the rules and legal ordinances governing copyright regarding the use of the thesis.
2. The reader will use the thesis for the purpose of research or private study only and not for distribution or further reproduction or any other purpose.
3. The reader agrees to indemnify and hold the University harmless from and against any loss, damage, cost, liability or expenses arising from copyright infringement or unauthorized usage.

### IMPORTANT

If you have reasons to believe that any materials in this thesis are deemed not suitable to be distributed in this form, or a copyright owner having difficulty with the material being included in our database, please contact [lbsys@polyu.edu.hk](mailto:lbsys@polyu.edu.hk) providing details. The Library will look into your claim and consider taking remedial action upon receipt of the written requests.

**MECHANISMS OF PHASE  
TRANSFORMATIONS IN ALUMINUM  
ANODES FOR LITHIUM-BASED BATTERIES**

**ZHENG TIANYE**

**PhD**

**The Hong Kong Polytechnic University**

**2021**

**The Hong Kong Polytechnic University**

**Department of Electrical Engineering**

**Mechanisms of Phase Transformations in  
Aluminum Anodes for Lithium-based Batteries**

**Zheng Tianye**

**A thesis submitted in partial fulfilment of the  
requirements for the degree of Doctor of Philosophy**

**November 2020**

# CERTIFICATE OF ORIGINALITY

I hereby declare that this thesis is my own work and that, to the best of my knowledge and belief, it reproduces no material previously published or written, nor material that has been accepted for the award of any other degree or diploma, except where due acknowledgement has been made in the text.

\_\_\_\_\_ (Signed)

ZHENG Tianye (Darren) \_\_\_\_\_ (Name of student)

## Acknowledgements

I would not have been completed my Ph.D. project smoothly and successfully without help from various parties. Here I would like to express my gratitude to the Hong Kong Polytechnic University (PolyU) and Karlsruhe Institute of Technology (KIT), Germany for providing me world-leading platforms in conducting scientific research.

First and foremost, I am and will always be thankful to Dr. Steven Boles from PolyU, not only for his guidance, support, and inspiration as a supervisor, but also for his respect, kindness, and generosity as a friend. Along my Ph.D. journey, my academic skills and critical thinking are significantly improved with his instructions. Importantly, he has influenced me on how to become a better person. Moreover, I am grateful to our long-term allies, Dr. Holger Geßwein, Dr. Dominik Kramer, and Dr. Reiner Mönig from KIT for offering me a great opportunity to conduct research in their lab. I was impressed by their working style and way of thinking. The half-year residence in Germany has enriched my life experience.

Many thanks to my dear colleagues: Dr. Bei Li and Ms. Sijia Ran for guiding me through the school/lab equipment, especially at the early stage of my study, and for their encouragement and friendship. Also, it was my honor to work with Dr. Mohammad Tahmasebi, Dr. Glen Tom, and Dr. Virag Raut who are nice, creative, and always willing to offer help, creating a unique and international atmosphere in our research group. I would like to acknowledge our collaborator, Mr. Xiaogang Wang, Ms. Ekta Jain, and Dr. Matteo Seita from Nanyang Technological University (NTU), Singapore as well.

Last but not least, as the only child in my family, I do appreciate the unconditional love from my dear parents Dr. Shuguo Zheng and Mrs. Hongjun Zhang. They are always on my side no matter what happens. I am also thankful to my fiancée Ms. Can Gu who has been accompanying me for twelve years through thick and thin. I am looking forwards to our next twelve years.

## Abstract

Lithium storage in aluminum stems from a phase transformation from lithium-poor  $\alpha$  phase (Al, face-centered cubic) to lithium-rich  $\beta$  phase (LiAl, cubic) at room temperature. The intrinsic properties, such as high capacity, light weight, low cost, and the potential of simplifying the manufacturing processes make Al a competitive anode material in lithium-based batteries. However, utilization of Al-based anodes is still not fully viable at this moment due to the drastic capacity fading during charge and discharge, thus drawing less attention compared to other anode candidates.

In this Ph.D. project, the initial step is to gain fundamental understandings of the  $\alpha$  to  $\beta$  phase transformation through *operando* light microscopy and kinetic analysis. It is visually revealed that nuclei appear at random positions and expand to form quasi-circular patches that grow and merge until the phase transformation is complete. Interestingly, the growth of the quasi-circular patches exhibits anisotropy at the granular level. Together with the electron backscatter diffraction technique, the lithiation of Al is suggested to be a whole-grain process that is influenced by grain textures, and the grain with a preferred out-of-plane  $\langle 111 \rangle$  orientation may inhibit the phase transformation. As for the reversed  $\beta$  to  $\alpha$  transition, the extraction of Li from the  $\beta$  phase is accompanied by fracture and crack formation leading to the detachment of the  $\alpha$  phase from the rest of the electrode. The mechanical stress in Al thin film electrodes shows a strong stress asymmetry during (de-)lithiation.

Then the investigations have been extended towards bulky Al foil electrodes, of which the typical features remain. However, the considerable thickness of foils facilitates a quasi-1D in-depth phase propagation once the surface is fully covered with the  $\beta$ -LiAl. The cross-section of a partly lithiated Al foil exhibits unique features under an electron microscope. Combining with *operando* x-ray diffraction, relevant scientific insights are yielded: 1) plastic deformation zone is characterized next to the  $\beta$ -LiAl, causing an extremely small size of Al grains before

being transformed; 2) significant compression may prevent certain Al regions from being nucleated; 3) delithiation makes Al matrix nanoporous with a neglected volume contraction, thereby accumulating the electrode thickness over cycling.

Lastly, the  $\beta$ -LiAl is found to be the only crystalline phase at room temperature. Li solubility within the  $\beta$  phase is suggested to take over the suspected formation of Li-rich phases beyond the  $\beta$ -LiAl. The solubility range of the  $\beta$  phase is determined to be  $\sim 5$  at% by potentiostatic charge counting experiments. Moreover, the cyclic voltammetry of partially lithiated Al foils shows that the  $\beta$  phase can be (de-)saturated without propagating the phase front towards the  $\alpha$  phase. Through delicate manipulation by solely engaging the solubility range, i.e., preventing the problematic  $\alpha/\beta/\alpha$  phase transformations from occurring, the cycling life of  $\beta$ -LiAl anode can be significantly improved and compete with the state-of-the-art LIB anodes. Not only does this thesis provide fundamental understandings for the  $\beta$ -LiAl phase at room temperature that complements the existing phase diagrams, but also implies that Al foils hold great potential as an anode material for lithium-based energy storage.

## Table of Contents

<b><i>CERTIFICATE OF ORIGINALITY</i></b> .....	<b><i>i</i></b>
<b><i>Acknowledgements</i></b> .....	<b><i>ii</i></b>
<b><i>Abstract</i></b> .....	<b><i>iii</i></b>
<b><i>List of abbreviations</i></b> .....	<b><i>ix</i></b>
<b>1. Introduction</b> .....	<b>10</b>
<b>1.1. Electrical Energy Storage (EES) Technologies</b> .....	<b>10</b>
<b>1.2. Lithium-ion Batteries (LIBs)</b> .....	<b>12</b>
<b>1.3. Anode Material Candidates</b> .....	<b>14</b>
<b>1.3.1 Graphite (C)</b> .....	<b>15</b>
<b>1.3.2 Lithium Titanite Oxide (LTO)</b> .....	<b>16</b>
<b>1.3.3 Silicon (Si)</b> .....	<b>17</b>
<b>1.3.4 Other alloy anodes</b> .....	<b>18</b>
<b>1.4. Utilization of Al-based anodes</b> .....	<b>19</b>
<b>1.4.1 Motivations</b> .....	<b>19</b>
<b>1.4.2 Challenges</b> .....	<b>20</b>
<b>1.4.3 Li-Al phase diagrams</b> .....	<b>20</b>
<b>1.4.4 Li-Al crystal structures</b> .....	<b>22</b>
<b>1.5. Research objectives</b> .....	<b>23</b>
<b>2. Experimental Section</b> .....	<b>25</b>
<b>2.1. Operando light microscopic cell</b> .....	<b>25</b>
<b>2.2. In situ stress cell</b> .....	<b>27</b>
<b>2.3. Operando XRD coin cell</b> .....	<b>28</b>
<b>2.4. Two-electrode beaker cell</b> .....	<b>29</b>
<b>2.5. Swagelok-type cell and coin cell</b> .....	<b>30</b>

2.6.	Electrochemical tests.....	31
2.7.	Material characterizations .....	31
3.	<i>Lithiation mechanisms: kinetic analyses .....</i>	<b>33</b>
3.1.	Background.....	33
3.2.	Results and Discussion .....	35
3.2.1	Stage 1 – Initial Lithiation .....	41
3.2.2	Stage 2 – Electrochemical Nucleation and Initial Growth of the $\beta$ Phase.....	44
3.2.3	Stage 3 and 4 – Stable Growth of the $\beta$ Phase .....	46
3.2.4	Stage 4 – Completing the Phase Transformation.....	50
3.2.5	Expansion Rates of Individual $\beta$ Phase Patches .....	50
3.2.6	Kinetic and Charge Control in Half Cell Experiments .....	53
3.3.	Conclusion.....	55
4.	<i>Lithiation mechanisms: granular phase transformation.....</i>	<b>57</b>
4.1.	Background.....	57
4.2.	Results and Discussion .....	58
4.3.	Conclusion.....	66
5.	<i>Delithiation mechanisms: stress analyses .....</i>	<b>68</b>
5.1.	Background.....	68
5.2.	Results and Discussion .....	69
5.2.1	<i>Operando</i> light microscopy .....	70
5.2.2	<i>In situ</i> stress measurement .....	76
5.3.	Conclusion.....	90
6.	<i>(De-)lithiation mechanisms of bulk foils.....</i>	<b>92</b>
6.1.	Background.....	92
6.2.	Results and Discussion .....	93

6.2.1	<i>Operando</i> XRD for (de-)lithiation cycles .....	93
6.2.2	Initial nucleation of the $\beta$ phase .....	97
6.2.3	Initial propagation of the $\beta$ phase .....	99
6.2.4	Initial delithiation of the $\beta$ phase .....	103
6.2.5	Repetitive cycling of Al foil electrodes.....	105
6.3.	Summary .....	107
7.	<i>Li solubility range of the <math>\beta</math> phase</i> .....	109
7.1.	Background.....	109
7.2.	Characterization by chronoamperometry .....	109
7.3.	Characterization by cyclic voltammetry .....	112
7.4.	Characterization by galvanostatic charge-discharge.....	115
7.5.	Li diffusivity within the $\beta$ phase.....	119
7.6.	Full cell demonstration with the $\beta$ -LiAl anode .....	121
7.7.	Summary .....	123
8.	<i>Conclusions and Outlook</i> .....	125
8.1.	Summary of literature review .....	125
8.2.	Conclusions from experimental results.....	126
8.3.	Outlook and perspectives.....	127
	<i>References</i> .....	131
	<i>Appendix-I: Supporting Information of Chapter 3</i> .....	136
	Supplementary Figures.....	136
	Supplementary Tables .....	143
	Astakhov's equation.....	145
	Avrami Analysis .....	147
	<i>Appendix II – Supporting Information of Chapter 4</i> .....	148

<b>Supplementary Figures.....</b>	<b>148</b>
<b>In-plane orientation and grain boundaries.....</b>	<b>152</b>
<b>Interatomic voids.....</b>	<b>153</b>
<b><i>Appendix III: Supporting Information of Chapter 5 .....</i></b>	<b><i>154</i></b>
<b>Supplementary Figures.....</b>	<b>154</b>
<b>Incremental Capacity Analysis (ICA) .....</b>	<b>158</b>
<b>Coin Cell Demonstration .....</b>	<b>160</b>
<b><i>Appendix IV – Supporting Information of Chapter 7 .....</i></b>	<b><i>161</i></b>
<b>Supplementary Figures.....</b>	<b>161</b>

## List of abbreviations

BSE	Back-scattered Electron
CE	Coulombic Efficiency
CV	Cyclic Voltammetry
DEC	Di-ethyl Carbonate
DMC	Di-methyl Carbonate
EC	Ethylene Carbonate
EV	Electric Vehicles
EES	Electric Energy Storage
EIS	Electrochemical Impedance Spectroscopy
EMC	Ethyl-methyl Carbonate
EBSD	Electron Back-scatter Diffraction
FCC	Face-centered Cubic
GCD	Galvanostatic Charge-Discharge
IPF	Inverse Pole Figure
LIB	Lithium-ion Battery
LTO	Lithium Titanite Oxide ( $\text{Li}_4\text{Ti}_5\text{O}_{12}$ )
PVD	Physical Vapor Deposition
PHEV	Plug-in Hybrid Electric Vehicles
SOC	State of Charge
SE	Secondary Electron
SEI	Solid-Electrolyte Interphase
SEM	Scanning Electron Microscopy
TEM	Transmission Electron Microscopy
XRD	X-ray Diffraction

# 1. Introduction

Utilization of energy plays a crucial role in this modern era, such as transportation means, power plants, and portable electronic devices. However, the fossil fuel-based economy has brought a series of issues to our society. Indeed, nowadays, most places in the world still heavily rely on burning coal to generate electricity, which is then delivered to households via the power grid and to fulfill people's daily use. This burning process always results in severe environmental issues that cannot be easily avoided, like emissions of air pollutants and greenhouse gases. Moreover, the gasoline engine still dominates the vehicle industry at this moment, which is considered as depletion of crude oil is expected at the end of this century. It is, therefore, necessary to exploit other resources to fulfill the energy requirements, especially the world energy consumption is predicted to grow by ~30% in the next 30 years.[1]

Although there are multiple renewable/sustainable energy sources available, such as solar, wind, and hydro powers that are considered as potential alternatives, the instability of these energy sources has always been one of the main challenges that prevent large-scale applications. This situation renders the necessary development of energy storage technologies, allowing a more efficient and feasible handle of these unstable energy sources. In the case of solar energy, excessive sunlight can be stored during the daytime and reused at night. The same concept can also be applied to wind turbines, hydropower, and so forth. Apart from these grid-scale applications, the technology can also be extended to electric vehicles (EVs) or plug-in hybrid electric vehicles (PHEVs), which are considered as the primary alternatives to replace the vehicles with gasoline engines soon. Lastly, people may expect long hours of use for portable electronic devices, such as smartphones and laptops.

## 1.1. Electrical Energy Storage (EES) Technologies

The modern electrical energy storage (EES) devices can be divided into three main

categories: fuel cell, batteries, supercapacitors, and conventional capacitors based on their energy or power density ( $\text{Wh m}^{-3}$  or  $\text{W m}^{-3}$ ) and specific energy or power ( $\text{Wh kg}^{-1}$  or  $\text{W kg}^{-1}$ ). Their positions in the Ragone plot can shed light on what kind of applications these devices can fulfill. For instance, the conventional dielectric capacitors at the upper left have extremely high power but limited energy and are often used as a filter to smooth current fluctuations. On the other end, fuel cells, which are capable of storing a significantly high amount of energy, are used as a back-up power source in commercial/residential buildings or even as primary power sources in remote places. However, the energy can only be stored or released from a fuel cell very slowly, which leads to a low power density. Here, one can intuitively deduce that the ideal EES devices will be in the upper right corner of the plot, such that a great amount of energy can be stored within a short period of time. The role of supercapacitors and batteries is to bridge the gap between capacitors and fuel cells, which have relatively higher energy than capacitors and higher power than fuel cells.

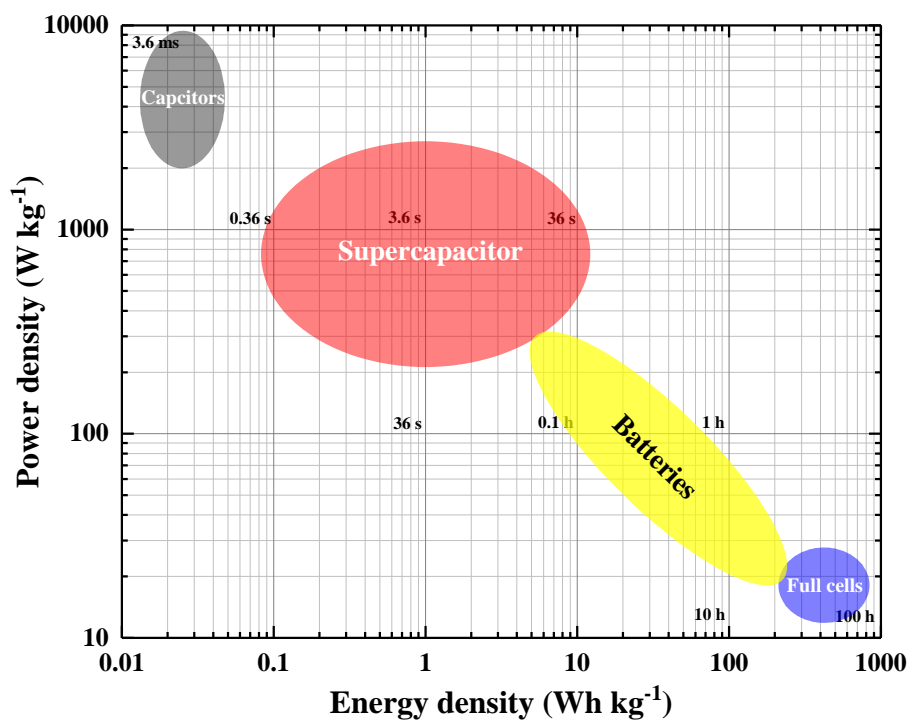


Figure 1.1. Ragone plot presenting the performance of various EES devices based on their energy and power densities. The data are collected from various reviews.[2-7]

In the field of batteries, there exists a trend from a bulky, dense, and toxic lead-acid battery (low energy/power density) to a smaller, lighter, and more environmentally friendly lithium-ion battery (LIB; high energy/power density). Details can be found in Table 1.1 which also highlights the development of battery-type energy storage chemistry.[6, 7] Apart from energy/power characteristics, the cycle life is another key factor that affects whether a battery is ready for commercialization. The comparisons also clarify that LIB exhibits the best cycle life, which partly explains why LIBs have soon dominated the EES market since its appearance in the 1990s.

Table 1.1. Comparisons of various battery types sorted by reaction chemistry.[8]

<b>Battery Type</b>	<b>Specific Energy</b> (Wh kg <sup>-1</sup> )	<b>Energy density</b> (Wh kg <sup>-1</sup> )	<b>Cycle Life</b>
<b>Pb-acid</b>	35	70	250-300
<b>Ni-Cd</b>	40	100	300-700
<b>Ni-MH</b>	90	245	300-600
<b>Li-ion</b>	125	440	1000

## **1.2. Lithium-ion Batteries (LIBs)**

As aforementioned, among all the different types of batteries, LIBs have exhibited great potentials due to the high energy density at a relatively high-power regime, contributed by the high electrode potential and the low atomic number of lithium. The preliminary concept of LIBs was first proposed by G.N. Lewis in 1912. Several attempts and breakthroughs had been made, e.g., discovery of propylene carbonate electrolyte by W. Harris, until the

commercialization of graphite-fluoride lithium primary battery by Matsushita. From the 1970s to the 1980s, the energy density of LIBs had been significantly improved from ~5 mAh to ~1,000 mAh per cell. In June 1991, Sony Energytec Inc. introduced the  $\text{LiCoO}_2/\text{LiC}_6$  and successfully demonstrated its feasibility and reliability in LIB applications. After almost 30 years, although the battery industries have developed tremendously, the chemistry behind this  $\text{LiCoO}_2/\text{LiC}_6$  cell remains unchanged and still dominates the energy storage market.[9]

The working principle of LIBs is illustrated in Schematic 1.1. In general, a LIB cell consists of two electrodes separated by a polymer membrane. The organic electrolyte acts as a carrier to allow Li ions to move between anode and cathode, such that electron flow can be created. The conversion from chemical energy to electrical energy requires different electrode potentials, which can be fulfilled by different electrode materials. In the cathodic part, the typical materials are transition metal oxides with a layered structure, such as  $\text{LiMnO}_2$  or  $\text{LiFeO}_4$  where Li atoms are stored. During the charging process, those Li atoms are removed together with the oxidation of the transition metal (higher valences). Subsequently, the free lithium ions travel through the membrane separator via the liquid electrolyte to the anode. The commercial graphite anode can store all Li atoms via intercalation, upon which a full charge process has been accomplished. The fully charged LIB is ready to deliver electrical energy through the movement of Li atoms from the anode back to the cathode.

The commercially available anodes and cathodes are both slurry-based composite electrodes, which consist of three components: active material, polymer binder, and conductive additive. Typically, the active material refers to the substance that participates in the storage of the Li ions, such as graphite for the anode and  $\text{LiCoO}_2$  for the cathode, while the others do not contribute to the energy storage. Instead, they help to hold the overall structure of the electrodes tight and ensure a decent electric conductivity. This kind of composite electrode can be fabricated by mixing these three components in an organic solvent and then pasting the slurry

onto the current collectors. It is worth noting that different materials are used as current collectors, e.g., copper foil for the anode and aluminum for the cathode, due to their stabilities under certain potential ranges vs.  $\text{Li}/\text{Li}^+$ . [9]

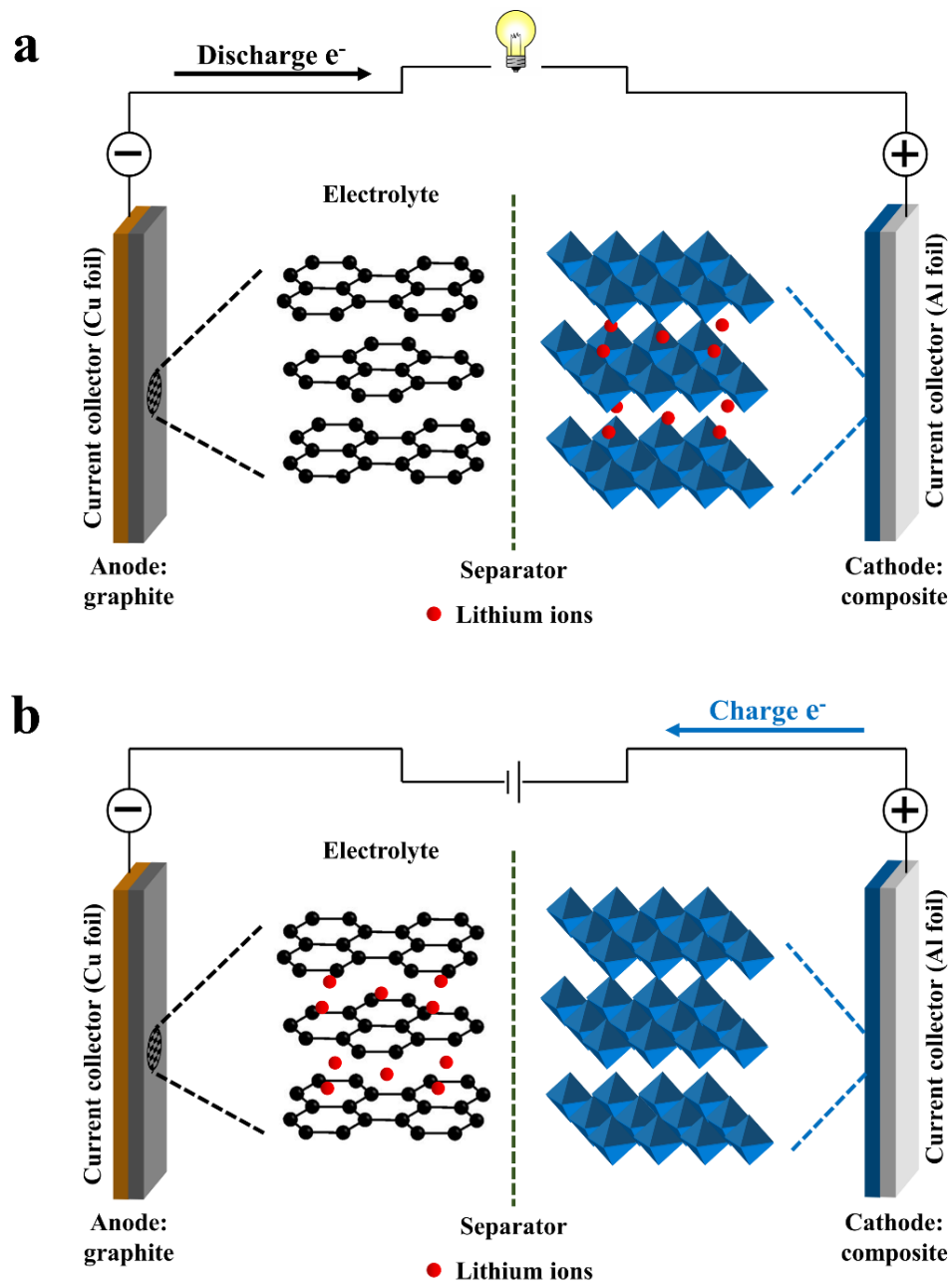


Figure 1.2. Schematic illustration of a conventional LIB design: (a) charge and (b) discharge processes of a lithium-ion battery (LIB) cell, during which  $\text{Li}$  ions move between cathode and anode to create electron flow.

### 1.3. Anode Material Candidates

As the work presented in this thesis focuses on the anodic part, literature reviews have been done to gain sufficient knowledge about anode materials in LIBs. It should be noted that Li metal anode is excluded here because the appearance of LIB anodes is to circumvent the dendrite growth on the surface of Li metal anodes. Technically, batteries with Li metal anodes do not belong to the LIB categories due to cell chemistry. Except for dendrite growth that causes safety issues, Li metal shows great promise as a battery anode including a high specific capacity of 3860 mAh g<sup>-1</sup> and the lowest electrode potential (i.e. maximized cell voltage).[8] Therefore, some research groups are still dedicated to understanding the mechanisms behind and in order to suppress dendrite growth.[10, 11]

### 1.3.1 Graphite (C)

As mentioned, graphite is widely used as the anode in commercial LIBs due to its abundance and low cost. Lithium ions in the electrolyte will intercalate into the hexagonal structure of the graphite anode under a certain potential range. Each hexagonal carbon ring holds one Li atom and frees one electron through the reaction path shown in Equation 1.1, which yields a theoretical capacity of ~372 mAh g<sup>-1</sup>. [3]



**Benefits:** As the ratio between Li and C atoms is 1:6, the volume change is limited to ~10% during (dis-)charge that contributes to superior cycling stability.[12] Moreover, the low lithiation potential close to Li/Li<sup>+</sup> gives a high cell voltage, and thus maximizes the energy density. The long lifetime and high stability have made graphite the preferred anode material in LIBs since its emergence in the 1990s. This is also one of the reasons why graphite anode enabled the commercialization of LIBs more than 30 years ago and is still used as anode currently.

**Drawbacks:** Although graphite anodes benefit from the low volume expansion, the chemistry up to 1 Li to 6 C ratio also limits the specific capacity to some extent. In addition, the

low potential vs. Li/Li<sup>+</sup> leads to the formation of solid-electrolyte interphase (SEI) on the graphite surface during lithiation, which is always associated with electrolyte decomposition, irreversible Li<sup>+</sup> consumption, and increase of the cell internal resistance.[12]. When graphite anode has to work under high (dis-)charge rates, Li deposition might occur on the surface of graphite anodes due to higher overpotentials and the low Li diffusivity in graphite of  $\sim 10^{-10}$  cm<sup>2</sup> s<sup>-1</sup>. [10] The deposited Li will be in a dendrite form that may break the separator causing a short circuit and related safety issues, e.g., Samsung Note 7.

### 1.3.2 Lithium Titanite Oxide (LTO)

LTO is another commercialized anode material in LIBs with an fcc (face-centered cubic) spinel structure and a chemical formula of Li<sub>4</sub>Ti<sub>5</sub>O<sub>12</sub>. Its applications include EVs and portable electronic devices by some famous companies, such as Mitsubishi, Honda, and Samsung. The energy storage of LTO is originated from the Li<sup>+</sup> (de-)intercalation via the reaction path shown below in Equation 1.2:[13]



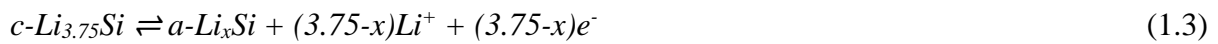
**Benefits:** Although LTO anodes do not have a specific capacity as high as graphite, the successful commercialization has already proven its strength as an anode in LIBs. The LTO is considered as “zero strain” material due to the negligible (e.g.,  $\sim 0.2\%$ ) volume expansion upon full lithiation, giving excellent cycling stability of tens of thousands of cycles.[3] Furthermore, the relatively high equilibrium potential ( $\sim 1.55$  V vs. Li/Li<sup>+</sup>) can unquestionably avert Li depositions and SEI formation, resulting in superior rate capability.[12] The fast (dis)charge makes the LTO anodes suitable for some high power applications, such as accelerations of EVs.

**Drawbacks:** Nevertheless, there are always two sides of the same coin. The chemistry shown in Equation (1) heavily limits the specific capacity ( $\sim 175$  mAh g<sup>-1</sup>), which is less than

a half compared to that of graphite anode. Moreover, the high equilibrium potential of LTO significantly limits the cell voltage of batteries with LTO anodes, further restricting the energy density of LTO-based batteries. This explains why LTO anodes are not widely implemented, even though the features of LTO (e.g., free of SEI) resolve the safety issues of graphite anode under high rates.[14]

### 1.3.3 Silicon (Si)

Si, representing various alloy anode materials, has slightly different mechanisms compared to graphite and LTO. Instead of  $\text{Li}^+$  intercalation, these materials can form alloys with Li at certain potentials, thereby creating electron flow. Among kinds of alloy anode candidates, Si is the most famous one and being extensively studied by researchers. Si reacts with Li at relatively low potentials ( $\leq 0.4$  V vs.  $\text{Li}/\text{Li}^+$ ) to gradually form the end products  $\text{Li}_{15}\text{Si}_4$  upon full lithiation at room temperature, following Equation 1.3 and 1.4:[15, 16]



**Benefits:** Si has an extraordinarily high theoretical capacity of  $\sim 3,580$  mAh  $\text{g}^{-1}$  ( $\text{Li}_{15}\text{Si}_4$ ) at room temperature that shows great potential in significantly lowering the weight and volume of future LIBs.[5] The 3.75 to 1 ratio of Li and Si at room temperature also explains the outstandingly high specific capacity. This number can be further boosted to 4,200 mAh  $\text{g}^{-1}$  at elevated temperature upon the formation of  $\text{Li}_{22}\text{Si}_5$ . [16] The highest abundance in the Earth's crust and non-toxicity also makes Si a cost-effective and safe anode material candidate.

**Drawbacks:** The processes described in Equation (1.3) and (1.4) are often associated with the formation of multiple phases with different crystal structures or amorphization, which makes the Li-Si a very complicated system and difficult to control.[17] No successful commercialization attempts have been achieved due to the large volume expansion ( $> 300\%$ ;

i.e. huge mechanical strain) and the brittleness (i.e. low plasticity) of Si, which can cause the structure to collapse and induce the loss of materials, leading to drastic capacity fading over cycling. The other issues, such as the low electrical conductivity of Si ( $\sim 10^{-3} \text{ S cm}^{-1}$ ) and the slow diffusion of Li in Si ( $10^{-14}$  and  $10^{-13} \text{ cm}^2 \text{ s}^{-1}$ ) will significantly hinder the rate capabilities of Si anodes.[18] As a result, a limited amount of Si can still be utilized in combination with other anode materials, e.g., graphite to increase the specific capacity.

#### **1.3.4 Other alloy anodes**

Other elements can form alloys with Li electrochemically, such as tin (Sn), germanium (Ge), antimony (Sb), and aluminum (Al). Similarly, all these elements can form alloys with Li. For instance, Sn and Ge can deliver  $994 \text{ mAh g}^{-1}$  and  $1384 \text{ mAh g}^{-1}$  at room temperature, upon the formations of  $\text{Li}_{22}\text{Sn}_5$  and  $\text{Li}_{15}\text{Ge}_4$ , respectively.[19] Detailed information can be found in the literature.[20, 21] For Sb and Al, on the other hand, the reaction stoichiometry is relatively simple with a well-defined potential plateau during electrochemical lithiation and delithiation,[22] representing the formation of  $\text{Li}_3\text{Sb}$  ( $660 \text{ mAh g}^{-1}$ ) and  $\text{LiAl}$  ( $993 \text{ mAh g}^{-1}$ ) at room temperature.[4] Apart from pure elements, various intermetallic compounds also exhibit promising features as anode materials in LIBs by modifying the electrochemical behaviors of pure elements.[22] Lastly, the properties of alloy anode mentioned above have been summarized in Table 1.2 for clear reference.

Table 1.2. Comparisons of various anode materials for LIBs. [2, 4, 22, 23]

Element	Specific Capacity (mAh g <sup>-1</sup> )	Final Alloy Composition	Formation potential (V vs. Li/Li <sup>+</sup> )
C	372	LiC <sub>6</sub>	0.07 - 0.19
Si	3,580	Li <sub>15</sub> Si <sub>4</sub>	0.04 - 0.33
Sn	994	Li <sub>22</sub> Sn <sub>5</sub>	0.38 – 0.53
Ge	1,304 – 1,623	Li <sub>15</sub> Ge <sub>4</sub>	0.2 - 0.5
Sb	660	Li <sub>3</sub> Sb	0.85
Al	993	LiAl	0.27

## 1.4. Utilization of Al-based anodes

Currently, Al somehow does not draw the same attention as other alloy anode candidates, even though it possesses intrinsic advantages as an anode in LIB applications. It is well-known as a technical material due to its abundance, low cost, and light weight. In the lithium-ion battery industry, it does not only function as a current collector for positive electrodes but also can be attractive as an active anode material.[24, 25]

### 1.4.1 Motivations

Al forms alloys with Li at a relatively low potential vs. Li/Li<sup>+</sup> among alloy anode candidates, yielding a theoretical capacity of 993 mAh/g for the formation of the  $\beta$  phase (LiAl) alloy, which is about three times higher than the current state-of-the-art graphite anodes.[26, 27] Compared with other anode materials which have multiple lithiation potentials, there is one aluminum-lithium compound which is dominant at room temperature: the  $\beta$  phase. It has a simple stoichiometry and a flat and wide plateau potential (~0.25 to ~0.3 V during lithiation) that makes the LIBs with aluminum anodes easier to control. More importantly, using aluminum anodes in LIBs would simplify the manufacturing process, during which aluminum

can serve as both the whole anodic compartment (active material and current collector) and the cathodic current collector. By doing so, the number of different materials and the material cost of future LIBs might be considerably reduced by omitting the copper and carbon, which are presently used at the anode.[28-31]

#### **1.4.2 Challenges**

Although there are noticeable advantages of Al as a negative electrode in LIBs, significant capacity fading during cycling and poor charge efficiency are the main obstacles that limit the commercial utilization of Al-based LIBs.[24-26] Some studies claim that the capacity fading is caused by the volume expansion of nearly 100%, associated with pulverization and delamination. For instance, Tahmasebi et al. observed using the *ex situ* SEM fracture and delamination of Al thin films during delithiation.[32] An *in situ* TEM study indicates that Al nanowire anodes evolve to become isolated particles after repeating cycles, with void growth during delithiation being the primary cause for pulverization.[33] Other groups suggested another explanation and propose a kinetic model for the capacity fading: lithium trapping might be responsible, even if no structural failure takes place. This involves the enclosure of the Li-rich  $\beta$  phase within the poorly Li-conducting  $\alpha$  phase.[34] Meanwhile, some researchers are focused on developing new structures to optimize the electrochemical performance of Al-based anodes.[28, 35-37] The origin of this seemingly intrinsic degradation is not entirely clear. At the end of the day, no solid conclusion has been drawn regarding the extent of the degradation behaviors, and aspects of the underlying mechanisms of the electrochemical Li-Al system remain poorly understood.

#### **1.4.3 Li-Al phase diagrams**

The solid-state first-order phase transformation from  $\alpha$  phase (Al structure, fcc) to the  $\beta$  phase (LiAl, NaTl structure, cubic) at room temperature is the origin of the lithium storage during the electrochemical lithiation of crystalline Al. As it can be seen from the Li-Al phase

diagram in Figure 1.3 and Figure 1.4, the  $\beta$  phase exhibits a wide solubility range that narrows done at the lower temperature regime and should give a rough 1:1 ratio between Li and Al at room temperature. It should be noted that there is no solid evidence at this moment showing that other phases can be formed at room temperature. Apart from the  $\sim 100\%$  difference in volume, these two phases also have different mechanical and chemical properties. For instance, the ductile Al will turn brittle after transforming into the  $\beta$  phase.[38] As for the chemical kinetics, the Li transportation within the  $\beta$  phase is roughly four orders of magnitude faster than the  $\alpha$  phase ( $D \sim 10^{-12}$  vs.  $D \sim 10^{-8} \text{ cm}^2 \text{ s}^{-1}$ ) at room temperature,[39-42] while the diffusivity value of the conventional graphite anode for LIBs is  $\sim 10^{-10} \text{ cm}^2 \text{ s}^{-1}$ . Finally, it should be noted that the Li-Al phase diagrams were established at an elevated temperature regime (e.g.,  $>400$  °C). By comparing the two versions, inconsistencies can be found, specifically the Li solubility range of the  $\beta$  phase at a low temperature regime. This Li solubility might not be relevant for the phase diagram studies but can be crucial for LIBs that mainly operate at room temperature.

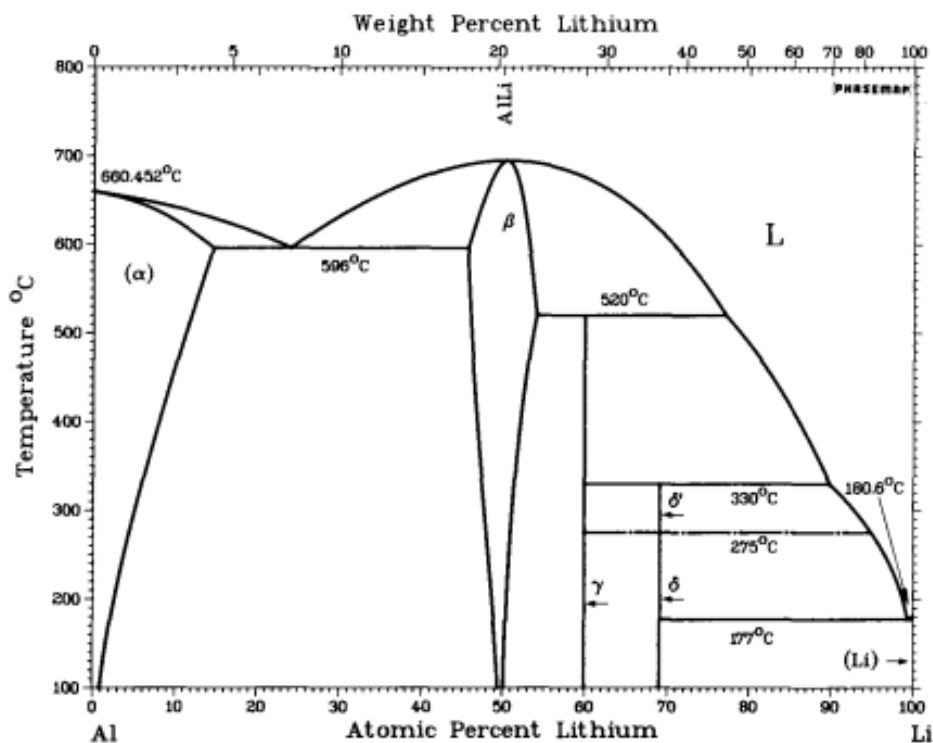


Figure 1.3. The Li-Al phase diagram published in 1982, reprinted from A.J. McAlister [43].

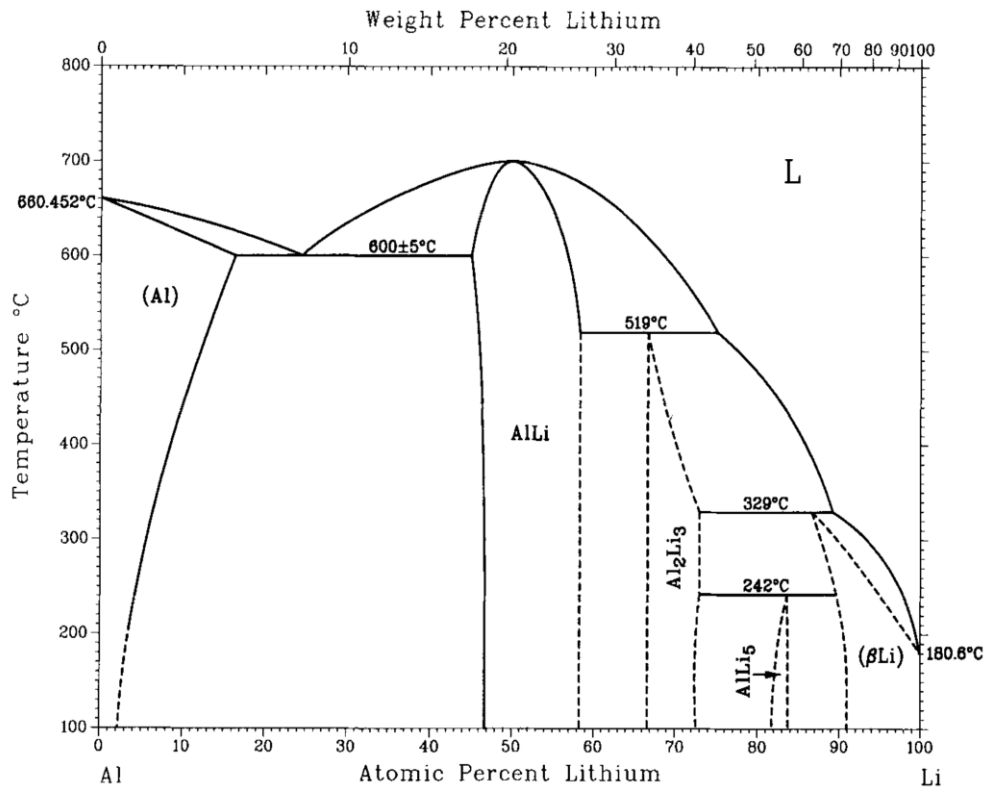


Figure 1.4. The Li-Al phase diagram published in 1986, reprinted from Murray, J. L., et al.[44]

#### 1.4.4 Li-Al crystal structures

The structures of crystalline Al and  $\beta$ -LiAl are schematically illustrated in Figure 1.5. The well-known Al has the typical face-centered cubic structure with a lattice constant of 4.05 Å while the lithiated  $\beta$ -LiAl remains a cubic structure and extends the lattice constant to ~6.37 Å.[45] Eight Al atoms are accommodated in the elemental cell of the  $\beta$ -LiAl, giving a ~95% volume expansion upon the  $\alpha$  to  $\beta$  phase transformation.[35] They also have different ground energy levels of -119.681 eV and -385.459 eV, respectively.[46]

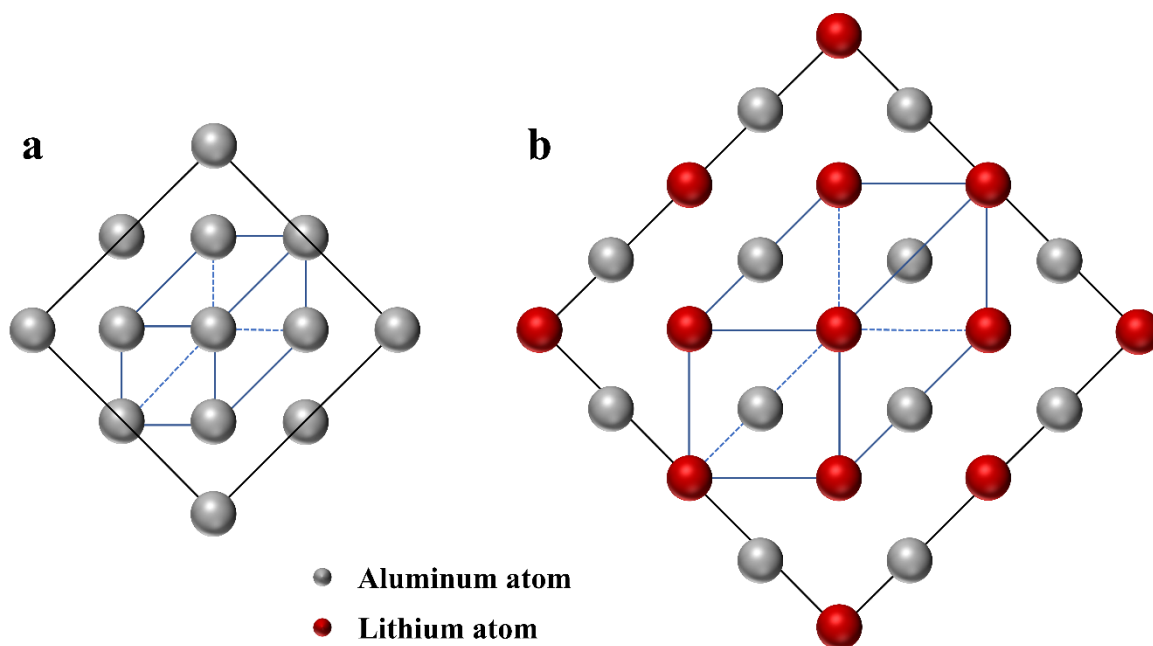


Figure 1.5. Schematic drawing of crystal structures: (a) the fcc-Al and (b) the  $\beta$ -LiAl.

## 1.5. Research objectives

The goal of the research presented in this thesis is to enable and/or provide relevant information/knowledge towards the commercialization of Al-based anodes, by resolving their technical difficulties. However, available literature on Al-based anodes is significantly limited compared to other alloy anode candidates, and most studies were done in or before the 1990s. Therefore, strategic, systematic, and probably procedurally investigations are necessary to achieve the ultimate research objective in a step-by-step fashion, of which the sub-goals are listed below:

- I. To gain fundamental understandings of lithiation phase transformation in aluminum thin film electrodes, by investigating its kinetics under various potentials vs.  $\text{Li}/\text{Li}^+$ .
- II. To learn the Li transportation pathways during the lithiation phase transition of aluminum thin film, by identifying its grain orientations and grain boundaries.
- III. To elucidate the degradation behavior of aluminum thin film electrode, by tracking its mechanical stress during the electrochemical phase transformations.

- IV. To extend the knowledge of the phase transformations in Al thin films towards bulk Al foils, by highlighting their similarities and differences.
- V. To assess the commercialization feasibility of Al-based anodes in Li storage, by demonstrating the cycling performance in both half-cell and full-cell configurations.
- VI. To recommend strategical pathways of utilizing Al-based anodes in battery applications, by trying to resolve or circumvent the seemly intrinsic shortcomings during the phase transformations.

## 2. Experimental Section

### 2.1. *Operando* light microscopic cell

**Electrode fabrication:** Current collectors and electrodes were prepared by physical vapor deposition (PVD) sputtering. Titanium nitride (TiN) was reactively sputtered onto the borosilicate glass as current collectors using a PVD system (MAT 400, Germany), to make use of the high electrical conductivity and the decent stability of TiN in electrochemical energy storage applications.[47, 48] The selective deposition was achieved using Kapton tape as a masking material. A 12-inch high purity titanium (Ti) target (99.999%) was used to carry out the thin film deposition for 20 minutes at 1500 W incident power with 30 sccm argon and 25 sccm nitrogen as background and reactive gases. After the preparation of current collectors, the TiN on glass substrates was transferred to a Denton Explorer Sputtering System (Denton Vacuum, USA). The substrate was heated to 550°C prior to Al deposition, and the masking method was changed to stainless steel clips and copper foil to adapt to the elevated temperature. A 3-inch high purity Al target (99.9995%) was employed to deposit the electrode material on the TiN films for 50 minutes with 300 W incident power and 30 sccm argon flow, resulting in 0.25-0.3 cm<sup>2</sup> surface areas. The deposited Al thin film electrodes were estimated to have a thickness of ~1 μm based on the calibrated deposition rate, corresponding to a charge density of 0.27 mAh cm<sup>-2</sup> assuming conversion to the LiAl 1:1 alloy.

**Cell assembly and operation:** The assembly of the light microscopic cells was done inside the argon-filled glove box. The cell design (Figure 2.1) was inspired by Steiger et al.,[10] where the borosilicate glass (50×75×0.7 mm<sup>3</sup>) with the sputtered TiN and Al was considered as the main body. A polyethylene (PE) frame was attached to the glass substrate to form the cell chamber, which was filled with the electrolyte (1M LiPF<sub>6</sub> in EC:EMC:DEC 1:1:1 Vol%) and then sealed with a borosilicate cover glass (30x30x0.2mm<sup>3</sup>). The assembled glass cells

were placed under a high-resolution optical microscope (DM4000, Leica, Germany) at ambient conditions. The observed region of each cell was fixed in the middle of the sputtered Al thin film while the Li counter electrode was always placed at the same position next to the working electrode. The time-lapse images were taken under the bright field (100× to 400× magnification) with fixed time intervals and analyzed by ImageJ-NIH software. As images were captured during electrochemical testing, the transition from Al to LiAl was evidenced by a disruption in the reflectance of the surface causing the LiAl phase to appear as darker regions in the images. It should be mentioned that a dummy cell with only TiN thin film current collectors was also prepared for estimating the background current contributed by the cell configuration.

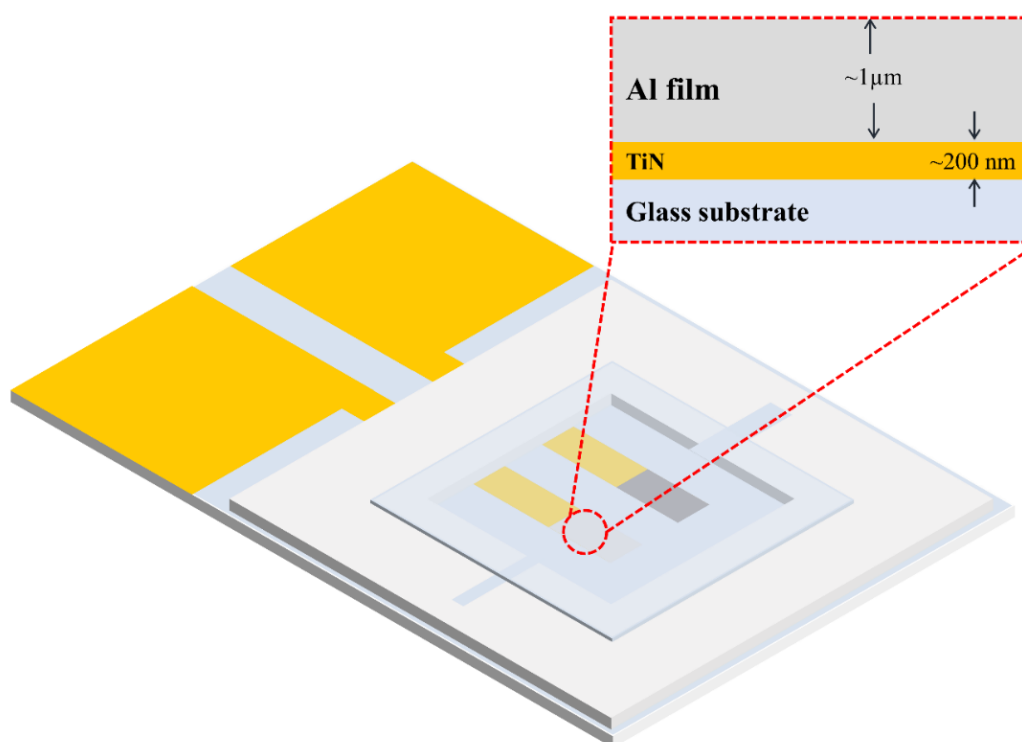


Figure 2.1. Design of the *operando* light microscopic cell. The titanium nitride (TiN) current collectors are drawn in gold color, of which the tips represent aluminum (Al) working electrode (light grey) and lithium (Li) metal (dark grey), respectively. Polyethylene (PE) is drawn in white, such that the glass substrate and the cover glass can be revealed.

## 2.2. *In situ* stress cell

**Electrode fabrication:** Cantilevers made of aluminum oxide with the size of  $15 \times 5 \times 0.25 \text{ mm}^3$  are double-side polished prior to the same PVD processes described before. The thickness of TiN and Al films for stress measurement are characterized to be  $\sim 160 \text{ nm}$  and  $\sim 420 \text{ nm}$ , respectively.

**Cell assembly and operation:** *In situ* stress measurement was achieved using the method of substrate curvature. In a substrate-based model where a rigid interface exists, the volume expansion caused by Li insertion strains the substrate and results in compressive stresses. As illustrated in Figure 2.2, the home-built three-electrode cell and two-beam laser setup[49] allow simultaneous measurement of the curvature of the substrate. Once the lithiation starts, the bending of the alumina cantilever can be tracked *in situ* by recording the distance change between the two laser spots. It should be noted that the stress values are normalized to the initial Al film thickness, referring to the nominal stress, such that the thickness change during (de-)lithiation is not taken into consideration. In other words, the mechanical stress reported in this study is a product of stress-thickness over the initial thickness and can be quantified using Equation 2.1 (Stoney equation):

$$\Delta\sigma_f = \frac{E_s h_s^2}{6h_f(1-\nu_s)} \frac{1\Delta d}{2n_e l L} \quad (2.1)$$

Where  $E_s$ ,  $h_s$ , and  $\nu_s$  are the Young's modulus (314 GPa), the thickness and the Poisson's ratio (0.21) of the alumina substrate, respectively;  $h_f$  is the initial thickness of the TiN film ( $\sim 160 \text{ nm}$ ),  $n_e$  is the refractive index of the organic liquid electrolyte,  $\Delta d$  and  $l$  are the initial distance and the distance change between the two laser spots,  $L$  is the distance between the cantilever and the camera sensor. As the alumina substrate and the TiN film are inactive to Li, the stress signal is anticipated to be directly correlated to the stresses due to volume changes within the thin films.

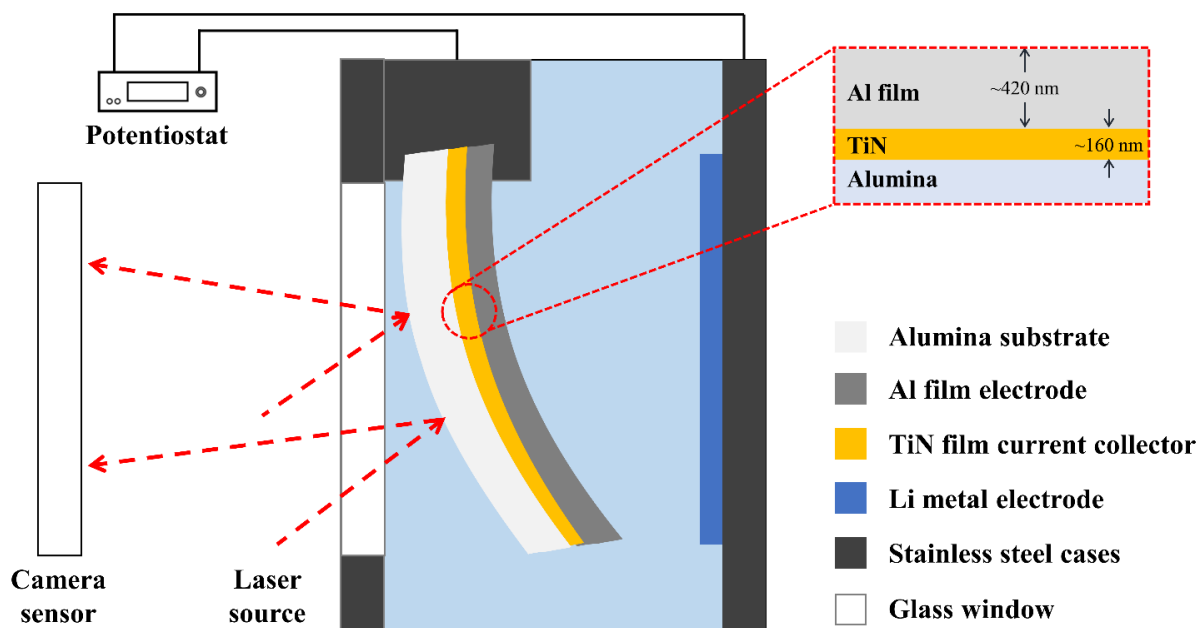


Figure 2.2. Schematic drawing of the *in situ* stress cell, of which the substrate curvature can be tracked during charge and discharge. The layered structure is elaborated in the cross-sectional illustration.

### 2.3. *Operando* XRD coin cell

**Electrode fabrication:** The ultrahigh purity Al foil was obtained from Alfa Aesar (99.9995%; 38  $\mu\text{m}$  thick). The as-received foil was punched into disks with a diameter of 12 mm and then was cleaned by isopropanol prior to the cell assembly.

**Cell assembly and operation:** The conventional coin cell is modified, namely by drilling a hole on the upper and the lower cell case, respectively. The holes were sealed with epoxy glue and two pieces of borosilicate glass. Thereafter, the cell assembly is the same as conventional coin cells as illustrated in Figure 2.3. With a specifically designed platform, the crystalline information of the Al foil can be extracted by Mo-based x-ray during electrochemical cycling.

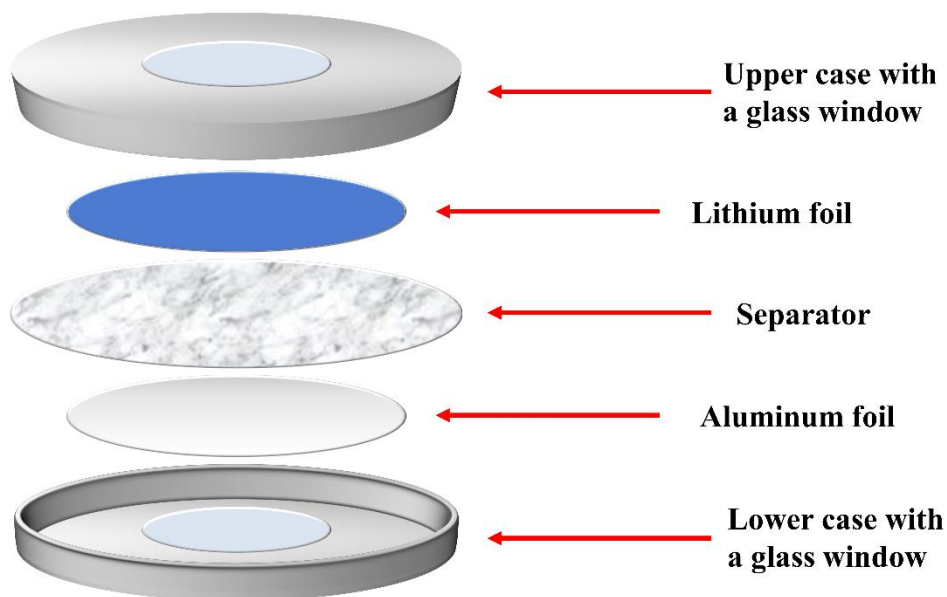


Figure 2.3. Design of the *operando* XRD coin cell, of which a glass window is manually created that makes transmissional geometry.

## 2.4. Two-electrode beaker cell

**Electrode fabrication.** The Al stubs (5 mm ×  $\varnothing$  12.5 mm) were obtained from Agar Scientific Ltd. and the Al pellets (3 mm ×  $\varnothing$  10 mm; 99.7%) were bought from a local supplier. The as received pellets were immersed into absolute ethanol and placed in an ultrasonic bath for half an hour. Afterward, the Al pellets underwent a series of grinding using silica papers from 60 mesh to 2000 mesh and were cleaned by ethanol again prior to further usage.

**Cell assembly and operation.** The conventional beak cell is slightly modified to allow a meniscus contact between the Al pellet and the electrolyte (as illustrated in Figure 2.4), such that one-dimensional propagation of the  $\beta$  phase can be maintained during lithiation. A piece of Li metal was placed right underneath the Al pellet as the counter electrode with a minimized distance. It should be noted that the electrochemical tests of such a beaker cell were conducted inside an argon-filled glove box to ensure an oxygen/water-free environment.

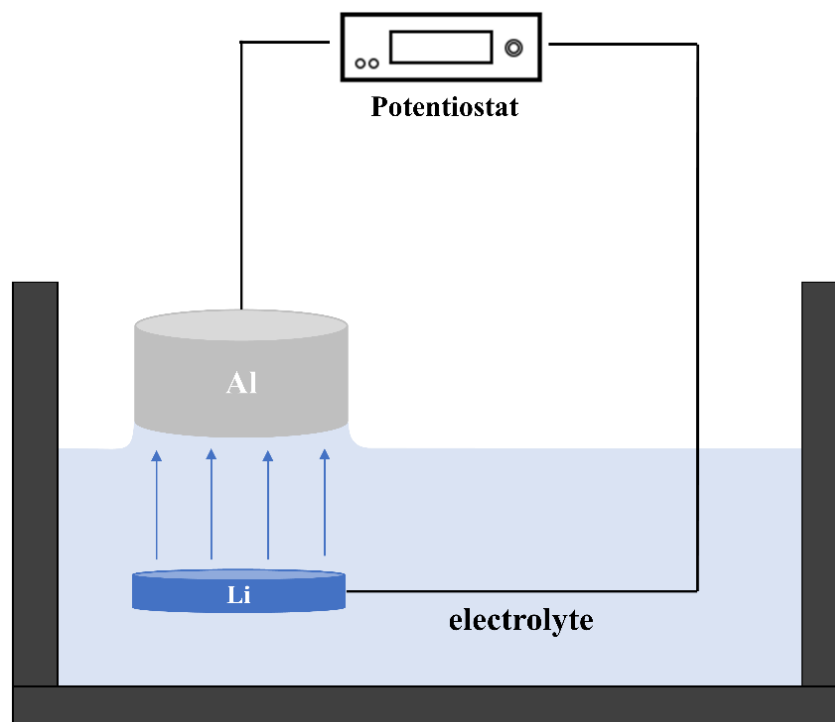


Figure 2.4. Graphic illustration of a modified two-electrode beaker cell, in which a meniscus contact between the bulk Al electrode and the electrolyte can be achieved by adjusting the electrode height.

## 2.5. Swagelok-type cell and coin cell

Swagelok-type cells were assembled along with the *operando/in situ* cells to take advantage of easier disassembly and reassembly, such that *ex situ* observations can be achieved. Coin cells (2025) were also prepared to compare the electrochemical response with that of the other cells. The electrodes have a size of 10-12 mm in diameter for Swagelok cells and 12-16 mm for coin cells. Copper foil current collector (10  $\mu\text{m}$  thick) was used for the sputtering of Al thin films. In the case of the bulk Al foils, no Cu foil is required as this monolithic foil electrode functions as both current collector and active material. Half-cell configuration (16 mm diameter) was built by placing Li metal as the counter electrode while a full cell with Al foil anode was assembled by pairing with a commercial  $\text{LiFeO}_4$  cathode (Customcells, Germany), separated using either a porous polymer separator (Celgard, USA) or a glass fiber

separator (Whatman®).

## 2.6. Electrochemical tests

A VMP potentiostat (Biologic Technologies, France) was employed to carry out various electrochemical tests. Firstly, potentiostatic mode was used to conduct the kinetic study regarding how Li gets incorporated into Al during electrochemical lithiation (i.e. the  $\alpha$  to  $\beta$  transformation). Moreover, the galvanostatic mode was used to simulate the practical working conditions of batteries. The other electrochemical techniques such as cyclic voltammetry (CV) and electrochemical impedance spectroscopy (EIS) were also used to assess the cell performance. With help of the various cell types, the (de-)lithiation processes can be further elaborated.

## 2.7. Material characterizations

**Scanning electron microscopy (SEM).** The *ex situ* SEM was done by opening the Swagelok half cells. A specifically designed transfer system (Leica VCT100) allows the immediate sample transfer from the glovebox to the SEM (Zeiss Merlin) without exposure to air. *Ex situ* SEM images were acquired under an acceleration voltage of 6 kV, using two detectors for secondary electrons (SE) and for backscattered electrons (BSE), such that the three-dimensional (3D) morphology and the  $\beta$  phase distribution can be revealed. After that, the electrode was reloaded into the glovebox and reassembled into the Swagelok cell, such that the electrochemical test can be continued.

Cross-sectional SEM was done through a cut and grinding process inside an argon-filled glovebox. The ultrahigh purity Al foil obtained from Alfa Aesar (99.9995%; 0.25 mm thick) was slightly lithiated in a Swagelok cell and then disassembled inside the glovebox. After flushing with pure DMC to remove the salt residue on the surface, the electrode was cut

into half. Two specifically designed PE blocks were used to hold the Al foil to undergo a series of grinding using silicon carbide papers (from #1000 to #5000). The created cross-section was flushed again with pure DMC before loading the specimen into the SEM chamber.

**Electron backscatter diffraction (EBSD).** The microstructure within the area was characterized using a Nordlys 2S EBSD detector (Oxford Instruments, UK) attached to a JEOL JSM 7600F field emission scanning electron microscope (FESEM). The complete scan was acquired to cover the area of  $141 \times 105.5 \mu\text{m}^2$  with a step size of  $0.2 \mu\text{m}$ . The running time for taking the EBSD measurement for 1 sample was approximately 12 hours. The orientation map was generated using MTEX (a MATLAB toolbox for analyzing EBSD data).

**X-ray diffraction (XRD).** High-resolution XRD (Rigaku SmartLab, Japan) was used to explore the crystal structure of the Al electrodes under a different state of charge (SOC). The samples were sealed in Kapton tape inside the glovebox before XRD tests to minimized air exposure. The scan step was  $10^\circ$  per minute with various  $2\theta$  ranges using the 45 kV maximum voltage and 200 mA maximum current. The deep lithiated Al electrode underwent the XRD test using a high-energy Rigaku SmartLab diffractometer equipped with a Mo anode tube. Such a Li-Al electrode was prepared by disassembling a Swagelok cell that underwent a potentiostatic hold at 5 mV vs. Li/Li<sup>+</sup> for 3 days and then sealing into Kapton tapes inside an argon-filled glove box.

*Operando* XRD was achieved using the specifically designed coin cell described above and a parallel beam diffractometer equipped with a Mo K $\alpha$  radiation anode in transmissional mode. A microfocus rotator was attached to the anode to have various incident angles while a Pilatus 300 K-W area detector was used to acquire structural information. Diffractograms were collected every 300 seconds during the electrochemical tests and optimized by co-loading two consecutive signals. The 2D diffraction images were integrated and analyzed using the pyFAI and the TOPAS V6.

### 3. Lithiation mechanisms: kinetic analyses

As mentioned, we aim to follow a step-by-step plan in order to achieve our research goals, and the problematic challenges remaining in Al-based anodes can only be resolved upon comprehensive understandings of the reasons behind. Therefore, the initial step would be to gain fundamental understandings of the Al electrode, its electrochemical performance, and the underlying mechanisms. The substrate-based model (i.e., Al thin films on rigid substrates or Cu foils) has been used to help investigate the electrode/electrolyte interface. Since the reaction kinetics during lithiation will decide whether the related degradation mechanisms might be minimized or prevented, their details are worth elaborating.

Kinetic analyses were conducted under potentiostatic modes in conjunction with the light microscopic cells. Potentiostatic modes create fixed electrical driving forces that can be ideal while the light microscopic cells allow simultaneous observation of the Al electrode during phase transformation. As a result, a series of video clips demonstrating the electrode change are achieved as direct evidence. Through coupling the electrochemical data with these *operando* optical images taken at specific time points (i.e. videos), extra insights can be yielded. In this part, we aim at building kinetic models to clarify the phase transition kinetics during the lithiation process and using this knowledge to improve the cycling performance of Al-based anodes in LIBs. This chapter was published in [50].

#### 3.1. Background

The model of Deal and Grove, which was developed to describe the growth of the oxide layer on silicon surfaces[51] has been well adapted to model phase transformation kinetics during electrochemical lithiation. Miao and Thompson developed a kinetic model based on the Deal-Grove model (which applies Fick's law for the case of a steady-state flux) to elucidate the initial lithiation of amorphous silicon thin film anodes for LIBs.[18] Another study also

presented a multi-stage model that illustrates the propagation of  $\text{Li}_x\text{Si}$  phase, the reaction rates at the interface, and the Li diffusion behavior in crystalline silicon.[52] For Al anodes, however, less information can be found regarding the kinetics of the electrochemical formation of Li-Al alloy at room temperature. Although a number of studies of the electrochemical kinetics in the Li-Al systems were conducted at elevated temperatures, e.g., by using emf measurements,[39, 41, 42, 53-56] the data obtained from the high-temperature regime can hardly be extrapolated to the domain that deals with incorporation kinetics of Li into Al at ambient temperature for LIBs. Moreover, the nucleation of the  $\beta$ -LiAl is assumed to be homogenous on  $\alpha$ -Al surface and the  $\alpha$  to  $\beta$  phase transformation could be modelled by the Deal-Grove model.[55, 56] Recently, Tahmabesi et al. reported that the quasi-1-dimensional (1D) thickening behavior described by the Deal-Grove model is not expected to be applicable for the lithiation of Al thin films. The nucleation and formation of the  $\beta$  phase are not uniform, and the growth of quasi-circular two-dimensional (2D) patches occurs at apparently random positions.[32] The degradation of the Al anodes will depend on the details of the phase transition between the  $\alpha$  (Al-based, fcc) and the  $\beta$  (LiAl) phase. To minimize and to prevent deterioration, it is, therefore, necessary to utilize appropriate models to explore the electrochemical incorporation of Li into Al.

Previous works of the phase transformation kinetics in LIBs heavily rely either on electrochemical data or on electron microscopy techniques, such as scanning electron microscopy (SEM)[32] or transmission electron microscopy (TEM),[33] which necessitate specific working conditions e.g., high vacuum. Consequently, specially designed architectures and/or interruptions of experiments are always associated with these studies. Furthermore, operational complexities and data reproducibility are always the main challenges using these techniques. Here we present an *operando* light microscopy which can be an ideal tool for investigating phase transformation kinetics since the new phase can be instantly revealed by

the contrast. Our setup includes an optical cell made of borosilicate glass and a high-resolution light microscope, such that simultaneous monitoring of the electrode surface during (de-)lithiation processes can be achieved. Although comparable *operando* light microscopy studies of Li metal anodes have been done before,[10, 57, 58] it is the first time to utilize similar equipment to conduct systematic investigations of Al-based anodes for LIBs. In addition to the visual observations done with the dedicated optical cells, a series of coin cells were assembled, and the same tests were done to compare the performance between the cells, such that the data generated can be directly applicable to conventional coin cells.

### 3.2. Results and Discussion

Microstructural characterization was performed to understand the phase transformation and evolution of the Al thin films upon lithiation and delithiation. Figure 3.1a reveals the surface morphology of a partial lithiated Al thin film, which exhibits quasi-circular shaped and isolated island-like patches at random positions. The corresponding image obtained from a detector for back-scattered electrons (BSE) are shown in Figure 3.1b. As can be seen, the formed patches all overlap with the darker regions, referring to the lithiated crystalline  $\beta$  phase. This contrast arises due to the Li atoms contributing fewer electrons than Al to the signal (i.e. lower mean atomic mass). Under higher magnifications and tilted conditions, the expansion along the z-axis can be clearly observed for the  $\beta$  phase patches (Figure 3.1c-f). Their diameter to height ratio keeps increasing as the lithiation proceeds, indicating 2D growth behavior. The lithiated Al thin film is further confirmed by x-ray diffraction (XRD). As shown in Figure 3.1e, the peaks at  $\sim 24^\circ$   $\langle 111 \rangle$  and  $\sim 40^\circ$   $\langle 220 \rangle$  of LiAl appear for the lithiated Al film, and then diminish after delithiation, proving the existence of the  $\beta$  phase.[59] It should be noted that the two unlabeled strong peaks are contributed by the Cu foil substrate.

The electrochemical incorporation of Li into Al was studied under various constant working potentials after holding at 0.5 V for 30 minutes to minimize the influence of surface (SEI-forming) reactions, which start below ca. 1.2 V according to the cyclic voltammograms (Figure S3.1a-b). Although the potentiostatic curves exhibit similarities to the 3-stage kinetics reported by Geronov et al. in the 1980s,[54-56] differences are to be expected mainly due to the thin film geometry (and to a minor extent due to the optical cell configuration) used in this study. Therefore, the electrochemical data of coin cells are also included to minimize the difference arisen from the configuration. As shown in the inset of Figure 3.1h, the transient can be characterized as: (1) there is an abrupt current decay immediately after the potential jump to the lithiation potential; (2) a fast rise of the lithiation current is observed then, (3) followed by a maximum, sometimes forming a broad plateau with quite constant current corresponding to the growth of the  $\beta$ -phase LiAl;[53, 55, 56] and (4) the current decreases towards the end of lithiation. As shown in Figure 3.1h, the optical cell generally exhibits the same 4-stage behavior, except that higher overpotentials are required for optical cells to overcome the higher internal resistance and the possible side reactions. Consequently, the current density of the optical cell is lower than that of the coin cell under the same applied potential. Nevertheless, the potentiostatic transients from the two cell geometries are overlaid at each applied potential, of which the general curve shapes are identical (Figure S3.1e-f), supporting the reliability of the optical cells.

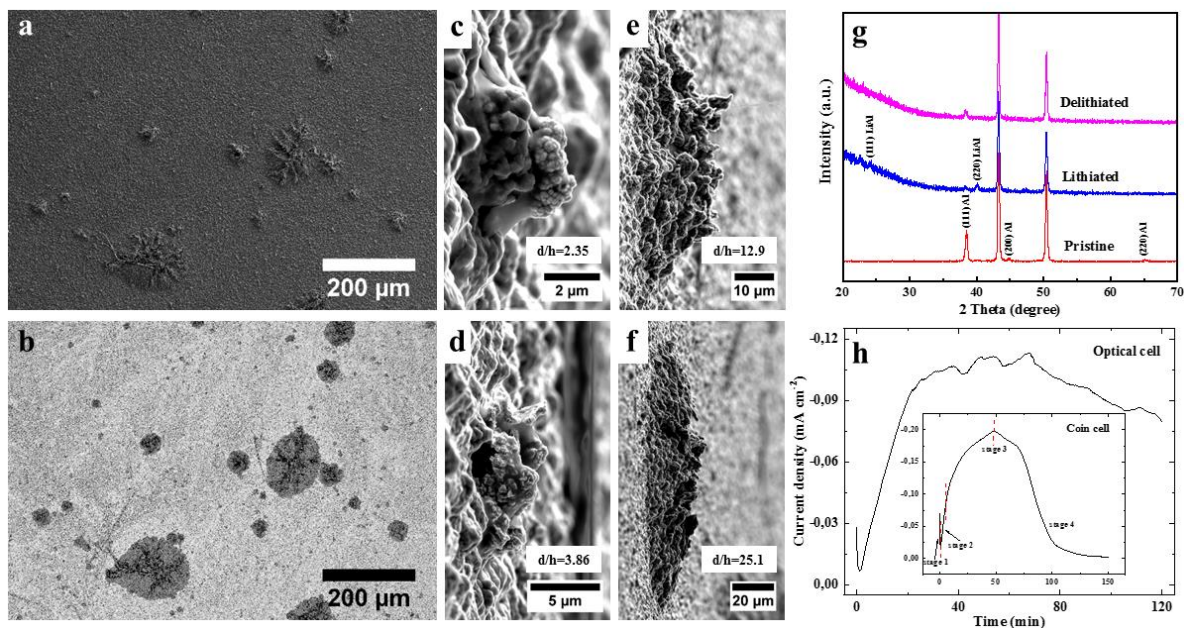


Figure 3.1. SEM images taken from a partially lithiated Al thin film using (a) a secondary electron (SE) detector and (b) a back-scattered electron (BSE) detector. (c-f) SEM observations along the z-axis of multiple  $\beta$  phase patches using a 90-degree sample holder with a tilting angle of 10 degrees. The d/h represents the ratio of diameter over the height of the given patch. (g) XRD diffractograms of pristine, lithiated, and delithiated Al thin films. (h) The representative current-time curve obtained from the preliminary experiments (120 mV) when developing the optical cell, and from the coin cell, where different stages are clearly shown.

In most cases, the lithiation kinetics of Al-based anodes has been studied based on electrochemical data and was not confirmed by independent means. By taking advantage of our *operando* light microscopy, the surface brightness change of the Al electrode is recorded instantaneously as soon as the electrochemical lithiation begins. A modified 4-stage kinetic framework based on Figure 3.2, in addition to the one suggested by Geronov et al., [54-56] has been established in this study and can be summarized:

**1. Initial lithiation:** This includes the solid solution lithiation of fcc Al without a phase transformation, i.e. while keeping the  $\alpha$  phase structure. According to the Li-Al phase diagram published in 1982, the maximum solubility of Li in Al at equilibrium ( $\alpha$  phase) is smaller than

~2 at.% at room temperature.[60] However, overlithiation well beyond the equilibrium value might be possible, especially before the nucleation of the  $\beta$  phase takes place. Therefore, the  $\alpha$  phase lithiation charge might be larger than that expected for 2 at.% of Li, (e.g., 2.6 at.%).[55] On the other hand, the transport of Li in the  $\alpha$  phase might be extra slow at room temperature.[61] Therefore, the lithiated  $\alpha$  phase volume might be limited to a thin layer at the sample surface, and the current corresponding to  $\alpha$  phase lithiation might be minor. Then, the observed current possibly belongs rather to SEI formation and Al oxide lithiation than to the  $\alpha$  phase lithiation.

## 2. Electrochemical nucleation and initial growth of the $\beta$ phase (LiAl) (ca. 50 at.%):

The initial growth of the  $\beta$  phase can be 3D in all cases considered up to now since extremely thin Al layers (i.e. thin films) have not been investigated yet. In the previous work with Al wires, this phase of the initial 3D growth of the nuclei ends when more and more growing nuclei impinge with each other. According to this study by Geronov et. al.,[56] the current is a cubic  $t^3$  function of the time in the initial growth regime, owing to the 3D growth with progressive nucleation.

## 3. Stable growth of the $\beta$ phase (LiAl):

**a)** In the case of **thick** (bulk) Al samples (e.g., Al foil), their surface is covered with a  $\beta$ -LiAl layer after some time. Lateral growth is not possible anymore, and only the in-depth growth along the z-axis can take place. Therefore, the stage 2 growth regime with a fast increase in the interface area between  $\alpha$  and  $\beta$  phases is followed by the stage 3 growth regime where the  $\alpha/\beta$  interface moves into the sample but does hardly change its area anymore (**quasi-1D growth**). In this second regime, the current would be constant if the phase transformation would be the only rate-determining factor. Since Li transport is involved as well, a decline in the current should have taken place due to the increasing diffusion distances, but this decrease is not pronounced for LiAl formation since the transport in the  $\beta$  phase is reported to be

sufficiently fast.[62, 63]

**b)** For the **thin** film samples, the in-depth growth is limited, and many growing nuclei will reach the electrode-substrate interface before they touch other nuclei. Therefore, in our case, the 3D growth of stage 2 is limited to the dimension of the film thickness. Later during stage 3, only a **2D growth** of the nuclei is possible. This 2D growth will be responsible for most of the consumed charge. In contrast to bulk samples that reach the state with an almost constant  $\alpha/\beta$  interface area, the  $\alpha/\beta$  interface area will never be constant in our case but will increase and decrease from time to time.

**4. Completing the phase transformation:** The current decreases to close to 0 since the fresh Al is used up, and the phase transition from  $\alpha$ - to  $\beta$ -LiAl is complete. This regime of pronounced current decrease was not studied for thicker bulk Al samples but is important for our thin film samples.

By summarizing the above mentioned 4 stages with the help of the *operando* images and the electrochemical data collected from coin cells under the same potentiostatic conditions (Figure S3.1c-d), schematic illustrations (Figure 3.3) are employed to understand the nucleation and the phase transformation processes. These illustrations of the cross-section are complementary to the *operando* images since the expansion along the z-axis is invisible under the light microscope. This vertical expansion during lithiation has been confirmed by the SEM images in Figure 3.1a-f, and can also be supported by Leite et al.[64] and Gooranorimi et al.[65] who observed LiAl mounds and nodules using the cross-sectional SEM. As demonstrated, the formation of SEI and  $\alpha$  phase take place at the surface of the Al thin film electrode (Figure 3.3a-b), and then the growth of  $\beta$ -LiAl initiates 3-dimensionally from the nucleation points at the electrode-electrolyte interface until approaching the substrate underneath (Figure 3.3c-d). Thereafter, a 2D growth (from 3D) gets involved and predominates the whole phase transformation process until the end of phase transition (Figure 3.3e-f).

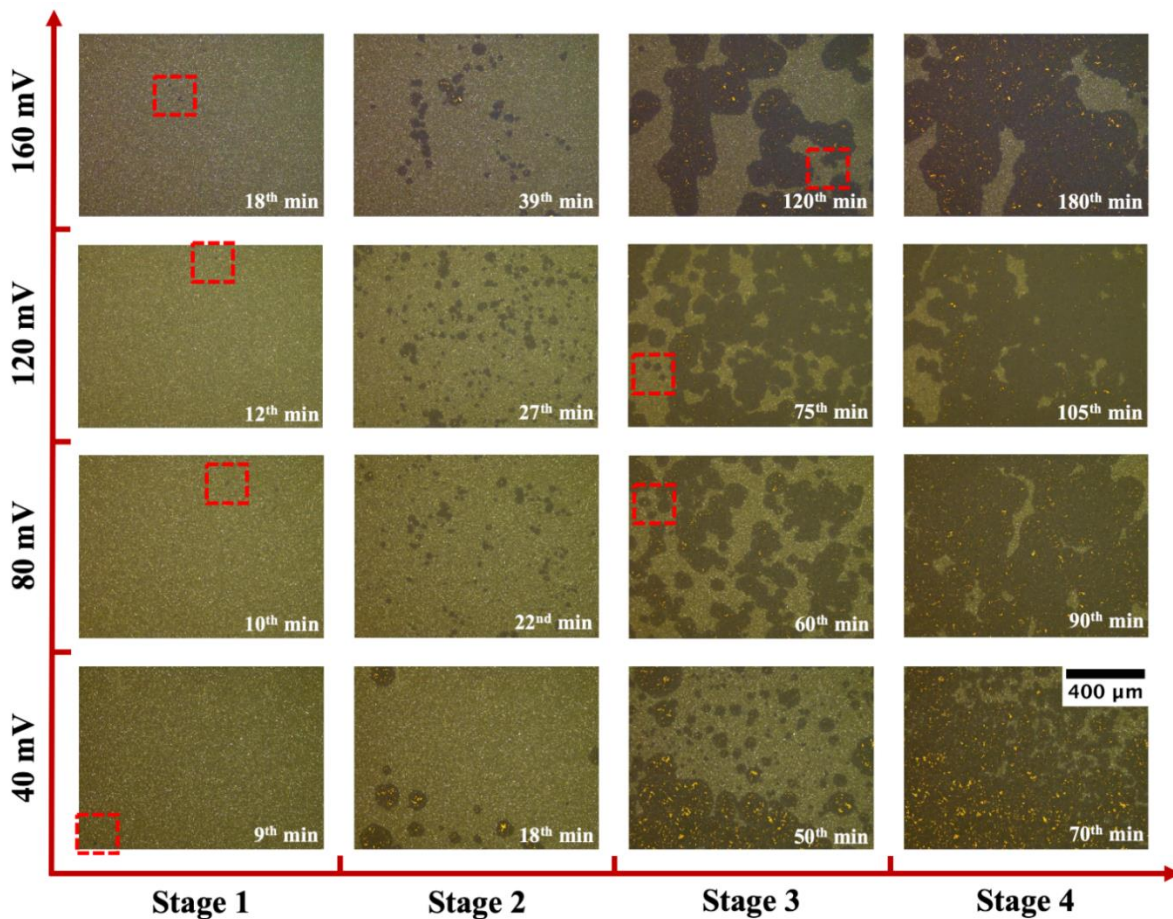


Figure 3.2. *Operando* light microscopic images (100x) of the sputtered Al thin film surface taken at different stages under various applied potentials vs.  $\text{Li}/\text{Li}^+$ ; the initial appearance of nuclei and the progressive nucleation are highlighted by dashed red rectangles in the first and the third column, respectively. The complete phase transformation processes are recorded as videos that can be found online as Video S1-S4 in the Supporting Information of [50].

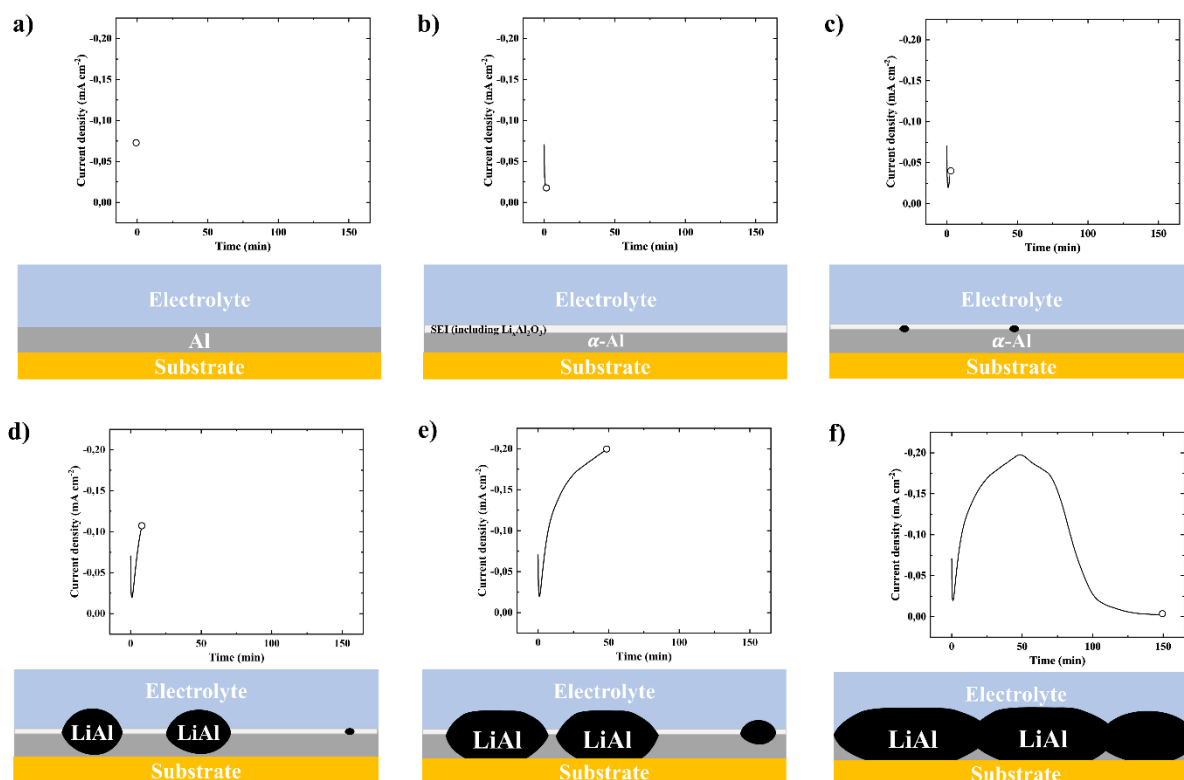


Figure 3.3. Potentiostatic curves (using 120 mV as an example) and schematic illustrations of Al thin film anodes at different time points during lithiation: (a) pristine Al electrode, (b) Al electrode before  $\beta$  phase nucleation (end of stage 1), (c) after nucleation (beginning of stage 2), (d) 3D growth associated with progressive nucleation (the connection between stage 2 and stage 3), (e) 2D growth in the thin film plane (stage 3), and (f) complete phase transformation (stage 4).

### 3.2.1 Stage 1 – Initial Lithiation

**Image analysis.** Since stage 1 presumably includes no phase transformation within the Al thin films, and the SEI is too thin to be visible, the surface of the electrode should not change. This argument is supported by the obtained *operando* videos, which show no visible change at the beginning of all potentiostatic tests for some time. The first column of Figure 3.2 makes it clear that the first visible nucleus appears in the observed region at the 18<sup>th</sup> minute, 12<sup>th</sup> minute, 10<sup>th</sup> minute and 9<sup>th</sup> minute after applying 160 mV, 120 mV, 80 mV, and 40 mV vs. Li/Li<sup>+</sup>,

respectively. Although the observed region can hardly represent the whole Al film, this sequence still supports the view that higher overpotentials may result in shorter activation times for nucleation. The appearance of nuclei indicates the start of stage 2 that will be discussed later.

**Electrochemical analysis.** The end of stage 1 (or beginning of stage 2) can be represented by the time point when the absolute value of the current is approaching its minimum in the potentiostatic transient, referring to the nucleation time, which is extracted from Figure S3.1c-d and summarized in Table S3.1. The outcome shows consistency with the *operando* images, except that the nucleation times required under the applied potentials below 80 mV (optical cells) and 100 mV (coin cells) become too similar to distinguish. As for the reaction kinetics, Equation 3.1 (Cottrell equation) can be used to analyze stage 1 without an Al phase transformation involved yet:[55]

$$j(t) = \frac{i(t)}{A} = \frac{zFc\sqrt{D}}{\sqrt{\pi t}} \quad (3.1)$$

where  $z$  is the number of electrons for the reaction,  $F$  is Faraday's constant,  $A$  is the area of the planar electrode,  $c$  is the concentration of Li in the  $\alpha$  phase at the surface of the sample, and  $D$  is the diffusion coefficient of the Li in the host metal Al. This equation describes the electrical current density  $j$  or the current  $i$  to a planar electrode with respect to time during diffusion-limited potentiostatic experiments.

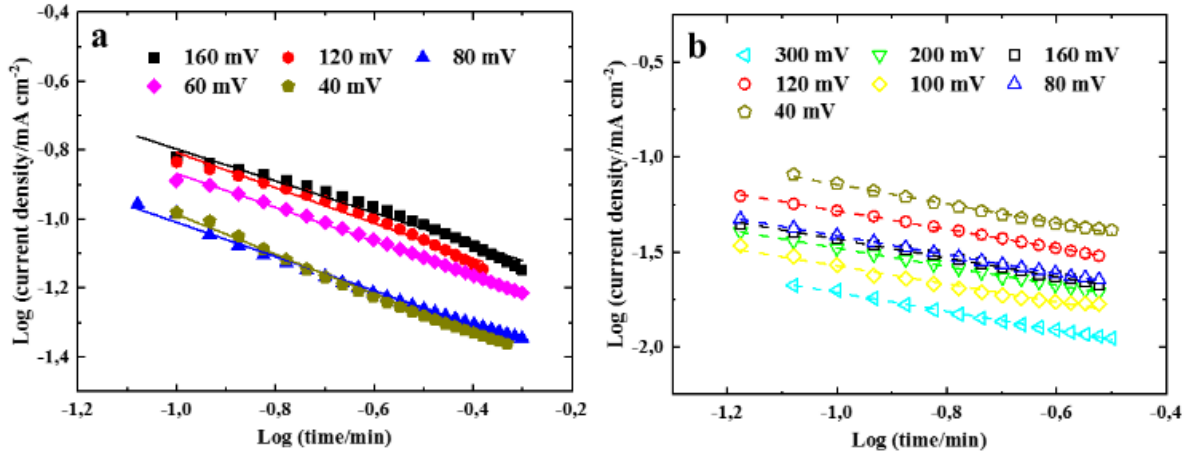


Figure 3.4. The logarithmic relations of current vs. time of the potentiostatic tests for (a) optical cells and (b) coin cells during stage 1, of which the slopes are all  $-0.5 \pm 0.03$  under various applied potentials.

Although previous kinetic evaluations suggested that formation of the  $\alpha$  phase dominates stage 1,[55, 66] currents contributed by SEI formation and lithiation of Al oxides should not be neglected. The initial lithiation is most likely diffusion-controlled by counting for all the possible reactions, such as  $\alpha$  phase lithiation and SEI formation. Hence, the  $i-t$  relationship should follow  $i \propto (c_1\sqrt{D_1} + c_2\sqrt{D_2} \dots)t^{-\frac{1}{2}}$ , with the concentrations  $c_1, c_2, \dots$  and the diffusion parameters  $D_1, D_2, \dots$  for the contributions of the different reactions. The logarithms of current vs. time during the first minute of the optical cells (Figure 3.4a) and the coin cells (Figure 3.4b) all yield slopes close to  $-0.5$  for all the tested potentials (Figure S3.2), regardless of the cell architectures. Calculations based on Eq. 3.1 were done to obtain the diffusivity values during stage 1, which fall into the regime between  $1.5 \times 10^{-11}$  and  $4 \times 10^{-11}$   $\text{cm}^2 \text{s}^{-1}$ . Although the diffusivity values are the approximations that include all the overlapping processes, they agree with previously reported ones, e.g.,  $2.4 \times 10^{-11}$   $\text{cm}^2 \text{s}^{-1}$ , [39, 55, 67] and are at least 3 orders of magnitude slower than the diffusion speed of Li in the  $\beta$ -LiAl.[42, 68] This consistency again supports diffusion-controlled kinetics during stage 1.

Lastly, to quantify the influence of the native aluminum oxide on the kinetic processes

in this first stage, a 50 nm Al<sub>2</sub>O<sub>3</sub> layer was deposited on top of the as-deposited Al film using atomic layer deposition (ALD). As shown in Figure S3.3a, the duration of stage 1 for ALD-coated Al films are longer than those with only the native oxide layer, regardless of the applied potentials. The longer nucleation time is most likely caused by the diffusion-limited process in the thicker Al oxide layer. Figure S3.3b clarifies that these oxide layers play an important role during the initial lithiation since the extra 50 nm of Al<sub>2</sub>O<sub>3</sub> consumes more charges than the Al films with only their native oxide layer at nearly all applied potentials.

### 3.2.2 Stage 2 – Electrochemical Nucleation and Initial Growth of the $\beta$ Phase

**Image analysis.** Stage 2 deals with the nucleation and initial growth before the  $\beta$  phase patches start to coalesce. It is suggested by Geronov et al. that stage 2 mainly consists of progressive nucleation and subsequent 3D growth,[56] which generally agrees with our *operando* observations. However, 3D growth is expected to be a short process and will eventually become 2D growth due to the thin film geometry in this study. It can be clearly seen from the first (beginning of stage 2) and the second (end of stage 2) column of Figure 3.2 that a large number of nuclei appear during a relatively short period (less than 30 min), except at 40 mV applied potential. Figure S3.4, which shows the  $\beta$  phase patch number vs. time relationship, can provide evidence for progressive nucleation during this period.

**Electrochemical analysis.** Geronov et al. suggested for their bulk electrodes that stage 2 includes either a 3D growth plus progressive nucleation (Equation 3.2) or a 3D growth plus instantaneous nucleation (Equation 3.3), but no conclusion could be drawn.[56] Our *operando* light microscopy is an ideal tool to provide direct proof with respect to the question of nucleation, which can be analyzed in conjunction with the electrochemical data from both cell configurations, such that:

$$\text{3D progressive: } i(t) = \frac{1}{3} zF\pi \frac{\rho}{M} V_1 V_2^2 J t^3 \quad (3.2)$$

$$3D \text{ instantaneous: } i(t) = zF\pi \frac{\rho}{M} V_1 V_2^2 N_0 t^2 \quad (3.3)$$

Where  $z$  is the charge of the ion ( $z=1$  for Li/Li<sup>+</sup>),  $\rho$  and  $M$  are the density and molecular weight either of the Al that is converted or of the LiAl phase that is created,  $V_1$  and  $V_2$  are the growth rates of the new phase at different directions,  $J$  is the nucleation rate, and  $N_0$  is the instantaneous number of nuclei.

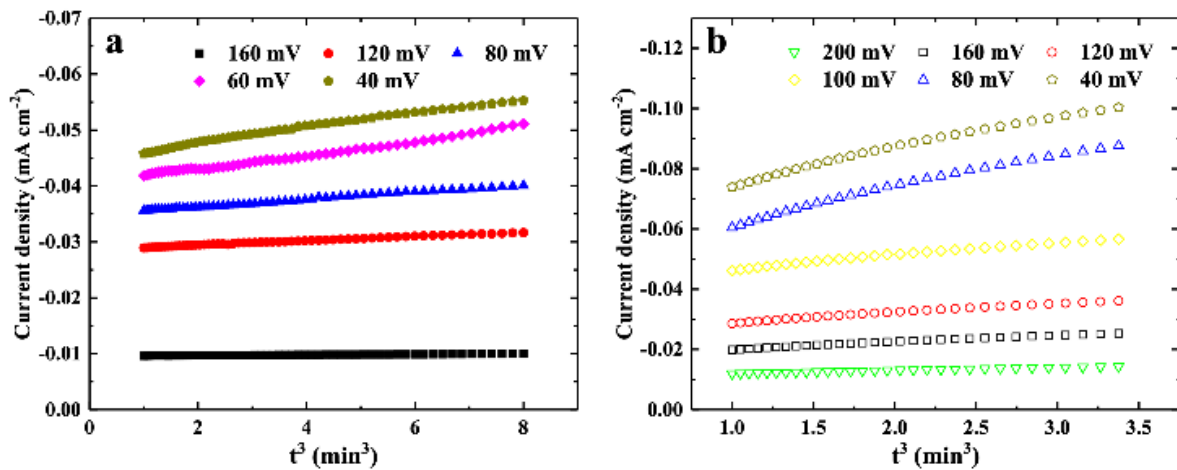


Figure 3.5. The  $i-t^3$  curves of the potentiostatic tests during stage 2 for (a) optical cells and (b) coin cells, which exhibit linearity under all the applied potentials; the time zero is defined as the minimum current that connects stage 1 and stage 2.

In nearly all cases, the number of patches stops increasing after ~30 minutes (Figure S3.4). The difference at 40 mV and more details will be discussed together with the next stage. By defining the moment where the minimum current is reached (beginning of stage 2) in the potentiostatic transient as time zero, the  $i \propto t^3$  described in Equation 2 is probably the case since ideal linearities are obtained at all applied potentials for both the optical cells (Figure 3.5a) and the coin cells (Figure 3.5b). The linearities here are perhaps contributed by the 3D growth of the nuclei before approaching the current collector during an extremely short period of time, plus progressive nucleation.

### 3.2.3 Stage 3 and 4 – Stable Growth of the $\beta$ Phase

These stages are the most significant ones since they occupy the major portion of the lithiation process which represents the plateau region of the potential vs. time curve during galvanostatic cycling. Stage 3 includes a rising current in Figure 1h and the ongoing growth of the  $\beta$  phase patches with the crystalline  $\text{Li}_x\text{Al}$  ( $x \approx 1$ ) intermetallic compound. Since these patches will grow and overlap, causing a decrease of the conversion rate and the corresponding current in stage 4, any mathematical analysis of the charge or current needs to take this process into account. This is done by using the model first developed by Kolmogorov, and later by Johnson, Mehl, and Avrami (JMAK model).[69-71] This model assumes that the propagation of the phase front follows a constant rate (“velocity  $v$ ”). Therefore, to apply this model to our thin films, it must first be confirmed that the radii or perimeters of circular  $\beta$  phase patches expand at a constant rate.

**Image analysis.** The obtained *operando* images show that the  $\beta$ -phase LiAl patches expand two-dimensionally: Often, they have a quasi-circular shape. Therefore, the in-plane ( $xy$ ) growth is considered isotropic hereafter (the growth in the  $z$ -direction likely has a different transformation rate). By measuring the perimeter of the patches and plotting it versus time, linear graphs are obtained (Figure S3.5), which confirms that the phase front velocity is a constant for a given potential. For the growth in the  $z$ -direction, a constant rate (corresponding to a quite constant current) has been confirmed earlier.[55] It has been suggested by Asthakov (as reported by Geronov et al.) that this rate is proportional to the potential (for details see Appendix-I: Supporting Information of Chapter 3) and that the phase transformation process from  $\alpha$  to  $\beta$  is most likely controlled by the reaction front at the phase boundary.[54-56] 2D growth in Al thin films was also observed *ex situ* by SEM in a study that pointed out the randomness of the position of nuclei and the non-uniformity of the patch sizes.[32]. Apart from the 2D circular growth of the  $\beta$  phase, progressive nucleation and patch coalescence are also

observed during stage 3. By carefully watching the *operando* videos, one can notice that an important part of the growth of the  $\beta$  phase is due to the expansion of the initially formed nuclei. This progressive nucleation is also visible in the third column of Figure 3.2. In stage 4, the  $\beta$ -phase LiAl patches keep coalescing with each other and finally consume all the  $\alpha$  phase.

**Electrochemical analyses.** The experimental lithiation electrical charge densities ( $q$ ) as a function of time at the applied potentials are plotted in Figure S3.6a-b for the optical cells and the coin cells, respectively. A part of the potentiostatic transients is occupied by approximately linear relationships that accelerate with a decrease of potential (i.e., an increase of the overpotential). This trend can be further confirmed by plotting current densities ( $i$ ) vs.  $q$  (Figure S3.6c-d). It can be clearly seen that the current rises faster with a higher overpotential, under which the peak current is also higher at the given extent of lithiation, regardless of the cell geometries. The JMAK analysis can be used for the evaluation here. It describes how solids transform from one phase to another with the dynamic interface area, including the coalescence of the new phase. The concept is ideal to shed light on the growth kinetics of the  $\beta$  phase in the Al thin film, and we can apply it to the electrochemical data and to the areal growth obtained from the microscopic images since both data sources allow the calculations of the volume fraction of the new phase during the whole phase transition process.

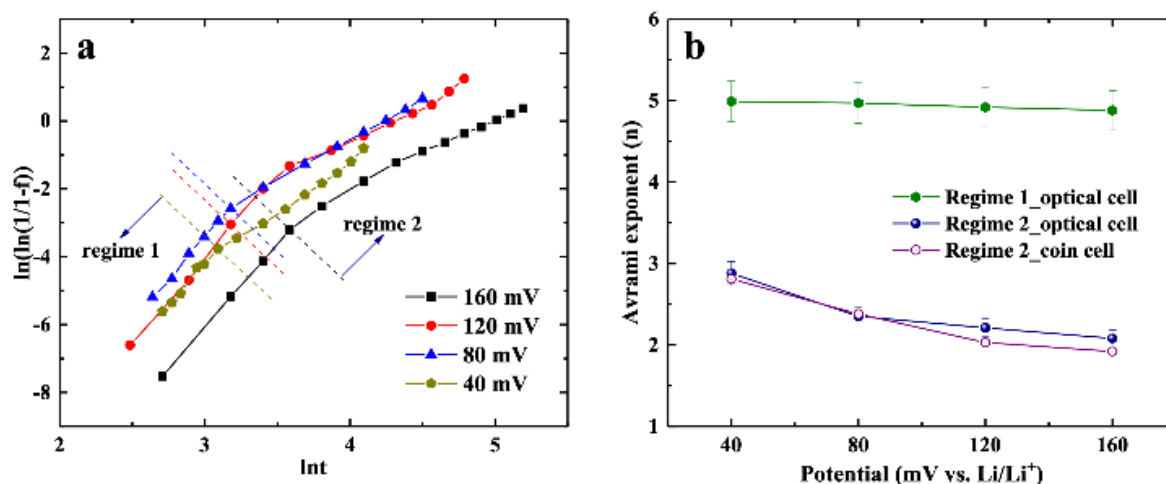


Figure 3.6. (a) The double logarithmic transformation plots obtained from the *operando* images

of optical cells of which the Avrami exponents ( $n$ ) can be determined from the slopes, for potentiostatic measurements at 160 mV, 120 mV, 80 mV, and 40 mV, which includes 2 linear regimes; (b) the Avrami exponents vs. the applied potentials for both optical and coin cells; the error bars represent the measuring errors from multiple times of manual measurements.

The transformation from  $\alpha$  to  $\beta$  phase exhibits typical isothermal behaviors (Figure S3.7a), where the slower rates at the beginning and the end of the whole processes are attributed by the nucleation of the  $\beta$  phase and the completion of the  $\alpha$  phase, respectively. Following the method of Avrami analysis (details in Appendix-I: Supporting Information of Chapter 3), plots of the relationship between  $\ln[-\ln(1-f)]$  and  $\ln(t)$  are used to extract Avrami exponent  $n$  (Figure S3.7b-c). As indicated in Figure 3.6a, it can be readily seen that this Avrami plot should be split into two regimes. The large slopes during regime 1 ( $n \approx 5$ ) might be due to the pronounced nucleation during stage 2 and the short-term 3D growth before approaching the substrate, while the decrease of the Avrami exponents in regime 2 results from the 3D to 2D growth[72, 73] as well as the lower nucleation rate observed from *operando* images. Regime 1 of Avrami analysis and stage 2 might be overlapping, but not necessarily the same process. Figure 3.6b summarizes that all the slopes obtained from the regime 2 are in the range of  $n=2-3$  that are indicative for a 2D growth of  $\beta$ -phase LiAl and agree with the quasi-circular expansion observed by the *operando* microscopy. To minimize the interference with the initial currents which include SEI formation and double layer charging, the latter portion of the  $q-t$  curves is used in Avrami analysis for the coin cells (Figure S3.7d) and yields similar Avrami exponents.

In addition to the geometry of the phase transformation, the Avrami exponent ( $n$ ) can also help to elaborate on the rate-limiting steps using the equation:[74, 75]

$$n = a + bc \tag{3.4}$$

Where  $a$ ,  $b$ , and  $c$  represent the nucleation rate, the growth geometry, and the rate-limiting step, respectively. The value of  $a$  can be obtained from the relationship of the number of nuclei per area versus the time,  $a=0$  for no nucleation,  $0<a<1$  for decreasing nucleation rate,  $a=1$  for constant nucleation rate, and  $a>1$  for increasing nucleation rate.  $b=1$ ,  $b=2$  and  $b=3$  are correspondent to 1D, 2D and 3D growth, respectively. There are two well-characterized values of  $c$ , of which  $c=1$  is indicative for reaction-limited growth and  $c=1/2$  for diffusion-limited growth.[52, 74-77]

Regime 2, referring to stage 3 and a part of stage 4, is the equilibrium state during the phase transformation process and occupies the major portion of the lithiation process, which is of vital importance in LIB applications. Although progressive nucleation is also observed during this regime, most nuclei pop up in the earlier stage that reasonably yields  $0<a<1$  in Equation. 3.4. This behavior has been confirmed by the nuclei number vs. time relation (Figure S3.4). Moreover, both the *operando* observation and the electrochemical analysis suggest that nucleation is more pronounced with the decrease of potentials vs. Li/Li<sup>+</sup>. This trend can result in the  $a$  values in a sequence of 160 mV<120 mV<80 mV and should be close to 0 since no outstanding progressive nucleation was observed until ~50% to ~60%. Together with the Avrami exponent ( $n=2.12$ , 2.29 and 2.35 for 160, 120, and 80 mV, respectively) and a 2D growth ( $b=2$ ),  $c$  is calculated to be 1, implying that the  $\beta$  phase growth is most likely limited by the reaction front at the phase boundary in the potential range from 160 mV to 80 mV. Overall, the Avrami exponential analysis is consistent with the previous discussion.

At 40 mV, although both the nucleation rate and the growth rate are higher, giving a bigger  $a$  value close to 1 and a larger Avrami exponent ( $n=2.88$ ), the calculated  $c$  is still close to 1, indicating the reaction-limited growth mechanism. It should be noted that other reactions might complicate the Li-Al system at lower potentials (e.g., 40 mV) due to the possible Li-rich phases formation.[59] Li diffusion can be more difficult in Li-rich Li<sub>x</sub>Al ( $x>1$ ) which are

formed within the  $\beta$  phase and consume extra Li atoms, and/or are associated with the structural damage caused by the brittleness of these new phases.[35, 78] Generally, it can be noticed that the current density during stage 3 at 40mV could correspond to a C-rate equivalent of 3C (Table S3.2), which is well beyond the rate capability of many insertion materials, let alone alloy anodes. Thus, the imperfect fitting of the data from the 40mV condition to the kinetic models of stages 2 and 3 can be expected (detail discussion in Appendix-I: Supporting Information of Chapter 3).

#### 3.2.4 Stage 4 – Completing the Phase Transformation

**Image analysis.** Stage 4 is the last part of the phase transformation process which is characterized by declining currents and more coalescence of the  $\beta$  phase patches, indicated by the dark color that occupies almost the whole surface. The unlithiated portion of the  $\alpha$  phase remains unchanged during the whole lithiation process.

**Electrochemical analysis.** Stage 4 is represented by the current decreases of  $i-t$  curves in Figure 3.1h, referring to the depletion of the  $\alpha$  phase, which has been confirmed by the *operando* videos. The wide plateaus at the end of the  $q-t$  curves obtained from the coin cells shown in Figure S3.6b indicate that no  $\alpha$ -Al was left for further lithiation.

Details of the degradation mechanisms of Al anodes are still unclear. Previous studies argued that the interfacial strain generated by the volume expansion and contraction[79] can result in pulverization[31] and/or delamination[33, 80] of Al thin film electrodes, which will subsequently lose their contact from the current collector. Since our *operando* observation indicates that the unlithiated Al can hardly be affected by the lithiated portion, the cycling stability of Al anodes may be improved by limiting the extent of lithiation.

#### 3.2.5 Expansion Rates of Individual $\beta$ Phase Patches

As 3D growth is limited in thin film geometry, optimization of the  $\beta$  phase growth and expansion rate in 2D are essential towards understanding the phase transition kinetics and improving the cycling performance of Al anodes in LIBs. As it can be clearly seen that degradation is always localized to the  $\beta$  phase regions, regardless of the degradation mechanism, the expansion rates of the  $\beta$  phase patches were measured for multiple isolated patches during potentiostatic lithiation. Figure 3.7 shows the growth rate of individual patches (perimeters vs. time) at various applied potentials. Strong linearities ( $R^2 > 0.99$ ) are clearly observed for the case of 160 mV, 120 mV, and 80 mV. This observation can be well supported by the multiple sampling strategies and measurements (5 randomly selected  $\beta$ -LiAl patches) in Figure S3.5, supplementing the inset of Figure 3.7. The applied potential of 40 mV, on the other hand, seems to exhibit a two-stage behavior. One can notice that the earlier portion is perhaps still linear, whereas the linearity is gone when the patch perimeter grows beyond  $\sim 4 \times 10^{-2}$  cm. By comparing the expansion rate for different potentials, the data exhibit an evident behavior that the growth rates are similar for potentials  $> 80$  mV (40 mV in Appendix-I: Supporting Information of Chapter 3), despite the measurements being taken from various times and locations during the *operando* experiment.

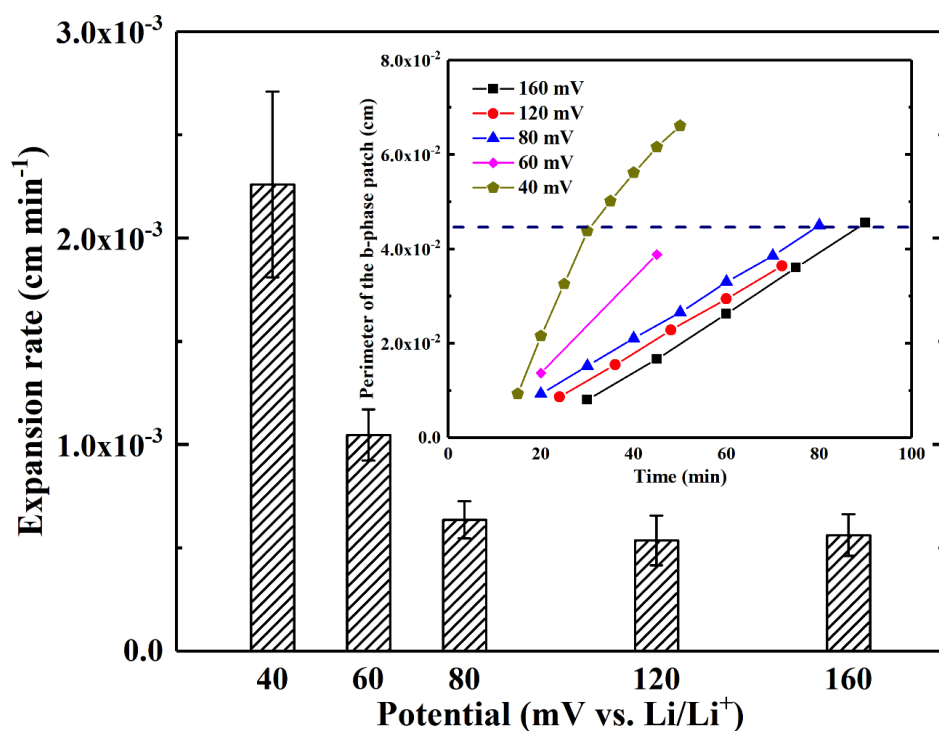


Figure 3.7. The expansion rate of individual  $\beta$ -LiAl patch' perimeter, obtained from the perimeter vs. time relations of the  $\beta$  phase patches from the *operando* images; the error bars represent the variations among five random  $\beta$  phase patches selected at different positions and time points.

The analysis of the  $\beta$  phase single patch expansion for Al thin films does not seem fully compatible with the bulk Al in previous studies,[54, 55] which report a linear dependence between the growth rates and the applied potentials. As evidenced here, single patches possess similar growth rates in the potential range between 160 mV and 80 mV. However, the total area (i.e., volume) of the  $\beta$  phase grows significantly faster at 80 mV than at 160 mV. This suggests that the nucleation rate contributes more to the overall growth of the  $\beta$  phase in this potential range. At applied potentials lower than 80 mV, the expansion rate of single patches also starts increasing dramatically and becomes another decisive factor that governs the phase transformation process. Nevertheless, this incompatibility could also arise from sample geometry and dimensionality and warrants further investigations.

### 3.2.6 Kinetic and Charge Control in Half Cell Experiments

The *operando* light microscopy combined with the electrochemical data allows for the phase transformation (lithiation) kinetic processes to be well described. The crucial features that may affect the lithiation of Al, and in turn, improve the performance of LIBs with Al anodes are highlighted:

- a. **Kinetic effect 1, nucleation:** Higher overpotentials lead to faster nucleation rates and higher nucleation densities (more nuclei formed in the observed region).
- b. **Kinetic effect 2, growth:** 2D growth rates accelerate significantly at low applied potentials and thus the transformation rate (from  $\alpha$  phase to  $\beta$  phase) may be governed by the current density when the two phases coexist.
- c. **Charge limit effect:** Inhomogeneous nucleation and 2D growth leave the unlithiated portion of the  $\alpha$  phase tightly adhered to the current collector during the growth of the  $\beta$  phase, such that degradation is localized to the  $\beta$  phase regions and the integrity of the  $\alpha$  phase is maintained.

Upon understanding these features, improved cycling stability of Al thin film anodes can be achieved by optimizing the amount of charge transfer and the kinetic conditions. There are several criteria that need to be taken into consideration: (a) proper nucleation potentials, (b) coalescence of the  $\beta$  phase patches, and (c) extent of lithiation. In other words, to facilitate the initial nucleation with a low nuclei density, a low overpotential should be applied. A current density that is similar in magnitude to the previous stage, should be used to avoid progressive nucleation during the subsequent phase transformation. Furthermore, a partial lithiation should be employed to minimize the coalescence among  $\beta$  phase patches, such that a continuous matrix of the  $\alpha$  phase can be maintained. Better ductility and stronger adhesion to the substrate of the surrounding  $\alpha$  phase can accommodate more mechanical stress which originates from the volume expansion of the isolated  $\beta$  phase patches, thereby one might expect that the

stability and reversibility of Al thin film anodes can be improved. Accordingly, a  $\beta$  phase volume fraction of  $\sim 55.6\%$  has been targeted to avoid patch coalescence (i.e. each  $\beta$  phase patch is presumably surrounded by the  $\alpha$  phase). This extent of lithiation may correspond to a specific capacity of  $\sim 552 \text{ mAh g}^{-1}$  ( $\sim 1.5$  times higher than conventional graphite anodes), in the absence of irreversible capacity loss (e.g., SEI formation, oxide lithiation, etc.).

These conditions were used to fix electrochemical parameters during galvanostatic cycling for our Al thin films using half cells. As shown in Table S3.1, some formation time is required prior to nucleation. Hence, a 15-minute potentiostatic hold at 200 mV was used to nucleate the  $\beta$  phase during the first cycle, followed by galvanostatic lithiation and delithiation cycles at a rate of C/5. In accordance with Table S3.2, a rate of C/5 is equivalent to the current observed during the 200 mV potentiostatic tests in coin cells and should satisfy the criteria to optimize kinetic effects 1 and 2 described previously. The full lithiation of the Al thin films in conventional half cells (using Li metal as the counter electrode) was conducted first, where the potential was approaching as low as 10 mV vs. Li/Li<sup>+</sup> before delithiation, yielding a specific lithiation capacity close to the theoretical value ( $\sim 993 \text{ mAh g}^{-1}$ ). It can be seen from Figure 3.8a that the delithiation capacity already drops dramatically after the initial full lithiation. Figure 3.8b displays the voltage profiles during partial lithiation and the delithiation to 1.5 V. Unlike full lithiation, the cell maintained the lithiation plateau potential ( $\sim 0.26 \text{ V vs. Li/Li}^+$ ) at the end of the 10<sup>th</sup> cycle, delivering similar capacity as the 1<sup>st</sup> cycle. For the 20<sup>th</sup> cycle, however, slightly lower potentials are required to keep the lithiation current, especially near the end of the lithiation process, and the cell finally stopped working after 25 cycles. It can be clearly seen from the inset of Figure 3.8b that the surface of partially lithiated Al film is not completely covered with the  $\beta$  phase, verifying our approach for stabilizing Al-based anodes. The comparisons are summarized in Figure 3.8c, which shows that the Al thin film electrodes with full lithiation at C/5 start degrading at the first cycle, of which the delithiation capacity and the

CE are lower than  $650 \text{ mAh g}^{-1}$  and 70%, respectively. The specific capacity keeps decreasing noticeably during the following cycles, and the cell subsequently stopped functioning after 5 cycles. On the contrary, the partially lithiated sample exhibits 20 cycles with the significantly improved CE, which is close to 100% for the 2<sup>nd</sup> to 6<sup>th</sup> cycles and is higher than 90% until the 15<sup>th</sup> cycle. These results demonstrate that cycling stability of Al thin film electrodes can be significantly improved by controlling the extent of lithiation and the nucleation/growth kinetics.

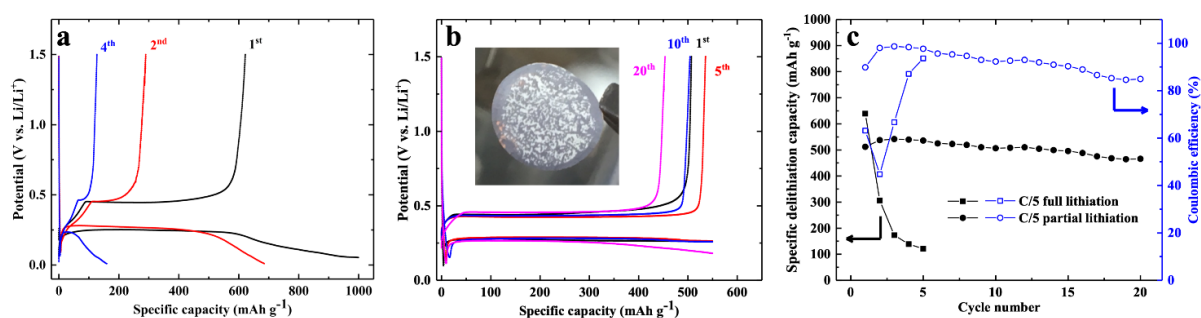


Figure 3.8. Galvanostatic (de-)lithiation capacity at C/5 with (a) the full and (b) the 55.6% partial lithiation for the half-cell with Al thin film electrodes at different cycle number; (c) cycling performance for the full (de-)lithiation and the partial (de-)lithiation at C/5 for coin cells with their corresponding coulombic efficiencies (CE).

### 3.3. Conclusion

The phase transformation kinetics and mechanisms of Al thin film lithiation have been investigated potentiostatically using *operando* light microscopy, supplemented by data obtained from conventional coin cells with the same testing conditions. The electrochemical data of both the optical cells and the coin cells agree with a model modified from those of previous studies. The stages are dominated by SEI growth, nucleation of the  $\beta$  phase patches, their growth, and their merging. We have provided a series of *operando* videos that visualize the phase transformation processes and these stages. Based on the results, schematic illustrations have been developed to discuss the underlying mechanisms. It has been found that

the nuclei of the  $\beta$  phase grow three-dimensionally, and subsequently, a quasi-circular 2D growth takes over and predominates the lithiation process owing to the aspect ratio of thin films. Avrami analysis via direct measurement of the area of the  $\beta$  phase patches has also been done and shows consistency with the electrochemical data and *operando* images. Since this study contains insightful information regarding the electrochemical lithiation of Al, it may be possible to optimize the performance of Al-based anodes in LIBs for some cycling conditions and applications. We demonstrate that the cycling stability and the coulombic efficiency of Al thin film electrodes can be improved by controlling the extent of lithiation (e.g., 55% partial lithiation) and the nucleation/growth kinetics (e.g., proper nuclei density and gentle lithiation speed that minimize the  $\beta$ -LiAl patch coalescences). This study provides fundamental understandings and helps to facilitate future investigations of Al-based electrodes in the electrochemical energy storage field.

## 4. Lithiation mechanisms: granular phase transformation

The light microscopy in Chapter 3 suggests that the  $\beta$  phase growth is quasi-isotropic which was considered as isotropic for the sake of kinetic analysis. However, the expansion of the  $\beta$  phase is notably anisotropic at the granular level. Apart from the same light microscopic cell under higher magnification (400 $\times$ ), electron backscatter diffraction (EBSD) was also used to shed light on the grain textures, thus yielding more insights during the lithiation of polycrystalline Al electrode.

In this part, the galvanostatic mode is used to simulate the practical working conditions while the electrode surface was observed simultaneously. Through overlapping the EBSD orientation map with *operando* images, the physio-chemical nature of Al lithiation on a crystalline level can be uncovered. Based on our observation, relevant information regarding the lithiation pathway (i.e.  $\alpha$  to  $\beta$  phase) can be discovered, which can contribute to the strategies for the development and commercialization of Al-based anodes in LIBs. This chapter was published in [81].

### 4.1. Background

As mentioned, the capacity of Al anodes in LIBs is originated from the phase transformation from  $\alpha$  phase to the  $\beta$  phase. This process involves breaking of Al-Al bonds and an atomic rearrangement with the formation of Li-Al bonds, and exhibits anisotropic features at the granular level. This observation infers that there might be (un-)favored crystalline orientations and/or grain boundary (i.e., misorientations) for the  $\alpha/\beta$  interphase to propagate. The preference during a lithiation-driven phase transformation also exists in other alloy anode materials. For instance, Lee et al. tried to lithiate single crystalline Si nanopillars with various grain orientations and found that lithium diffusion along  $\langle 110 \rangle$  direction is preferred during the electrochemical lithiation.[82] A similar outcome was also reported by Goldman et al.[83]

However, to the best of the authors' knowledge, no existing information is available regarding anisotropy during the electrochemical lithiation of Al. It should be noted that Si single crystals are more commercially approachable due to the well-developed semiconductor industry. For Al, on the contrary, almost all commercially available products are polycrystalline. It is therefore more relevant to study polycrystalline Al, such that the knowledge can be directly extended to the effort of commercializing LIBs with Al-based anodes. Compared to single crystalline materials, the influence of grain boundaries and texture may be also expected.

## 4.2. Results and Discussion

Figure 4.1a illustrates the structure of the *operando* light microscopic cell, which allows simultaneous observation of the electrode surface during the electrochemical lithiation. The details of the electrode preparation and the *operando* cell assembly can be found in our previous studies, [47, 50] which proves that such a cell design functions similarly as conventional coin cells and thus yielding identical electrochemical responses. The typical galvanostatic charge and discharge (GCD) profile of an aluminum/lithium half-cell is shown in Figure 4.1b, where the lithiation ( $\sim 270$  mV) and the delithiation ( $\sim 430$  mV) plateaus can be clearly observed, referring to the alloying and the de-alloying processes of the  $\beta$  phase, respectively. In this study, we focus on the lithiation plateau, at which the  $\beta$  phase is forming.[24] It should also be noted that the potential dip right after applying current (black dashed circle) refers to the extra energy required for the nucleation of the  $\beta$  phase.[27] By placing such an *operando* cell under a high-resolution light microscope, the electrode surface can be monitored during the whole lithiation process. Figure 4.1c presents the light microscopic image of the pristine Al thin film electrode surface and the red dashed rectangle denotes the area that has gone through an EBSD scan prior to the optical cell assembly. The generated orientation map is shown in Figure 4.1d, which seems to show a random grain

texture distribution based on Figure 4.1e. It should be mentioned that a second cell with the same components and procedures was also built and run as an individual control experiment. Both Al thin film electrodes exhibit similarities regarding the grain size ( $2.16 \pm 1.14 \mu\text{m}$ ), texture, and distribution (Figure S4.1).

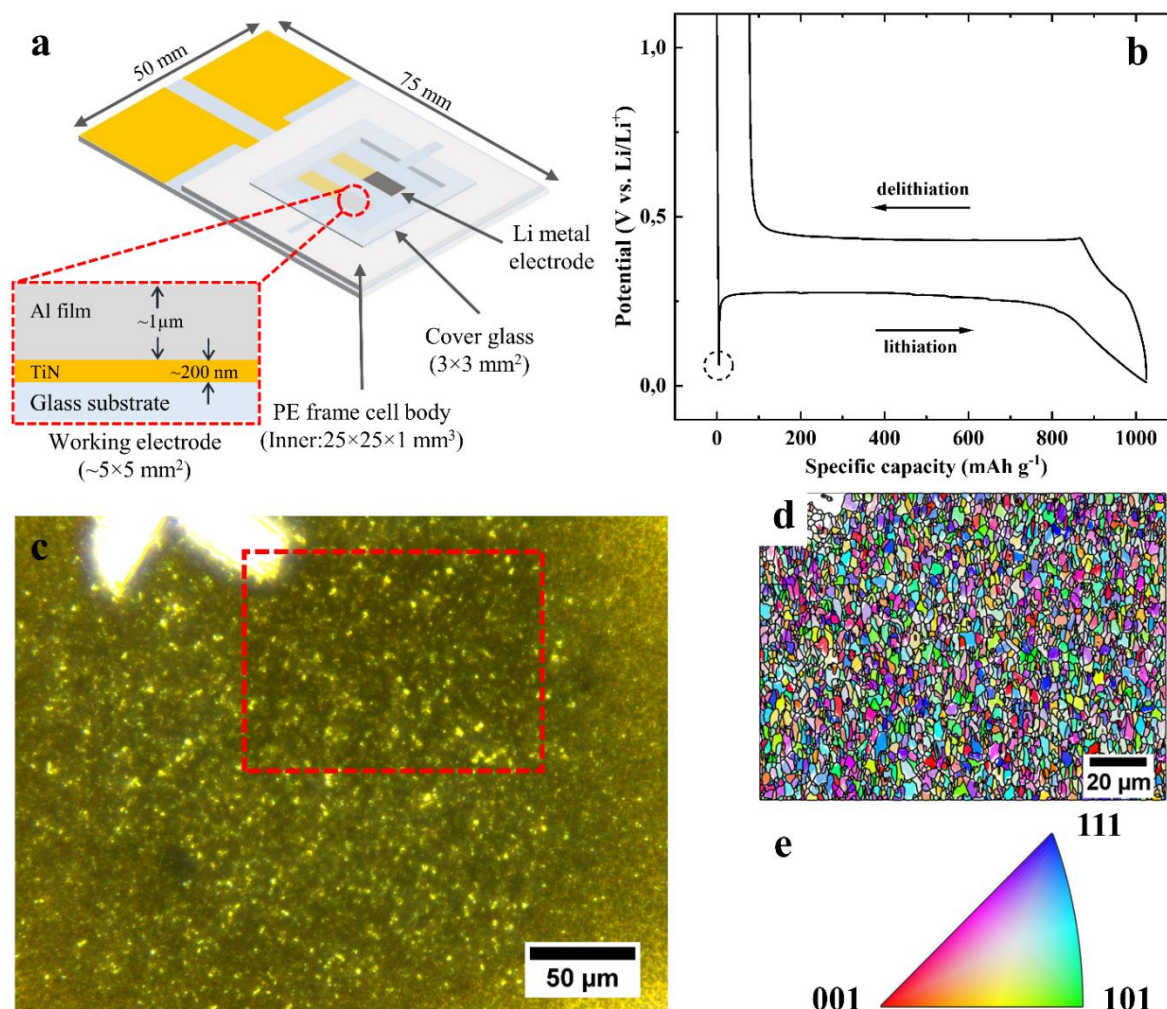


Figure 4.1. (a) Schematic illustration of the *operando* light microscopic cell, including TiN current collectors (gold) which own high electrical conductivity and decent electrochemical stability; the Al film (light grey) and Li metal (dark grey) are located at the tips; (b) typical potential profile of Al anode of a galvanostatic test; (c) a light microscopic image ( $400\times$ ) taken from the pristine surface of the Al thin films (red dashed circle); (d) the EBSD crystallographic orientation map along Z-axis that represents the grain textures within the area highlighted by

the red dashed rectangle; (e) the inverse pole figure (IPF) color key.

Previous studies point out that electrochemical lithiation starts with the  $\beta$  phase nucleating at specific locations and this is then followed by radial expansion which is quasi-isotropic at the low magnification (100x) under a light microscopic.[50] In this study, a higher magnification (400x) is used, under which we clearly observe that there are specific positions that exhibit the anisotropic features at the edge of the  $\beta$  phase patches (i.e.  $\alpha/\beta$  phase interface). It has been observed that certain grain clusters appear to be intrinsically more reluctant towards phase transformation, and these amounts of grains which are resistant to lithiation are termed “stubborn grains” hereafter. The *operando* images in Figure 4.2 reveal how the two representative stubborn grain clusters evolve during the phase transformation selected from the two cells. The time zero is defined as the moment when the phase interface hits the stubborn regions (Figure 4.2a1 and Figure 4.2b1). Subsequently, the stubborn grains suppress the specific locations from being transformed easily, whereas the normal phase transformation is observed for the nearby non-resistant locations (Figure 4.2a2 and Figure 4.2b2). The stubborn regions are clearly revealed from the enlarged images shown in Figure 4.2a3 and Figure 4.2b3. Finally, the stubborn grains are lithiated after a certain period, as indicated by the highlighted regions of Figure 4.2a4 and Figure 4.2b4 that are filled up with the dark color (i.e., the  $\beta$  phase).

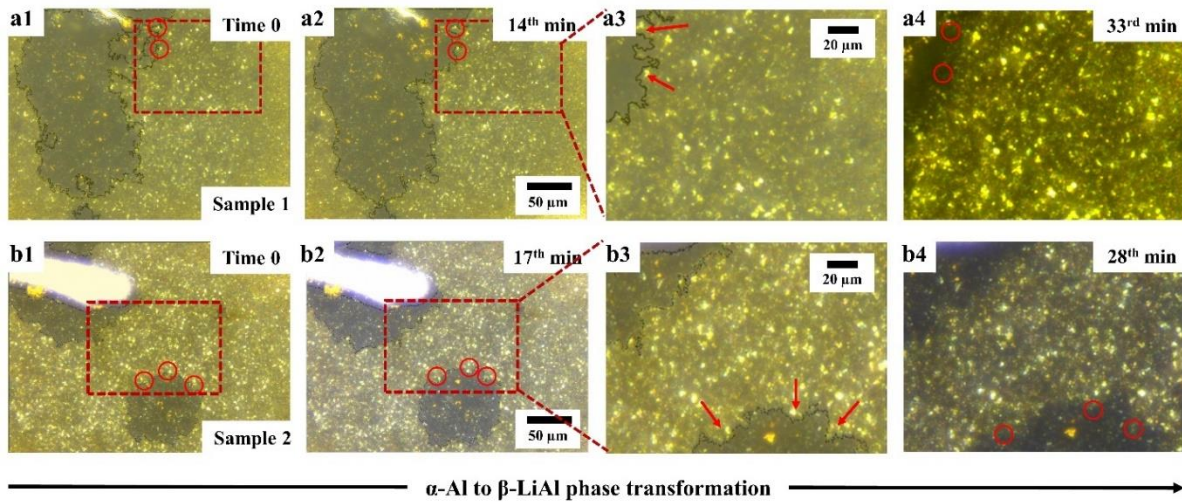


Figure 4.2. Two series of *operando* images taken during electrochemical lithiation of the Al thin films, where the dark regions refer to the  $\beta$  phase LiAl; the red arrows point out the specific locations where the lithiation are inhibited and extra time is required for the grains at these locations (stubborn grains) to be lithiated; image series (a1-a4) and (b1-b4) are taken from the electrode surface of sample 1 and 2, respectively; the complete *operando* videos are provided in the online version of [81].

Through using such an approach derived from Figure 4.2, all the stubborn grains can be selected and summarized statistically to explore their crystalline textures. The extra time required for all the stubborn grains to transform is  $\sim 17$  min on average (see Figure S4.2 for full distribution). In addition to these stubborn grains, other grains next to those resistant regions, which are presumably preferred for lithiation (i.e., preferred grains), are also selected to compare with the stubborn grains. Moreover, the same number of grains is selected randomly from the whole EBSD area (random grains). These three sets of data containing the information of out-plane orientations are presented and compared in Figure 4.3a1-a3 and Figure 4.3b1-b3. From the corresponding inverse pole figure (IPF) maps, one can notice that the stubborn grains show stronger  $\langle 111 \rangle$  texture compared to the preferred grains and the random grains. Among the preferred and the random grains, no clear trends can be determined even though their

distributions are slightly different.

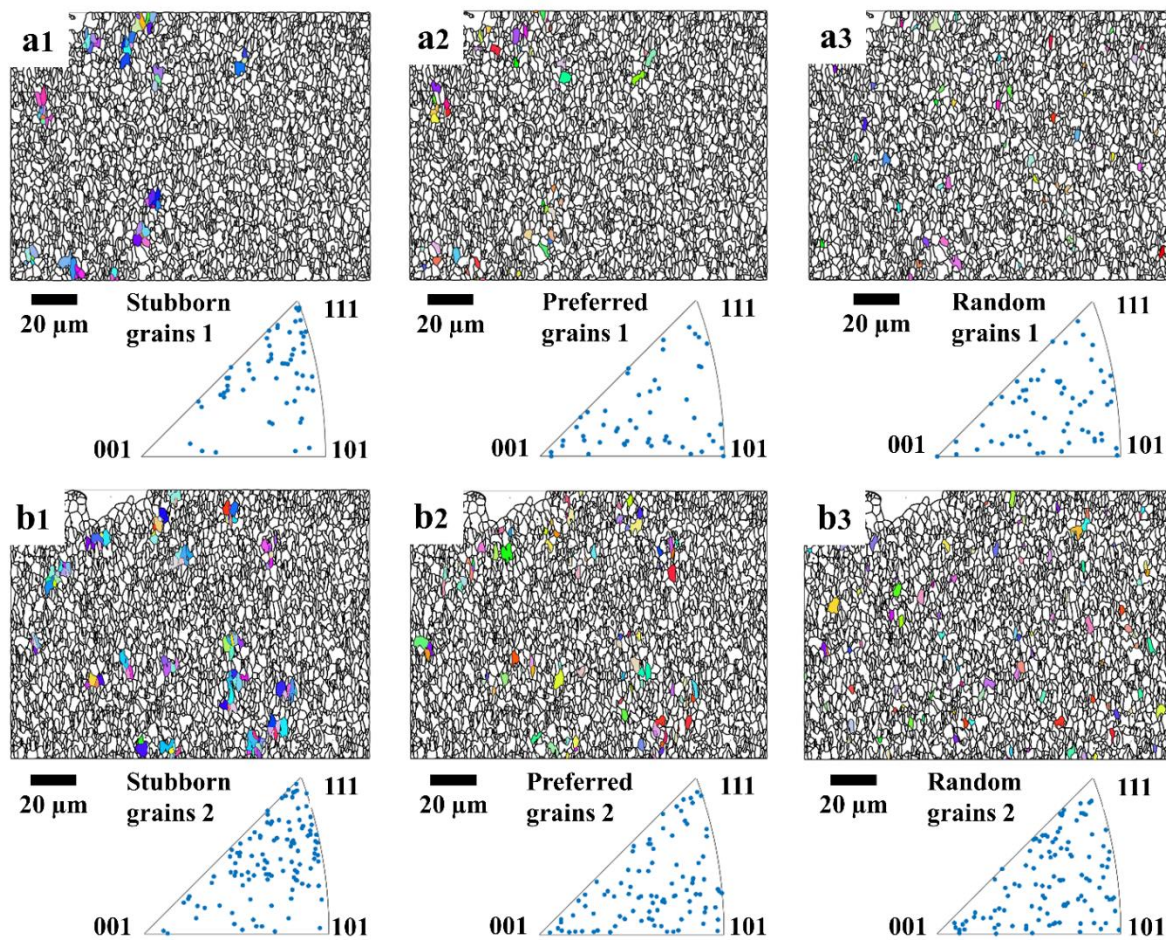


Figure 4.3. All the stubborn grains are selected and marked in (a1) and (b1) for the two samples, respectively; the corresponding IPF maps reveals that the stubborn grains have a preferred texture towards  $\langle 111 \rangle$  direction; the same analyses are also done for the preferred grains (the grains next to the stubborn positions) and the completely random grains, which are summarized in (a2, a3) and (b2, b3), respectively.

The crystallographic orientations of discrete grains in a thin film are known to be closely correlated with surface energy [84]. Thompson, et al. demonstrated a surface energy sequence for grain stability, whereby  $[001] > [110] > [111]$ , and  $\langle 111 \rangle$  texture has the lowest surface energy.[85] In other words,  $\langle 111 \rangle$  out-plane orientation is the favored texture for fcc metals (e.g., Al films) during the PVD sputtering process including nucleation and growth.[86]

This minimized surface energy makes the  $\langle 111 \rangle$  grains the most stable of all possible orientations. In other words, they are more difficult to be lithiated than other grains.[87, 88] This information agrees with our data that the grains with/or close to the  $\langle 111 \rangle$  orientation are more reluctant to phase transformation (i.e. stubborn grains). As for the grains with/or close to  $\langle 001 \rangle$  and  $\langle 101 \rangle$  orientations, no solid conclusion can be drawn from the available data. Since the preferred grains are selected from the regions next to the stubborn regions, they are considered as relatively “preferred” instead of absolutely “preferred”. The outcome can also be well supported by Kumagai et al. who stated that the transformation rate from the  $\alpha$  to the  $\beta$  phase depends on the crystallinities with the preferred orientation of  $\langle 100 \rangle$ . [89] They also reported that  $\langle 100 \rangle$  orientation gives a higher lithiation rate due to a larger effective surface area, thereby reducing the energy required for Li insertion. Nevertheless, the surface energy should not affect the lithiation behavior significantly since the Al film used in this study is  $\sim 1 \mu\text{m}$  thick.

Together with the kinetic analysis and the schematic model from a previous study,[50] three different scenarios of 2D (i.e. thin film) lithiation mechanisms are proposed in Figure 4.4 to shed light on the possible Li pathways. Firstly, the Li ions in the electrolyte may directly insert into the  $\alpha/\beta$  phase boundary, and/or the  $\alpha$  phase close to the phase boundary, to facilitate continuous phase propagation (Figure 4.4a; ‘mode a’). Alternatively, the Li ions may also insert into the existing  $\beta$  phase through a pinhole (i.e., initial nucleation point) and then diffuse to the  $\alpha/\beta$  phase interface to enable further radial expansion (Figure 4.4b; ‘mode b’). This mode is proposed because the solid-electrolyte interface (SEI) is too thin to be visible under a light microscope and previous studies suggest extensive deformation is localized at the center of the patches (i.e. from a pinhole).[32] Lastly, in the case of ‘mode c’ (Figure 4.4c), the whole surface of the  $\beta$  phase patch acts as sites to accept the Li ions from the electrolyte.

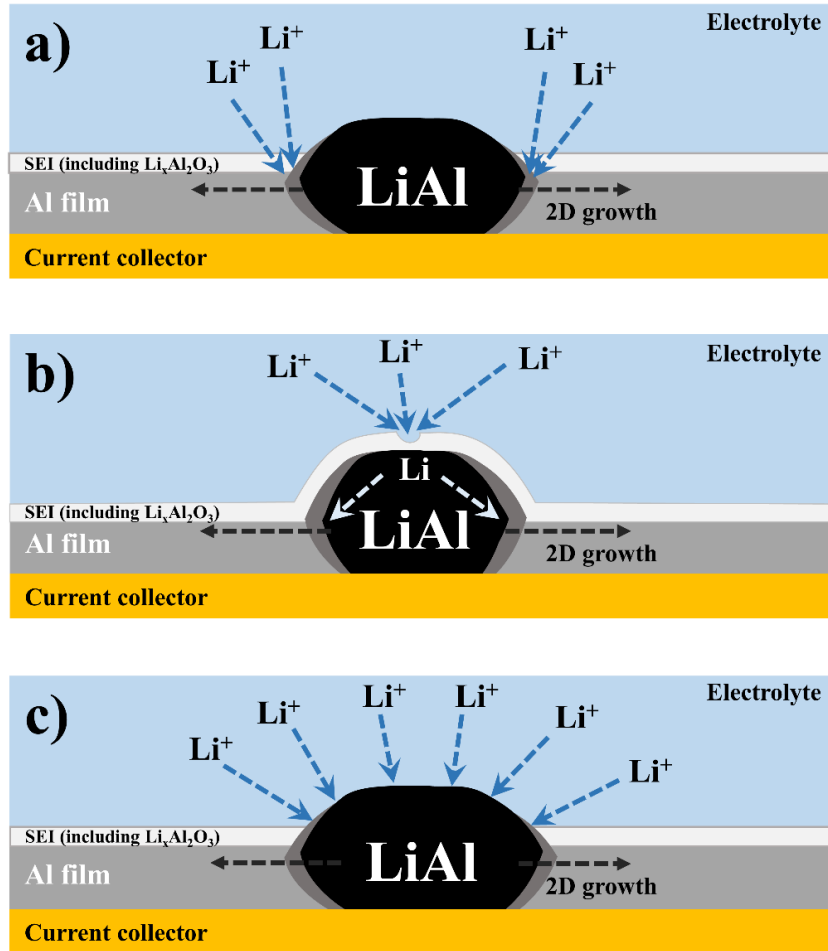


Figure 4.4. Schematic illustrations of lithiation mechanisms (points of Li insertion) of Al thin film anodes: (a) insertion directly into the phase boundary (i.e., reaction front), (b) insertion through a pinhole in the SEI on top of the  $\beta$  phase patches, (c) insertion into the whole surface of the  $\beta$  phase patches.

Our observations and analysis reveal that the transformation nature of stubborn grains is caused by out-plane orientation, as opposed to in-plane orientation or their grain boundaries (Figure S4.3 and Figure S4.4; detailed discussion in Appendix II – Supporting Information of Chapter 4), suggesting that Li ions most likely insert into the Al matrix directly from the electrolyte at the phase boundary (mode a) rather than into the existing  $\beta$  phase patches and then diffuse to the phase boundary (mode b). In addition, the exposure of the current collector

in the *operando* videos indicates that the defects of patches occur during the phase transformation, thereby destroying the pinhole. In a solid solution like LiAl, it is reasonable to presume that the Li insertion occurs at the phase interface where the largest concentration gradient is located.[61] In the case of mode a, the growth rate of the  $\beta$  phase patches is limited by the reactions at the phase interface, which can be well supported by the previous study.[50] However, we shall not eliminate the pinhole mechanism if the  $\beta$  phase patch is sufficiently small (i.e. prior to the pinhole destruction) since pinholes may exist and can be the preferred positions for initial nucleation from a thermodynamic point of view. As for mode c, it is known that Li diffusion in the  $\beta$  phase is several orders of magnitude higher than that in the  $\alpha$  phase,[39, 42, 68, 90] and the growing patches provide a thermodynamically favorable pathway for Li insertion, rather than nucleating the new  $\alpha$  phase where extra energy is required.[91] Although mode c should not have exhibited progressive nucleation, it seems to be the only way when an in-depth 1D phase propagation occurs (i.e. lithiation of thick Al foils). Therefore, the phase transformation is likely a hybrid process, covering all three scenarios due to the effects of SEI and Li diffusion.

Importantly, this EBSD investigation implies that the electrochemical  $\alpha$  to  $\beta$  phase transition in a Li-Al system seems to occur on a grain-by-grain basis (i.e., individual grains transform completely), regardless of the proposed modes. Thus, it should be considered that the mechanisms which control granular transformation are more significant to the lithiation process than the trans-granular atomic pathway itself.

The lithiation mechanism of Al might be compared with that of crystalline silicon, which strongly depends on the orientation. This is not due to a dependence of the lithium diffusion on the orientation, but because the velocity of the reaction front varies in different crystallographic directions of Si.[92] It is kinetically easier for Li atoms to penetrate and break up the crystalline Si lattice via  $\langle 110 \rangle$  and  $\langle 112 \rangle$  lateral directions than along  $\langle 111 \rangle$

directions.[92] In a similar way, it is unlikely that the diffusion within the Al  $\alpha$  phase influences the lithiation rate strongly (Figure S4.5, detailed discussion in Appendix-I: Supporting Information of Chapter 3). The grain-by-grain lithiation of Al is also expected to be affected by mechanical properties of the grains, not only during the initial nucleation, but also during the propagation of the phase front. The elastic moduli of most cubic materials, e.g., fcc Al, depend on the orientation with the largest value for  $\langle 111 \rangle$  plane (106 GPa)[93] and the smallest for  $\langle 100 \rangle$  plane (95 GPa)[93] – the Al atoms along  $\langle 111 \rangle$  plane are more densely packed. Due to the large strains during lithiation, the plastic deformation of Al might be more important here. For instance, creep rates are reported for Al for stresses  $\geq 40$  MPa at 300 K.[93] It is also reported that the strength and mode of failure of Al samples significantly depend on the grain orientation.[94] Grains in our thin film on the rigid substrate are stretched in the out-of-plane direction if a neighboring grain has been transformed to the  $\beta$  phase. If we assume that the grain boundaries can transfer a given amount of stress to the neighboring grains, Al  $\alpha$  grains with an  $\langle 111 \rangle$  orientation in the out-of-plane direction will be less strained elastically than those with an  $\langle 001 \rangle$  orientation. Since a larger strain might facilitate the lithiation more, this mechanical effect might explain the observed dependence of the lithiation rate on the orientation. All in all, the analyses suggest that the mechanical stress/strain should play a more important role in contributing to such an anisotropic lithiation at the granular level.

### 4.3. Conclusion

In conclusion, we have conducted an *operando* light microscopic experiment on electrochemical lithiation of Al thin films. By using an EBSD characterization, the orientation of Al grains before lithiation was determined and correlated with the lithiation behavior. Our statistical analyses suggest: 1) Al grains with  $\langle 111 \rangle$  out-plane texture are more reluctant to the transformation from the  $\alpha$  to the  $\beta$  phase; 2) In-plane orientations and grain boundaries do not

seem to play important roles as same as the grain orientation during the growth and propagation of the  $\beta$  phase. We suggest that the observations might be explained by the minimized surface energy of  $\langle 111 \rangle$  Al grains to a minor extent. Moreover, a dependence of the  $\alpha/\beta$  reaction interface velocity on the orientations of the grains might be influenced by a smaller strain of an  $\langle 111 \rangle$  out-of-plane orientation grain for a given stress. The discovery in this study provides insights that might help in engineering Al-based anodes that fulfill the performance requirements for multiple application purposes. For instance, facilitating homogenous Li diffusion by decreasing the prevalence of  $\langle 111 \rangle$  grains might help to achieve better reliability due to improved mechanical strain uniformity. The designated distribution of grain orientations can be engineered to manipulate the  $\beta$ -LiAl nucleation and subsequent phase propagation for multiple application purposes.

## 5. Delithiation mechanisms: stress analyses

Based on the observations above, it is the reverse transformation (i.e.  $\beta$  to  $\alpha$  phase transition) that may be the biggest concern and most critical to capacity fading: Hudak et al. suggest that this process is more problematic since the capacity decay is only observed during delithiation.[80] Moreover, the mechanical strain linked to volume changes during Li insertion/extraction is suggested to severely shorten the lifetime of Al anodes.[95] Thus, mechanical strain/stress during the electrochemical cycling of Al electrode is also of importance. This chapter has been published in [96].

### 5.1. Background

In our previous study, we explored the kinetics of the initial electrochemical incorporation of Li into Al and highlighted the factors that may affect the electrode stability.[50] Although the potentiostatic techniques with fixed driving forces used can be ideal for conducting kinetic analyses, they may not fully represent the typical working conditions for LIB applications. It is therefore also necessary to explore how Al electrodes behave under various electrochemical conditions, such as GCD and CV. In this work, we aim towards a better understanding of the delithiation and re-lithiation processes, which ultimately determines whether Al anodes are suitable for practical applications. The well-established *operando* platform consisting of a borosilicate glass-made optical cell and a high-resolution light microscope allows concurrent observations of the Al thin film electrode during electrochemical cycling. Furthermore, substrate curvature experiments are also performed *in situ* to measure the mechanical stresses during the phase transformations in both directions.

Here, we still use sputtered Al thin film electrodes as convenient substrate-based model systems to investigate the electrode-electrolyte interface and fundamental transformation mechanisms during cycling. Findings can then be extended to assess bulk Al, such as foils,

meshes, and other forms, for practical applications.

## 5.2. Results and Discussion

The typical cyclic voltammograms of Al in Figure 5.1a are obtained from a standard coin cell. They exhibit two sharp peaks at  $\sim 0.15$  V ( $\sim 0.2$  V for the 2nd cycle) and  $\sim 0.5$  V, referring to lithiation and delithiation, respectively. For the other cell types, (Figure 5.1b-c), although different rates were used, identical shapes are observed, strengthening confidence in the different cell designs.[14] The slightly different CV shape of the optical cell is determined to not be a result of cell architecture. Instead, CV scan rates (Figure S5.1a) and electrode forms (Figure S5.1b) should play a more important role here. Also, this particular CV shape is constantly observed by other studies.[12, 15] Correspondingly, the two wide plateaus observed in the GCD curves shown in Figure 5.1d-f are located at  $\sim 0.26$  V (lithiation) and  $\sim 0.48$  V (delithiation) vs. Li/Li<sup>+</sup>, regardless of the cell type. Nevertheless, poor coulombic efficiency is always one of the major issues for Al-based anodes. The potential-capacity profile exhibits a dip before the lithiation plateau, where the potential difference is defined as the nucleation potential by Wang et al.[16] This potential is clearly below the equilibrium and represents the extra energy required for the  $\beta$  phase nucleation,[17] which may have a large contribution from the energy required to initiate deformation of the local  $\alpha$  phase Al matrix.[18]

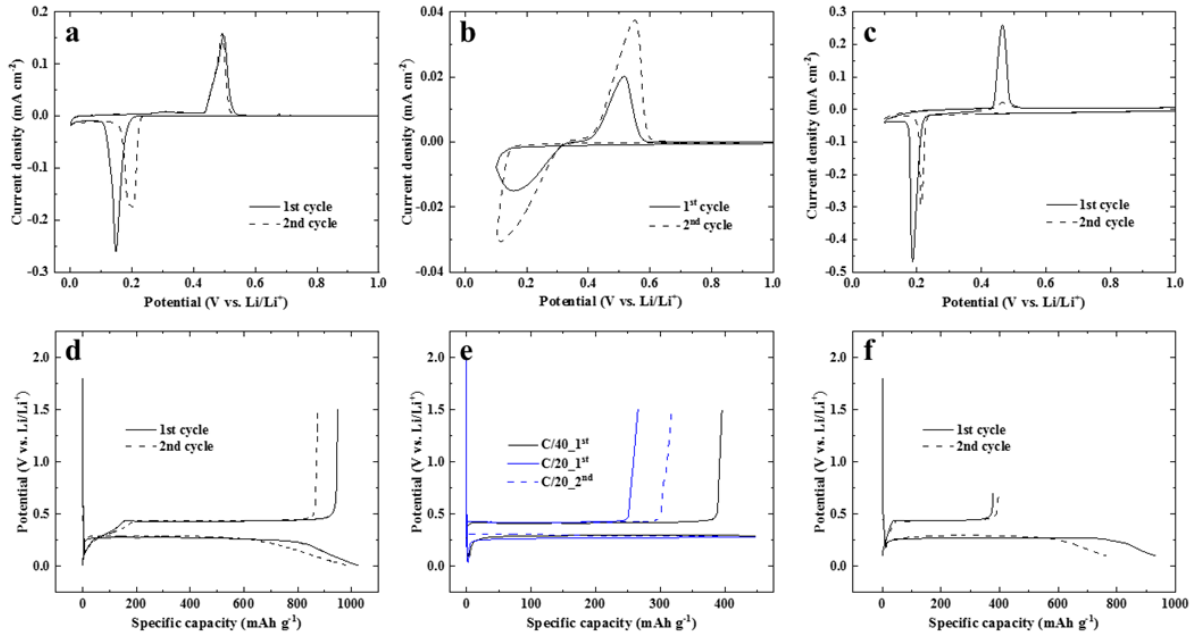


Figure 5.1. Typical electrochemical profiles for the (de-)lithiation of Al thin films including cyclic voltammograms and the GCD curves obtained from various cell types: (a) the conventional coin cell at  $0.01 \text{ mV s}^{-1}$  and (d) C/40, (b) the *operando* optical cell at  $0.5 \text{ mV s}^{-1}$  and (e) C/40 and C/20 (c) the *in situ* stress cell at  $0.05 \text{ mV s}^{-1}$  and (f) C/10. Multiple scan rates and C-rates are used to adapt to different cell types.

### 5.2.1 *Operando* light microscopy

*Operando* light microscopy monitors the electrode surface concurrently as (de-)lithiation processes are ongoing. The *operando* images at specific time points have been selected and are shown in Figure 5.2. As demonstrated in Figure 5.2a, the lithiation behavior agrees with our previous study, yielding the quasi-circular  $\beta$  phase patches at random positions under both GCD rates. The same study also suggests that the stability and reversibility of Al thin film anodes can be improved if these  $\beta$  phase patches are surrounded by the ductile  $\alpha$  phase.[50] Therefore, a partial lithiation is adopted to minimize the patch coalescence, and thus enabling several stable cycles for investigations of the delithiation and re-lithiation processes. The surfaces of Al films at the end of  $\sim 45\%$  partial lithiation show no visible degradation, i.e.

neither delamination nor pulverization at the chosen magnification is observed. For the delithiation, cracks are observed to form within the patches and subsequently become more and more prominent. Here, a golden color indicates the exposure of the underlying TiN current collector/adhesion layer. At the late stages of delithiation, the area of these uncoated regions is high which suggests that next to the cracks sliding along the substrate interface or film delamination occurs. Generally, the Al thin films exhibit similar features even when cycled under different C rates. Two complete sets of images that record the surface change of the Al thin film electrodes during (de-)lithiation are provided as video clips (can be found in the online version of [96]).

As the initial lithiation always includes irreversible solid-electrolyte interface (SEI) formation, lithiation of oxides, and perhaps  $\alpha$  phase lithiation (i.e., without phase transitions), which can consume significant fractions of the charge for a thin film electrode, the subsequent cycles should be more important and representative for practical reversible battery operation. Figure 5.2b visualizes the beginning of the second lithiation process at the rate of C/20, during which the Li insertion initiates in the existing patches. This is supported by the apparent closing of cracks resulting from the volume expansion of the re-lithiating patch. As the lithiation continues, additional nuclei are also observed within pristine Al regions. After the second delithiation, more severe degradation of the Al electrode is observed, such as new cracks within the new patches. The number of cracks and the amount of delamination accumulate over cycles, and it is suggested that this finally determines the lifetime of an Al thin film electrode.

The areal growth of the  $\beta$  phase within the observed region measured from *operando* images and the one calculated from the electric charge during the initial lithiation are plotted in Figure S5.2. As can be seen, both curves appear to be linearly correlated with time and possess the same slope for a galvanostatic test due to the constant current, except that there are lags at the beginning of the lithiation. This time lag may be attributed to the SEI formation and

the oxide lithiation that consume charges at early stages, and thus delay the phase transformation process. The individual  $\beta$  phase patches, however, exhibit a  $\Delta r \propto \Delta t$  relationship (Figure S5.3a) instead of the  $\Delta A \propto \Delta t$  expected for the whole thin film based on the constant current. As  $\Delta r \propto \Delta t$  is obtained for single patches while  $\Delta A \propto \Delta t$  is observed for the integrated  $\beta$  phase' area of the whole observed region, one may argue that the different expansion rates of individual patches observed in C/20 data (Figure S5.3b) can be responsible for the inconsistency between the single patch and the whole film. This behavior can also be supported by the analyses of our previous work, which suggests a reaction-controlled growth mechanism of the  $\beta$  phase patches.[50]

To shed light on the Li pathways that govern the  $\beta$  phase patches evolution during fast and repetitive cycling, CV is used in addition to GCD. The evolution of the Al film surface during the initial CV cycles is shown in Figure 5.2c, where a clear expansion of the  $\beta$  phase is observed. Later during delithiation, the  $\beta$  phase patch contracts radially with the fixed center point, although the contraction is not completely reversible. As illustrated, the expansion during the following cycle also initiates from the same center position and the patch becomes even larger. This observation supports the view that Li ions might be going through a fixed point (e.g., a pinhole) during (de-)lithiation, specifically for the first several cycles prior to the destruction of the pinhole.[81] It can be clearly seen from Video S5.3 and S5.4 that the  $\beta$  phase patches break after several CV cycles, and the TiN current collector becomes visible. It should be noted that the pinhole can hardly be preserved as soon as visible cracks are formed. These repetitive CV cycles also support that the lithiation preferentially initiates at the existing patches, consistent with findings from the GCD tests.

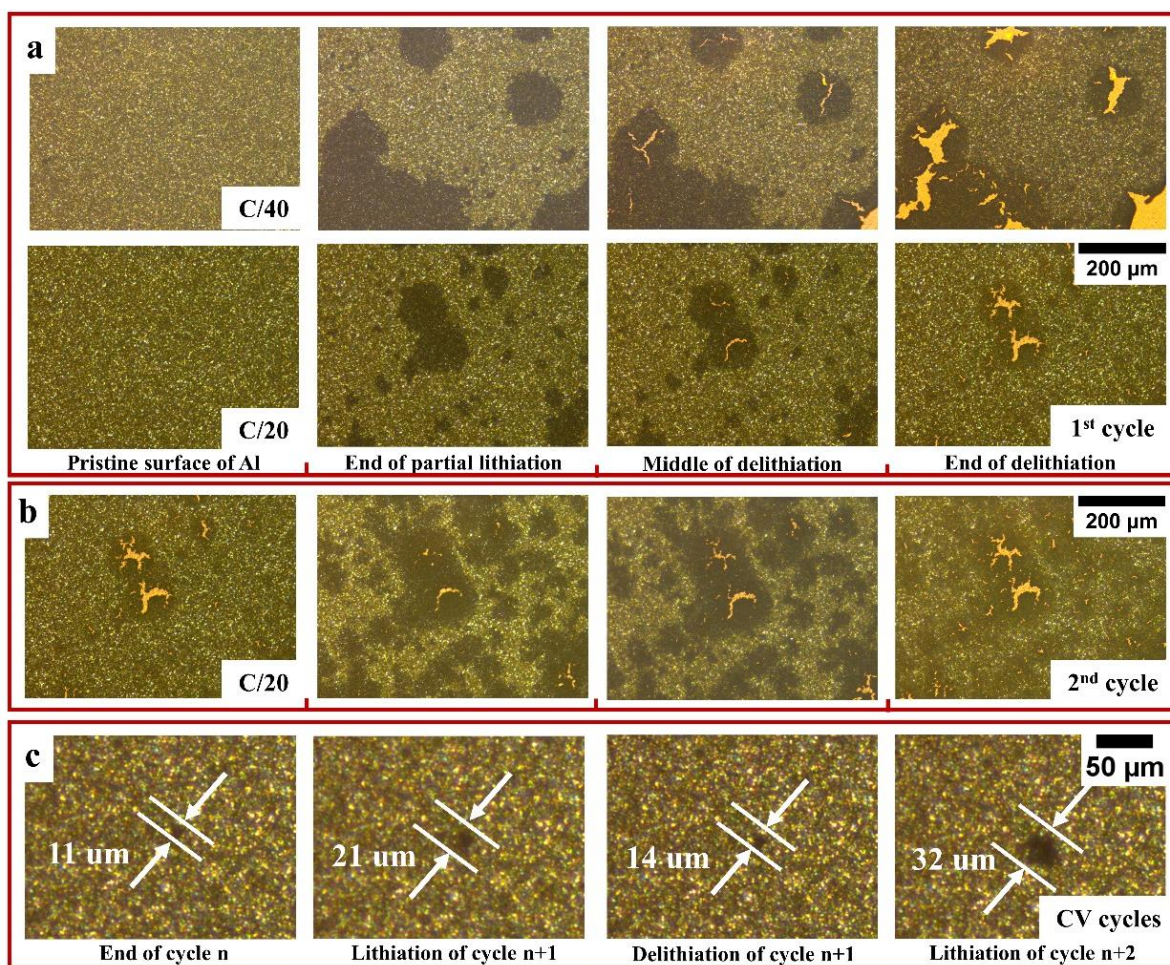


Figure 5.2. *Operando* light microscopic images of the sputtered Al thin film surface taken for (a) the initial galvanostatic cycle at two rates, for (b) the second cycle at C/20, and for (c) a randomly picked  $\beta$  phase patch during CV at  $0.5 \text{ mV s}^{-1}$ , including (1) initial state taken at 1.5 V vs.  $\text{Li/Li}^+$  after certain cycles when the nucleus appears; (2) after lithiation at 0.1 V vs.  $\text{Li/Li}^+$ ; (3) after delithiation; and (4) after the subsequent lithiation. The complete *operando* videos can be found in the Supporting Information online from [96].

To explore samples at a higher resolution, SEM images are also collected for partially lithiated Al thin films, in addition to the light microscopy ones. The surface morphology is revealed by Figure 5.3a while the corresponding backscattered image (Figure 5.3b) gives a clear indication of the  $\beta$  phase distribution due to the lower electron density in the lithiated  $\beta$  phase. As can be seen, the patches are generally island-like with creases that are likely caused

by the volume expansion during lithiation. SEM images of the Al film after delithiation in Figure 5.3c-d show cracks within the delithiated patches due to the volume contraction as Li leaves the LiAl alloy and the delamination. Under higher magnification at a granular level, an elongation of the grains is observed in Figure 5.3e-f after lithiation. After delithiation, on the other hand, no clear grain structure can be found under the same magnification (Figure 5.3g).

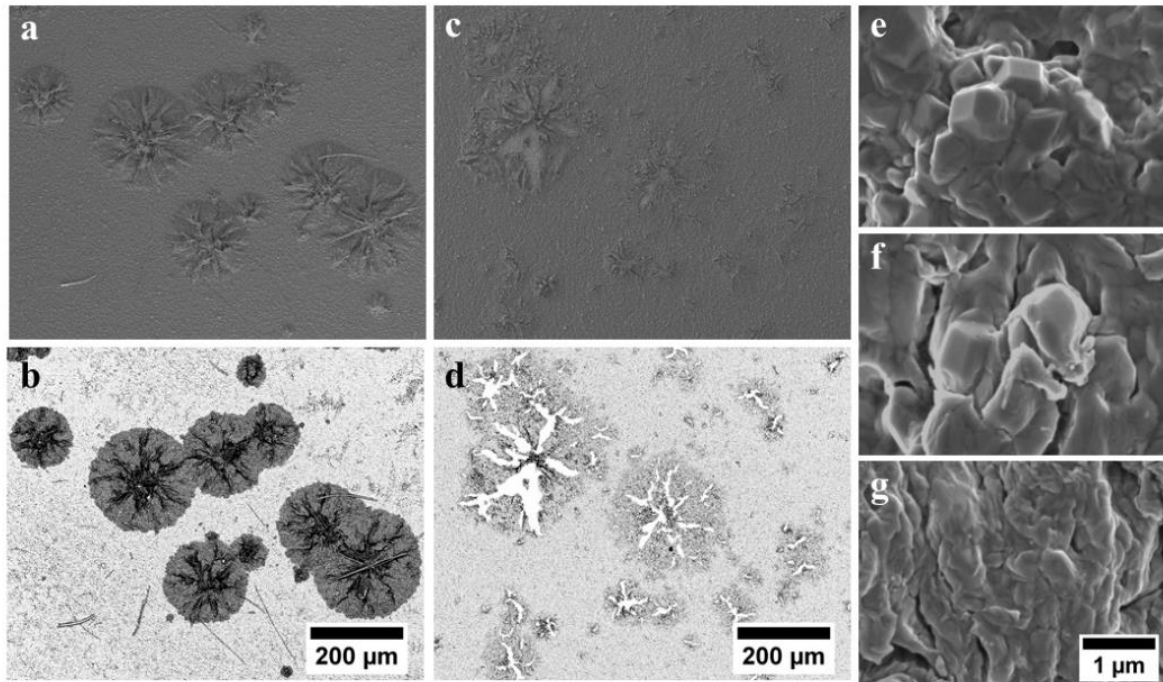


Figure 5.3. SEM images taken from (a, b) a partially lithiated and (c, d) a delithiated Al thin film. (b, d) images taken by a back-scattered electron (BSE) detector where the dark circular patches in (b) denote the lithiated  $\beta$  phase LiAl. High magnification SEM images revealing the grain morphology of (e) the pristine, (f) the lithiated and (g) the delithiated Al thin film.

With the help of *operando* light microscopy and SEM, the delithiation and re-lithiation processes can be illustrated as shown in Figure 4. The (de-)lithiation processes during electrochemical cycling can be summarized:

1. **Initial lithiation:** This process was elaborated in our previous study,[50] including oxides lithiation, nucleation, and growth of the  $\beta$  phase (Figure 5.4a-c). The important features such as random nucleation and quasi-circular growth generally remain under the GCD mode.

However, it should be noted that a constant current gives various growth rates for each  $\beta$  phase patch while a constant potential yields a similar rate. The growth mechanism is suggested to be controlled by the reaction at the phase front for both cases.

2. **First delithiation:** This includes the formation of cracks within the  $\beta$  phase patches when the delithiation process occurs (Figure 5.4c-d). Afterward, the patches continue to contract, causing larger cracks associated with delamination along the edge until the delithiation is completed (Figure 5.4e). Smaller patches may experience less severe degradation because the localized stress can be absorbed by the elastic strain of the surrounding Al matrix.[79] It should be mentioned that the shrinkage, cracking and delamination observed for the thin film on a substrate might be less relevant for bulk Al foils.

3. **Second lithiation:** The re-growth of the  $\beta$  phase initiated at the position where the patches were located previously. This behavior means that the nucleation is easier within the newly formed structure after dealloying compared to the pristine bulk Al. The cracks become smaller after the second lithiation, and progressive nucleation occurs to form new  $\beta$  phase patches. Since the current efficiency during delithiation is below 100%, e.g., because of delamination which will prevent the delithiation of disconnected  $\beta$  phase, it is clear that a second lithiation with the same charge will result in larger and/or more  $\beta$  phase patches (Figure 5.4f). The subsequent cycles should be similar as described here by eliminating the influence of the SEI formation that is only pronounced during the initial lithiation. Nevertheless, this ongoing growth of the  $\beta$  phase would not occur in a full cell, where typically the total amount of Li is limited by the cathode composition

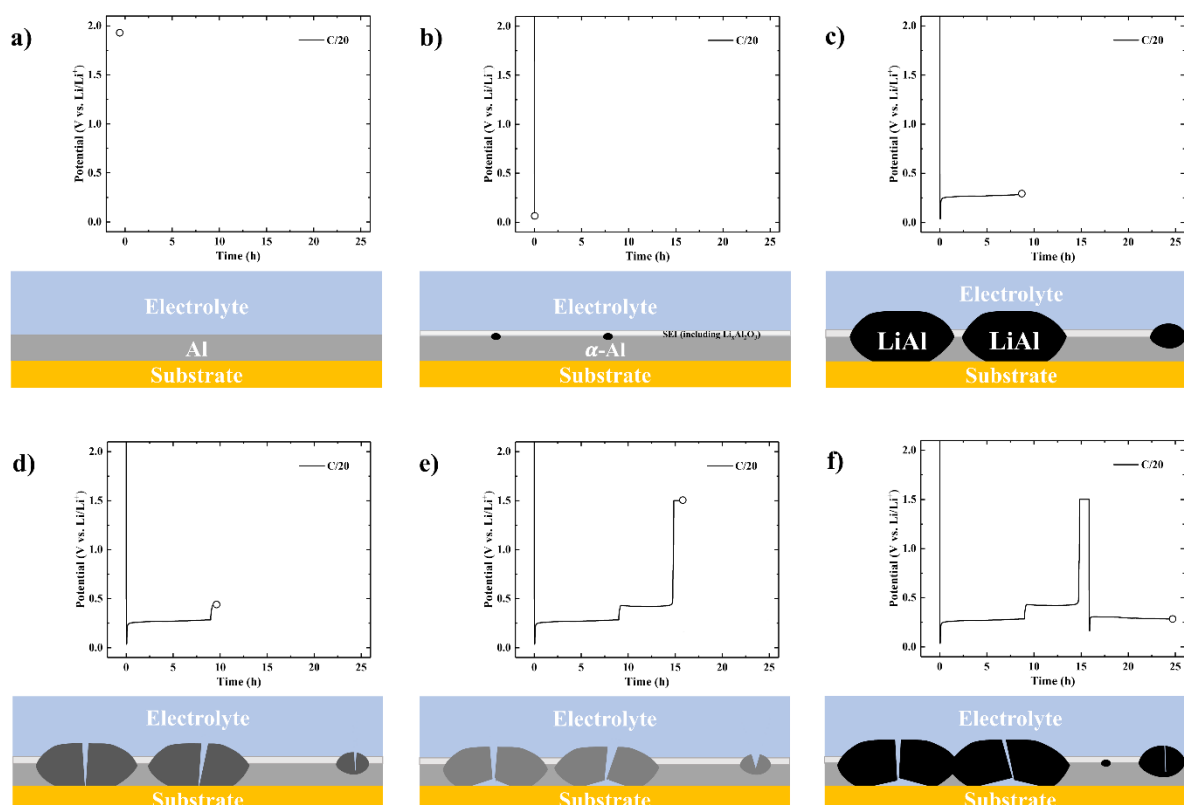


Figure 5.4. Schematic illustrations of Al thin film anodes during electrochemical (de-)lithiation: (a) Pristine Al electrode (i.e., before initial lithiation); (b) nucleation of the  $\beta$  phase; (c) end of first partial lithiation; (d) middle of the first delithiation; (e) end of first delithiation and (f) end of the second lithiation. It should be noted that the cyclic SEI forms within the  $\beta$  phase patches and is not elaborated here.

## 5.2.2 *In situ* stress measurement

In a substrate-based thin film model system where a rigid interface exists, the volume expansion caused by Li insertion strains the substrate and results in compressive stresses in the  $\beta$  phase. As illustrated by the *operando* videos, there is a sharp interface between  $\alpha$  and  $\beta$  phase, which suggests that there are considerable local stresses at this interface. Since the ductile Al metal under tension is presumably not as strong as the neighboring  $\beta$  phase under compression, it is expected that the metallic  $\alpha$  phase close to the perimeter of the  $\beta$  phase patches will plastically yield. This involves the creation and motion of dislocations and the

release of the tensile stress in the  $\alpha$  phase which in turn will lower the compressive stress in the  $\beta$  phase nearby. During delithiation, mechanical energy can be dissipated by cracks to some extent, and a previous study suggests that mechanical stress/strain should play a crucial role in the lithiation process of Al.[19] Clearly, volume changes and associated mechanics are of importance governing the two-direction phase transformations. For instance, Li et al. suggest that the performance of alloy anodes can be considerably improved by guiding the volumetric strains into selected directions.[13] In order to assess the mechanical aspects of this electrode material, we employ substrate curvature measurements to collect relevant mechanical information.

As can be seen from Figure 5.5a, continuous build-ups of compressive stresses are observed during lithiation processes, even though the magnitude shrinks with an increasing number of cycles due to electrode degradation. Interestingly, the almost linear evolution of stress during lithiation does not occur in some other alloy anodes, such as Si[97] and Ge[20, 98], which exhibit two regimes: quasi-elastic straining and quasi-plastic deformation with quite constant stresses. The continuous stress evolution in this work is expected to be a result of the linear change of the phase fractions of  $\alpha$  and  $\beta$ . This agrees with the *operando* observations where the  $\beta$  phase patches grow at a constant rate. It should be noted that a larger slope of the stress vs. capacity curve is observed when the lithiation plateau potential is no longer preserved (i.e., last ~20% of lithiation; indicated by the blue arrow), implying that there might be different mechanisms besides the two phase coexistence at the end of lithiation. Here, further investigations are needed for clarification.

The delithiation process of the Al thin film exhibits a completely different behavior compared to the lithiation. The nominal stress moves quickly towards tension from  $\sim -540$  MPa back to  $\sim -100$  MPa after reversing the current direction and then flattens out when the potential hits the delithiation plateau. Only a small amount of Li extraction causes this significant tensile

stress rise at the beginning of delithiation.

The physical reason for the pronounced asymmetry of the stress curve is related to the large overvoltage that is needed to move the  $\alpha/\beta$  interface: During ongoing lithiation, the  $\beta$  phase must be Li-rich, with respect to its Li solubility, to enable the  $\alpha$  to  $\beta$  conversion. During delithiation, the reverse phase transition also dissipates mechanical energy in addition to Li extraction, causing a corresponding overvoltage. Meanwhile, Li content in the  $\beta$  phase must approach its minimum to trigger the phase transition. Correspondingly, Li released from the solubility range of the  $\beta$  phase is separated from the phase transition, resulting in two distinct features in the stress signal: a large stress change caused by the solubility range and a constant stress profile by the  $\beta$  to  $\alpha$  phase transition. All the features are also observed in subsequent cycles, except that the stress magnitude becomes smaller due to the cyclic electrode degradation.

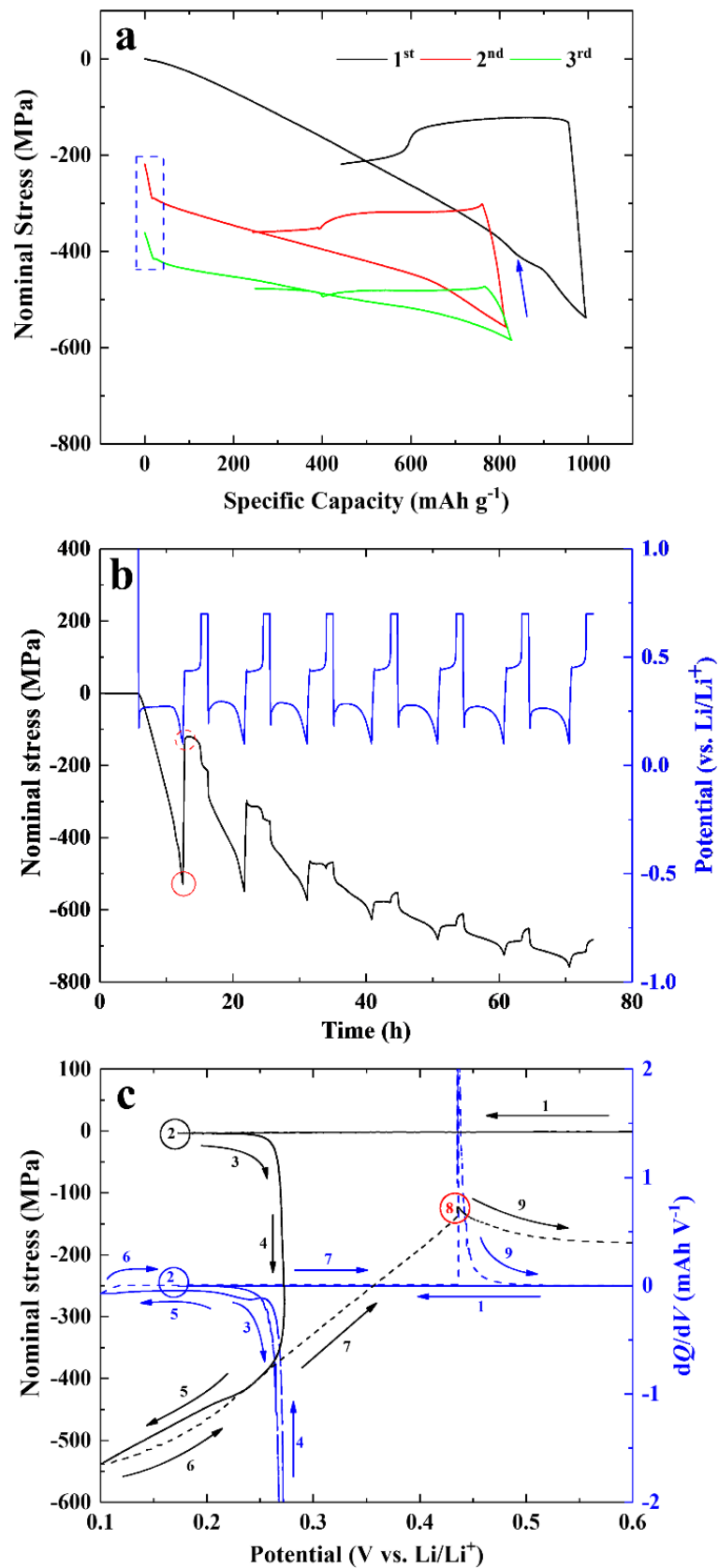


Figure 5.5. (a) Nominal stress as a function of specific capacity: data of the first three cycles are plotted: black (1<sup>st</sup>), red (2<sup>nd</sup>) and blue (3<sup>rd</sup> cycle). (b) The maximum (end of lithiation) and

the minimum compressive stress (end of delithiation) are extracted and plotted against cycle number. (c) Incremental capacity analysis (ICA): nominal stress (black line) and differential capacity (blue lines: solid-lithiation and dashed-delithiation) as a function of potential vs.  $\text{Li/Li}^+$  under galvanostatic cycling conditions between 0.1 V and 0.7 V for the initial cycle. The steps are numbered to link the stress and the  $dQ/dV$  curve.

Apart from the stress analysis of individual cycles, one can notice that there is a stress build-up over cycling, i.e., the stress does not revert to its initial level and grows continuously despite fluctuations stemming from individual cycles. As shown in Figure 5.5b, the compressive stress generated after the seven lithiation is increased by ~47% compared to the first one (i.e., ~70<sup>th</sup> hour vs. ~12<sup>th</sup> hour). This continuous build-up of stress can be partly supported by the observations of Qin et al., which show that the thickness of Al constantly increases during cycling.[59] This incomplete reversibility of the electrode thickness may contribute to the accumulation of compressive stress for our substrate-based system. The other interesting feature here is that the stress difference between the maximum and the minimum of the first cycle is ~-400 MPa (i.e., difference between the dashed and solid red circles), which becomes less evident and eventually levels off by the fourth cycle. Together with the sharp increase of compressive stress at the beginning of the second and the third cycle (Figure 5.5a; blue dashed rectangle), it is suggested that the delithiated Al matrix should have different structures and mechanical properties compared to the unlithiated/pristine one. Such a new delithiated Al structure should completely replace the pristine Al film after three full cycles. This assumption will be evaluated later together with the SEM observations.

A complementary approach of analyzing data known as incremental capacity analysis (ICA) is used to help understand the stress evolution during lithiation and delithiation. Figure 5.5c shows the ICA of cycle 1, where the nominal stress and the differential capacity are plotted versus potential. Such plots overlay and compare the volumetric (stress/capacity) and the

surface/interface property (potential), thereby yielding extra insights in addition to the stress-capacity curves. In general, most of the features discussed above can also be found in the ICA plot, such as nucleation (blue circle; step 2) and lithiation plateau (steps 3 and 4; detailed discussion in Appendix III: Supporting Information of Chapter 5). Importantly, there is a mismatch between the stress and the  $dQ/dV$  signal in the lower potential regime (steps 5 and 6): the compressive stress increases from roughly  $-400$  MPa to  $-550$  MPa while the net amount of charge is nearly zero. In the Li-Al system, only the  $\beta$  phase is thought to be present at room temperature, especially considering that the cut-off voltage here is set at  $0.1$  V, above which  $\text{Li}_{1+x}\text{Al}$  phases should not be expected.[99] However, the existence of amorphous  $\text{Li}_{1+x}\text{Al}$  phases is suggested by a previous Al anode study,[59] and thus warrants further investigation.

Assuming that the  $\beta$  phase is the only phase present in this case, the total volume of the film is expected to shrink during the delithiation as the Li extraction proceeds, resulting in the motion towards tensile stress. As can be seen from Figure 5.5c, the tensile stress grows almost linearly against potential until the potential increases to the delithiation plateau at  $\sim 0.45$  V and then flattens out. This process is equivalent to the sudden stress rise at a high state of charge (SOC) in the stress-capacity curve shown in Figure 5.5a. Then a stress peak is observed at the same potential as the delithiated peak of the  $dQ/dV$  curve is located (red circle; step 8), which may refer to the nucleation of the  $\alpha$  phase once the Li content within the  $\beta$  phase approaches a minimum. This feature indicates that Li solubility plays a primary role in generating sharp stress rise because the film mostly still consists of the  $\beta$  phase at this point. The  $\beta$  phase has a Li diffusivity that is several orders of magnitude higher than that of the  $\alpha$  phase and a Li solubility of several percent. Once the Li concentration varies within this solubility range, the  $\beta$  phase may change its overall volume and shift the lattice parameter (e.g., by  $\sim 0.03$  angstrom),[45] thus generating substantial stresses. When the  $\beta$  to  $\alpha$  phase transition starts, the stress change would only occur close to the phase interface that is moving through the volume.

In other words, the stress change contributed by this tiny active volume where the atomic rearrangements are happening should be limited.[45] Additionally, this stress profile may also be attributed to the brittleness of the  $\beta$  phase to a minor extent,[38] coinciding with the *operando* light microscopy which visualizes the crack formation process. The local tensile stress that is produced during delithiation should be partly released while the cracks form and grow within the  $\beta$  phase patches, where delamination is observed at the edges. The dynamic processes are shown in the videos that can be found in the online version of [96].

Together, both Li solubility and crack formation can help to explain why the stress profile does not vary significantly during the subsequent delithiation, even though Li is continuously extracted. Interestingly, slight compressive stress is generated towards the end stage of Li extraction again, which can be explained by the incomplete volume expansion/contraction, e.g., formation of nanopores, which will be elaborated together with the SEM images later. It should also be noted that the ICA analysis of the subsequent cycle follows similar trends as the initial cycle (Figure S5.4; detailed discussion in Appendix III: Supporting Information of Chapter 5).

To answer the lingering issues arising from the *in situ* stress analysis, SEM images are taken for the pristine and the cycled ( $\times 10$ ) cantilever to reveal the change of surface morphology and film thickness. As illustrated in Figure 5.6a, the as-deposited Al film is generally flat, and Al grains ( $\sim 2 \mu\text{m}$ ) are visible. An image was taken using an Everhart-Thornley Detector which is mounted on the side of the sample and gives some height information in the image due to shadowing of lower regions. It is shown in Figure 5.6b and indicates that the flat surface no longer preserves after cycling. Instead, the cycled film exhibits a completely different morphology from a flat thin film to a loose and porous structure. The cross-sectional view in Figure 5.6c mainly shows the  $\sim 250 \mu\text{m}$  thick alumina substrate while the pristine Al film is hardly visible at a magnification of  $500\times$ . The initial film thickness is

revealed and characterized to be ~420 nm under the higher magnification of Figure 5.6e. As visualized by Figure 5.6d, the film extraordinarily expanded after 10 cycles. The cycled Al film is estimated to have a thickness of ~20  $\mu\text{m}$ , indicating an expansion by a factor of more than 40, significantly beyond the theoretical ~100% volume expansion.[26] The porosity of the cycled Al film is linked to the expansion and can be estimated to be approximately 98%. A large porosity is also evident in the high magnification SEM image Figure 6f. The material exhibits the typical bicontinuous nanostructure obtained by dealloying, i.e. the selective dissolution of an element from an alloy which is also considered a common process to fabricate nanoporous metals.[100, 101]. A single dealloying step might give a porosity similar to the fraction of the less noble metal (e.g., 76% porosity for the dealloying of  $\text{Ag}_{80}\text{Au}_{20}$ ,[102] but the large porosity here is the result of 10 alloying/dealloying cycles. The most identical characteristic, the Al ligament diameter of ca. ~36 nm observed here, generally fits the relationship with the homologous temperature plot presented in the previous study.[103] Reasonably, these ligaments will become elongated once Li is inserted. For delithiation, on the other hand, the ligaments do not have to become significantly shorter because Al atoms need to be rearranged anyway. This argument agrees with Figure 5.5b, which indicates that the stress difference after lithiation and delithiation stopped changing after three cycles due to the ligament formation. Also, it explains why the contraction is originally observed by light microscopy during the initial delithiation, and this contraction should hardly occur after the third cycle once the film is completely replaced by Al ligaments. Lastly, the associated film thickness increase and structural change are of vital importance to understand the stress behavior over cycling. The stress accumulation, i.e. the increase of the absolute value of the compressive stress with the number of cycles, shown in Figure 5b can be well elucidated by this thickness increase.

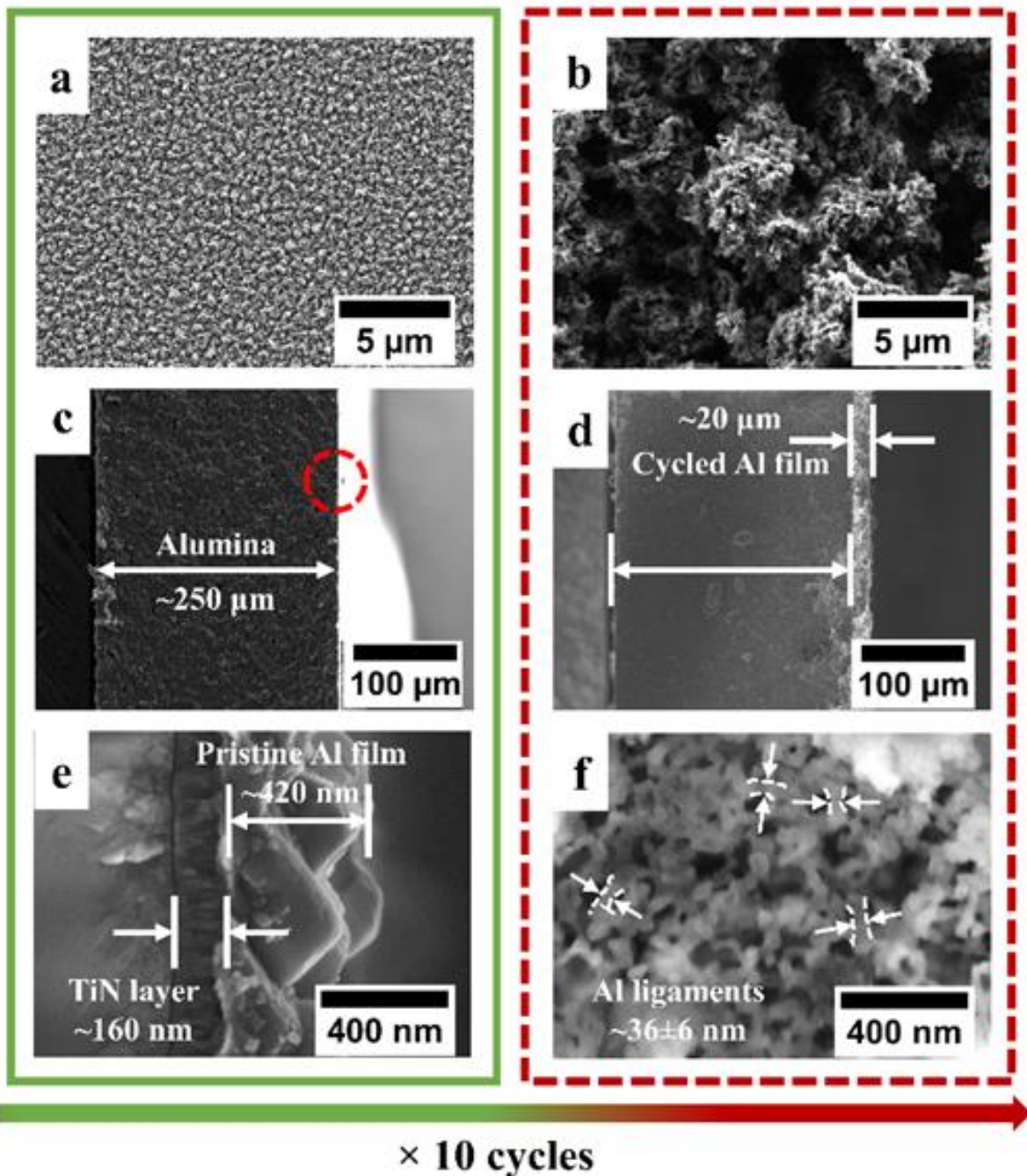


Figure 5.6. SEM images taken from the Al thin film electrodes before and after cycling: (a), (b) surface morphology taken by a detector for secondary electrons (SE) that is sensitive in probing the height difference; (c), (d) cross-sectional views reveal that the volume expansion of the Al film after 10 cycles is way beyond 100%; (e) enlarged cross-section of pristine Al film (red dashed circle in (c)) with a thickness of  $\sim 420$  nm and (f) enlarged top view of the cycled Al film that exhibits nanoporous features. More SEM images showing the surface morphology are provided in Figure S5.5.

At this point, the prioritized lithiation at existing patches observed in the *operando* videos can be well explained by this highly porous Al matrix after delithiation. Such a porous structure, which allows for volume expansion and stress relaxation, seems to facilitate nucleation of the  $\beta$  phase. In comparison, the formation of new patches in pristine Al should require a higher overvoltage. Furthermore, the external volume can remain quite constant during dealloying due to the formation of pores. This constant external volume can result in a flattened stress profile during delithiation. Therefore, the lack of tensile stress in our case is probably due to the formation of nanopores rather than crack formation, while a combination of both effects is still possible due to the brittleness of the  $\beta$  phase. Importantly, our findings may allow us to revisit some of the previous studies, explaining why the nanoporosity has hardly been reported. An example could be the in situ TEM study for Al nanowires done by Liu et al. who describe that voids are formed continuously during each delithiation until the nanowire electrode is entirely pulverized into isolated particles (i.e. a bamboo structure).[33] However, the nanowires used in their study have a diameter of  $\sim 40$  nm (similar to the size of the ligament diameter shown in Figure 5.5f), which is still too small to exhibit porosity, even when the thickness of SEI is considered. In other words, the nanoporous structure observed in our study cannot be reproduced by such experimental conditions, suggesting that Al nanowires might not be fully representative of the practical situation for Al electrodes in LIBs.

The formation of the nanoporous structure is also relevant for the discussion of the degradation mechanisms proposed in the literature. It has been suggested that Li might get trapped in the electrode by an enclosure of  $\beta$  phase with a dense layer of  $\alpha$  phase which hinders the transport of Li.[34] The highly porous structure shown in Figure 5.6f has such a large area of the electrode/electrolyte interface that it seems unlikely that a relevant fraction  $\beta$  phase can remain completely enclosed by  $\alpha$  phase.

After analyzing the *operando* light microscopic observations and the *in situ* stress measurement separately, relevant insights of Al films as anode material in LIB have been collected. The next step is to evaluate whether the outcome so far agrees with both sets of data. Therefore, a new stress cell is assembled to undergo the galvanostatic tests with ~45% partial (de-)lithiation cycling as same as the optical cells did. After the initial cycle at 0.1 C, the lithiation rate is fixed at 0.1 C and coupled with the various delithiation rates in the sequence of 2 C, 1 C, 0.5 C, 0.2 C, and 0.1 C to further investigate the delithiation process. As plotted in Figure 5.7a, the linear increase of compressive stress is also observed for the partial lithiation. It is obvious that the compressive stress amplifies over cycling, once zero stress is defined at the beginning of each cycle. As the *operando* videos show that the second lithiation always initiates at the existing patches that expand further, the larger patches and the additional nucleation during the second cycle (i.e. more Al is lithiated) most likely contributes to the higher stress, explaining this stress amplification over cycles. As for the delithiation, it follows the same trend as the full lithiation where a small amount of charge causes huge tensile stress, regardless of the C rate. After that, the stress stays constant towards the end of delithiation. To have a better understanding, the slopes of stress versus charge during individual cycles for the lithiation and delithiation are extracted and shown in Figure 5.7b. It can be clearly seen that the stress per charge data during lithiation appears to have a quite linear regime, indicating that in later cycles, less charge is needed to reach the same level of compressive stress. This agrees with the *operando* observation of the larger patches plus the formation of new patches and with the SEM images of the film thickening behavior over cycling. On the other hand, the slopes for delithiation all exhibit similar stress per charge values under various C rates. This implies that the Li diffusion within the  $\beta$  phase is facile (i.e. high Li diffusivity) and that crack formation behaves similarly at all rates (i.e. inevitable crack formation).

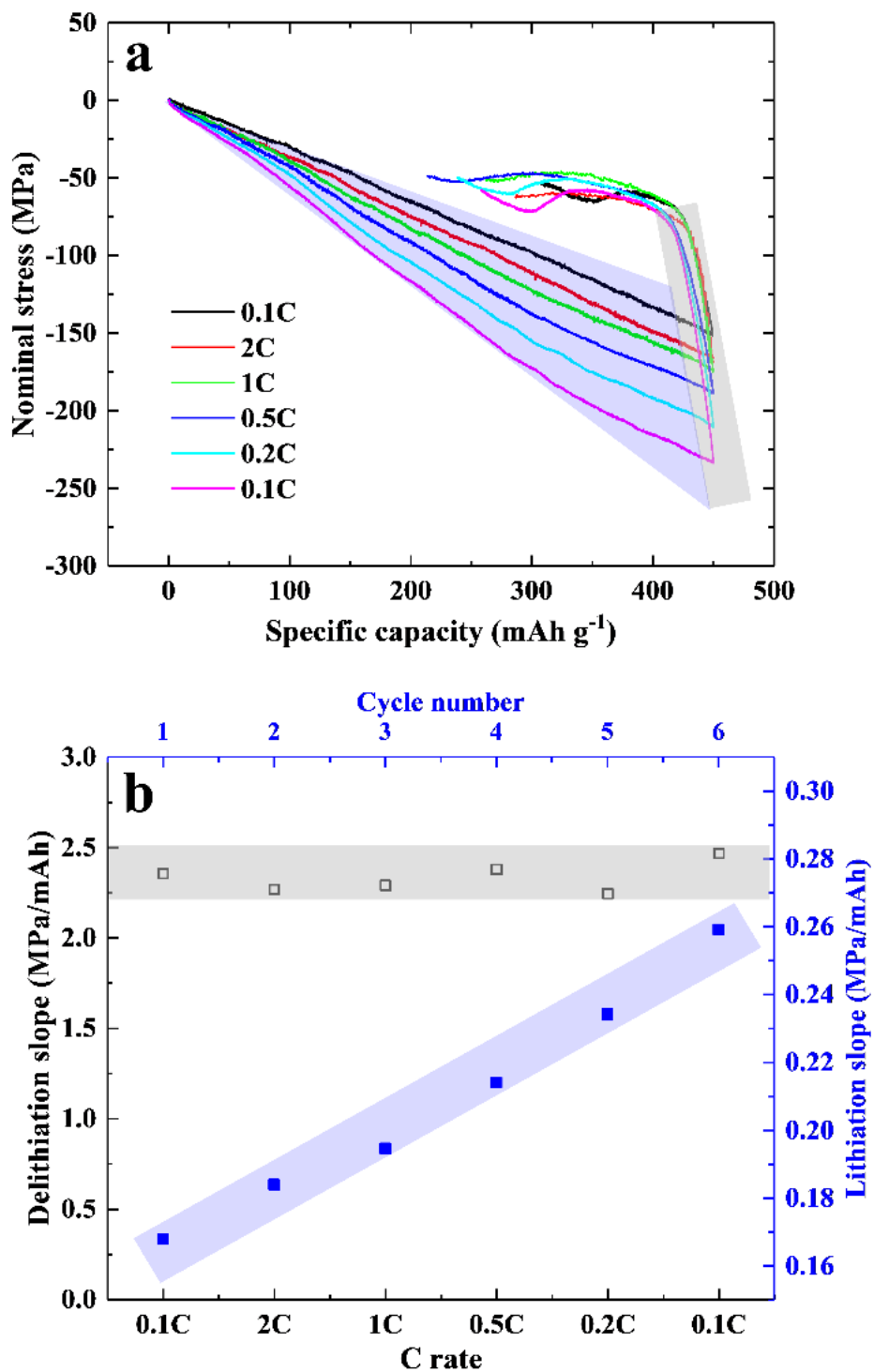


Figure 5.7. (a) Nominal stress versus specific capacity during a partial lithiation for an Al thin film, with fixed lithiation rate at 0.1 C and various delithiation rates ranged from 0.1 C to 2 C; the stress level of each individual cycle is normalized to be zero for easier comparisons. (b) Slopes describing force over charge, extracted from the shadow region (delithiation) and the linear stress accumulation (lithiation) in (a).

In agreement with previous studies, the outcomes discussed so far suggest that Al may have significant intrinsic challenges when employed as an anode material in future LIBs. Our previous study concludes that through minimizing the coalescence between the  $\beta$  phase patches observed in the *operando* videos, the surrounding  $\alpha$  phase can greatly stabilize the electrode due to its higher ductility that reduces the mechanical stress from the volume expansion by plastic deformation. In this study, with the help of *in situ* stress measurements, some other crucial factors that may also significantly affect the cycling performance of Al anodes are also realized:

a. Mechanical effect 1, lithiation: compressive stress builds up continuously versus electric charge during the GCD test. One may manipulate the speed of the mechanical stress evolution by varying the current density once the SEI is stable after a couple of cycles with partial lithiation. The reaction-controlled growth of the  $\beta$  phase patches suggested by the previous kinetic study can further support this argument.[50]

b. Mechanical effect 2, delithiation: the compressive stress developed during lithiation is released by removing a small amount of Li from the  $\beta$  phase. Perhaps most of this stress release happens with neither the nucleation of  $\alpha$  phase nor a significant movement of the  $\alpha/\beta$  interface. Instead, Li is extracted from the  $\beta$  phase by changing its composition within the solubility range. Later when there is little compressive stress, cracks form in the delaminated parts and are inevitable even though the delithiation rate is as low as C/40. Although the crack formation is most likely a result of the brittleness of the  $\beta$  phase, it should be mentioned that metals that are highly ductile in their ordinary state, like gold, can behave brittle on the macroscopic scale if they are nanoporous and exposed to tensile stresses.[104, 105] Hence, even the nanoporous Al alloy ( $\alpha$  phase  $\text{Li}_x\text{Al}$  with  $x < 10\%$ ) might be more susceptible to cracking compared to pure Al which can be very ductile.

Figure S5.6 presents the cycling performance of coin cells, which seems to be only

affected by lithiation rates (detailed discussion in Appendix III: Supporting Information of Chapter 5). Upon understanding the structural change of Al anodes over cycling, one may presume that the significantly higher surface area of such a porous (i.e. cycled) Al can be more compliant than a solid (i.e. pristine) Al. In other words, lithiation of the porous Al, including secondary SEI formation, might initiate everywhere, referring to the sharp increase of compressive stress at the beginning of the second and the third cycle shown in Figure 5.5b. Meanwhile, the pristine Al electrode only must be lithiated from the surface. Therefore, the lithiation rates should not matter that much if most solid Al has been converted to a porous one. To prove that, gentle (de-)lithiation rates at C/20 are considered as the formation cycle before applying fast (dis-)charging conditions. As shown in Figure 5.8, two formation cycles are sufficient to achieve similar cycling performance as the one with C/20 partial (de-)lithiation in Figure S6a. These findings support that the Al anode can tolerate some high rate cycling, such as fast charging if formation cycles have been run prior to further usage.

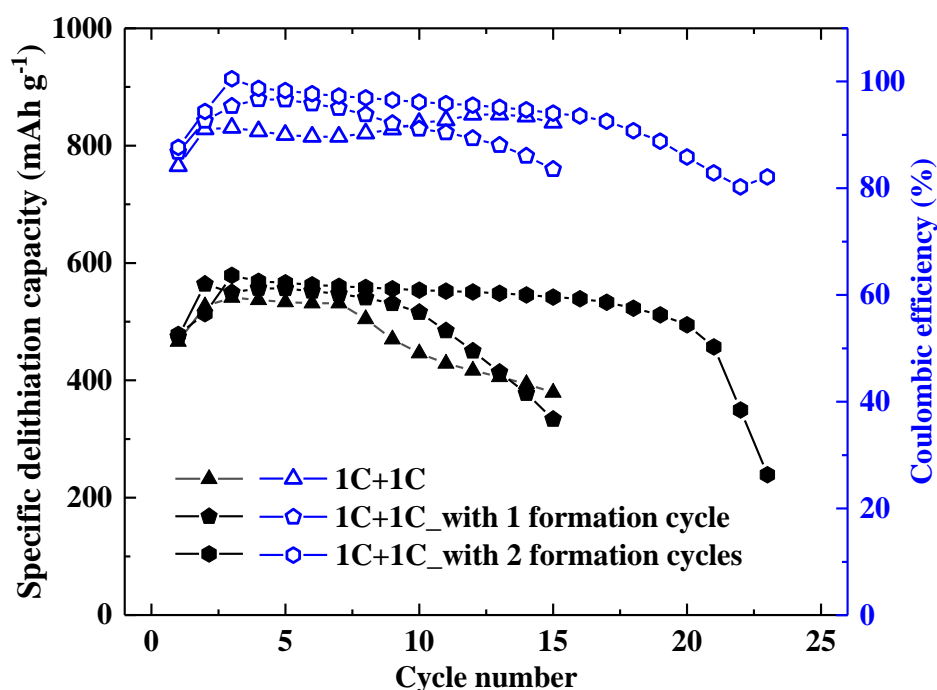


Figure 5.8. Coin cell performance of Al thin film anodes under a half-cell configuration that reveals the influence of the number of slow formation cycles on the cycle life. The whole sets

of cycling data and corresponding discussion can be found in Appendix III: Supporting Information of Chapter 5.

### 5.3. Conclusion

The electrochemical cycling of Al thin film electrodes has been explored by SEM observations, *operando* light microscopy and *in situ* stress measurements with a focus on the initial delithiation and on the subsequent cycles. The *operando* videos obtained visualize the noticeable degradation, such as cracks and delamination of Al thin film anodes during the first delithiation. The second lithiation initiates at the delithiated patches. Additional  $\beta$  phase patches are nucleated, and the volume that is or has been converted to  $\beta$  phase increases from cycle to cycle due to the limited coulombic efficiency. The alleviated lithiation at the existing patches was also observed in a CV scan, with a partial expansion/contraction of the patches. Based on the *operando* light microscopy, a schematic model has been built to illustrate the (de-)lithiation processes of Al thin film anodes. Moreover, *in situ* stress measurements and SEM can yield extra insights: (1) continuous buildup of compressive stress during lithiation; (2) rapid tensile stress evolution after reversing the current direction; (3) nearly constant stress during the main part of the delithiation. The sudden tensile stress rise can be attributed to the Li solubility range of the  $\beta$  phase, and the constant stress part can be attributed to nanoporosity and crack formation. Lastly, we examine the impact of mechanical effects on the stability of Al anodes using conventional coin cells with Li metal as the counter electrode. The cycling data show that a slower lithiation rate during the first cycle results in a longer cycling life due to improved or modified nanoscale structures of the film. The degradation does not seem to be rate-dependent during delithiation, owing to the inevitable formation of nanoporosity and cracks revealed by light and electron microscopy. Although this study contains information regarding fundamental processes, the utilization of the Al/LiAl/Al ( $\alpha/\beta/\alpha$ ) phase

transformations might be challenging due to the intrinsic volume changes and the related mechanical issues that affect not only the thin film electrodes used here, but also are expected to influence conventional electrode designs with Al particles. As a result, future LIBs using Al-based anodes will require a strategic mitigation of the complication associated with the phase transformations. The investigations have laid the foundation for a series of follow-up studies, such as SEI engineering, protective layers/coatings, and development of micro-/nano-structures, which can presumably mitigate the shortcomings presented above, thus helping improve the performance of Al -based anodes.

## 6. (De-)lithiation mechanisms of bulk foils

As mentioned at the beginning of this thesis, the final goal is to enable the usage of bulk Al foils as anodes for LIBs. Polycrystalline Al alloy products can be easily found in daily life, such as food packaging, window frame, and vehicle components. The matureness of Al alloy industry significantly reduces the cost and the complexity of its manufacturing processes. Upon a comprehensive understanding of the electrode/electrolyte interface using the substrate-based model (i.e., Al thin films), our next step is to evaluate the performance and to investigate the underlying mechanisms of bulk Al foils, by highlighting the similarities and differences as compared with Al thin films.

### 6.1. Background

Conventional composite anodes consist of active materials, polymer binders, and conductive additives. These components are dissolved into a solvent, usually N-Methyl-2-Pyrrolidone (NMP) and are well mixed to form a “slurry”, which is then be pasted onto a piece of copper foil for drying. Not only does the toxicity of NMP threaten occupational safety and environmental friendliness, but also the multi-step nature of the electrode manufacturing may result in unnecessary costs of labor and capital. The most crucial distinction of Al foils is that a novel structure can be developed by a partial lithiation, such that the top ( $\beta$ -LiAl) and the bottom (fcc-Al) layer function as the active material and the current collector, respectively. This novel anode design significantly simplifies the electrode manufacturing and deducts the fabrication cost by omitting the usage of copper foil and other additives, thus offering us a great opportunity to completely change the current state-of-the-art anodes.

Boles and Tahmasebi stated clearly in their commentary paper that the volumetric capacity of a dense foil would be significantly higher than that of a conventional particle-based electrode design.[106] Moreover, a paper published in Science highlights the volumetric

capacity should play a more important role than the gravitational one in various EES devices and applications. An example would be that a low-density graphene electrode only exhibits a similar level of volumetric energy as conventional EES products, although extraordinarily high gravitational energy has been reported scientifically. [107] As a result, considering the simplified manufacturing and the mass production capability, recent interest in anode development for LIBs has been slowly shifted towards bulkier and denser forms, such as foils, meshes, and other possible electrode structures. Importantly, the great thickness and the strong polycrystallinity of Al foils may offer us excellent opportunities in investigating the cross-section using SEM and collecting the structural information using XRD, respectively.

## 6.2. Results and Discussion

In the Li-Al solid solution, there exist multiple phases as described in the phase diagram depending on the Li content, such as  $\beta$ -LiAl,  $\text{Li}_3\text{Al}_2$ , and  $\text{Li}_9\text{Al}_4$ . [43] Although vast majority of the studies focus on the  $\beta$ -LiAl that is predominant at room temperature, Li-rich phases are never elaborated and consistent conclusions can hardly be achieved. For instance, Ghavidel et al. report that the  $\text{Li}_3\text{Al}_2$  and the  $\text{Li}_9\text{Al}_4$  are only approachable at the temperature higher than  $35^\circ\text{C}$  and  $100^\circ\text{C}$ , respectively. [99] On the contrary, Li-rich phases (i.e. higher Li contents than the  $\beta$ -LiAl) are also detected at room temperature by some other research. [29, 35] Recently, Qin et al. conducted an in situ XRD study for Al composite anodes and claim that amorphous Li-rich phases ( $\text{LiAl}_{1+x}$ ) are formed at the end of lithiation where the potential plateau no longer remains. [59] Another interesting explanation is that the Li-rich phases are probably present on the electrode surface, though the overall equilibrium is fcc-Al/ $\beta$ -LiAl. [95]

### 6.2.1 *Operando* XRD for (de-)lithiation cycles

The *operando* x-ray diffractograms have been obtained for the first two galvanostatic

cycles of the Al foil electrode. Figure 6.1 presents the diffractograms in conjunction with GCD curves. To start with, there is a slight shift in  $2\theta$  angle at the beginning of lithiation, coinciding with the discussion regarding the initial nucleation of the  $\beta$ -LiAl in one study.[32] The authors claim that the local distortion caused by the local mechanical deformation may slightly shift the lattice parameter of fcc-Al. Both  $\langle 111 \rangle$  and  $\langle 220 \rangle$  peaks of the  $\beta$ -LiAl appear after lithiating the Al foil for around 4 hours. Since then, it is quite normal that the intensities of both peaks grow stronger and stronger until the end of lithiation due to the  $\beta$  phase accumulation. On the contrary, fcc-Al peak slowly blurs out at  $\sim 8^{\text{th}}$  hour and eventually disappears at  $\sim 15^{\text{th}}$  hour, agreeing with the progressive decrease in the grain size of fcc-Al described in Figure 6.4.[35] It should be noted that disappearance of the Al peak may refer to extremely small grain size or even amorphization. Another crucial feature of the diffractograms is that the  $\langle 111 \rangle$  LiAl peak disappeared when the lithiation plateau of the GCD curve no longer exists (i.e., end of lithiation) while the  $\langle 220 \rangle$  LiAl peak does remain but with a shifted  $2\theta$  angle. This shift is likely a result of the Li solubility because the saturation of the  $\beta$  phase may change its overall volume and shift the lattice parameter by  $\sim 0.03 \text{ \AA}$ . [45]

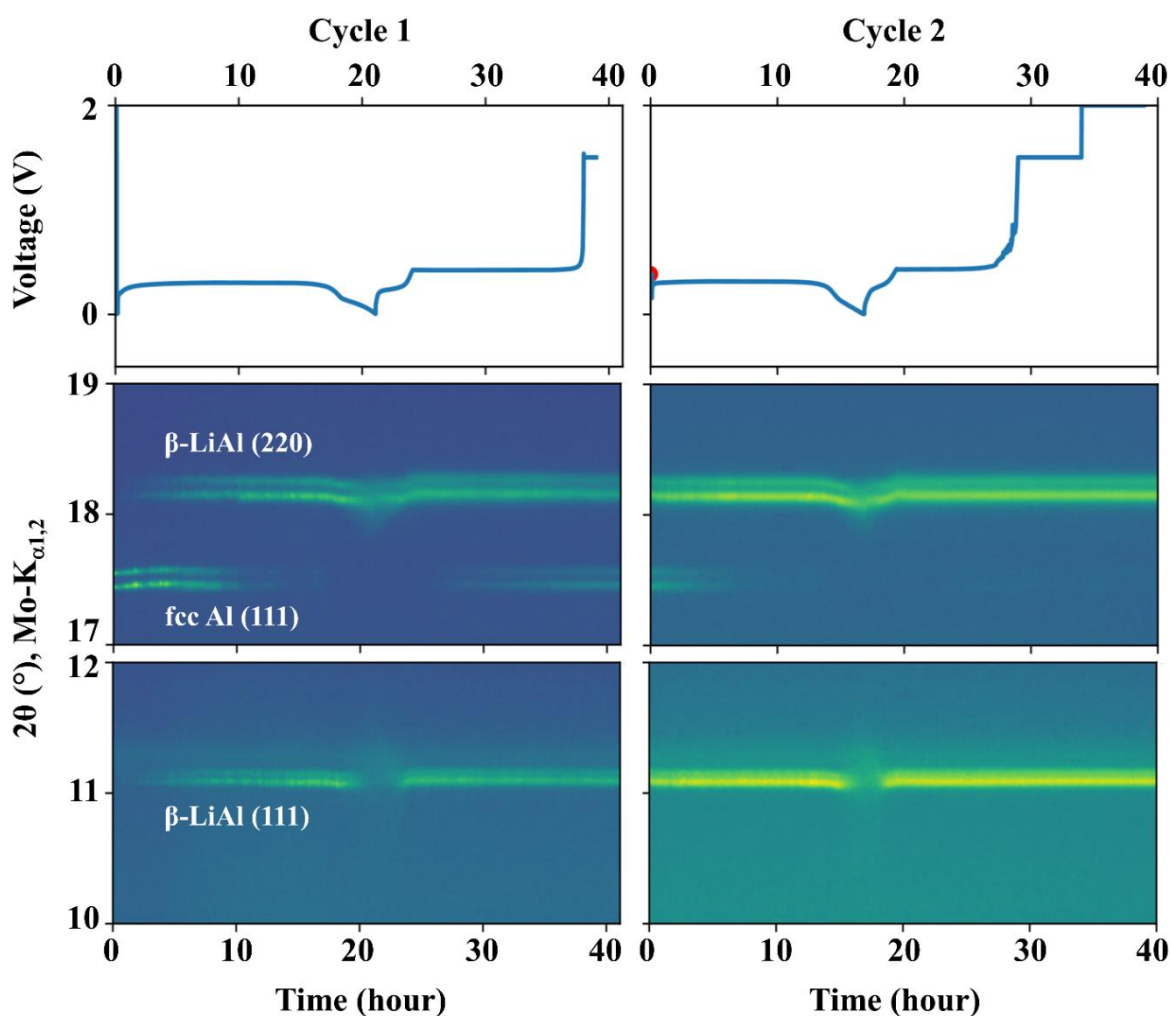


Figure 6.1. Waterfall plot of the *operando* XRD for the Al foil in conjunction with the galvanostatic profile of the first and the second cycle obtained at a rate of C/20.

Qin et al. have also observed and elaborated this decrease towards disappearance of the peak intensity for  $\langle 111 \rangle$  LiAl using *in situ* XRD. They claim that amorphous Li-rich ( $\text{Li}_{1+x}\text{Al}$ ) phases are forming at the consumption of the  $\beta$ -LiAl at end of lithiation, explaining why there is no crystalline peak for these Li-rich phases in the diffractograms.[59] Nonetheless, it is believed that solely tracking the peak intensity might not be fully representative. In a diffractogram, peak intensity indicates the degree of crystallinity while the peak area represents the amount of a certain crystalline plane. Therefore, the peak area of  $\langle 111 \rangle$  LiAl is integrated from the diffractograms and plotted against time during the lithiation and delithiation. As

shown in Figure 6.2, it can be clearly seen that the amount of  $\langle 111 \rangle$  LiAl keeps increasing during the whole lithiation process, though the peak intensity drops at the end of lithiation. This observation partly agrees with the theory of the progressive decrease of the grain size. At the end of lithiation, fcc-Al is mostly converted into the  $\beta$ -LiAl with a roughly doubled volume and thus is under higher compression. This mechanical force induces lots of dislocations in the remaining fcc-Al, resulting in extremely small grain size or even amorphization.

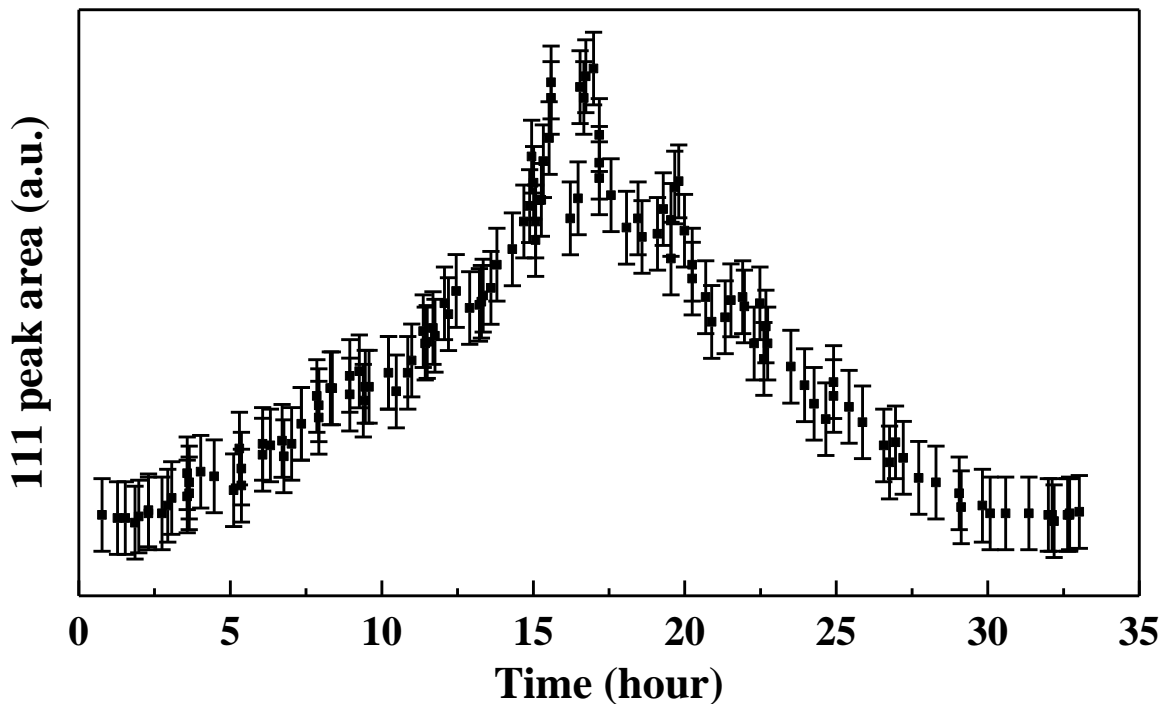


Figure 6.2. The area integrated from the  $\langle 111 \rangle$  peaks of the diffractograms as a function of time during a lithiation-delithiation cycle.

Back to Figure 6.1, the shifted  $2\theta$  angle of  $\langle 220 \rangle$  LiAl caused by the Li solubility and the disappeared  $\langle 111 \rangle$  LiAl peak restore when the potential approaches delithiation plateau. Most likely, this potential increase is caused by the desaturation of the  $\beta$ -LiAl and nucleation of the  $\alpha$  phase. The  $\langle 111 \rangle$  peak of fcc-Al re-appears by delithiating for roughly 5 hours, but with a significantly lower intensity, indicating a significantly smaller grain size. This weak crystallinity of  $\langle 111 \rangle$  Al disappears again during the second lithiation and can never be

detected since then, suggesting that the delithiated Al becomes amorphous and/or nanocrystalline after two cycles.

As illustrated, the  $\beta$ -LiAl peaks are still outstanding at the end of delithiation, implying that Li-trapping probably occurs. This trapping issue cannot be resolved by holding the potential at a level as high as 2 V (Figure 6.1). As already elaborated in Chapter 5 of this thesis, the Li trapping is suggested to occur on the basis of “dead Li”, such that a certain amount of  $\beta$ -LiAl may fall off from the electrode and become non-conductive electrically due to its mechanical brittleness and volume expansion.[96] It should be re-emphasized that the  $\beta$  phase encapsulation described by Oltean et al. is not observed.[34]

## 6.2.2 Initial nucleation of the $\beta$ phase

Since the nucleation occurs at the interface between the electrode and the electrolyte, a foil electrode is expected to behave similarly to a film electrode. The obtained SEM images can perfectly support the hypothesis. Figure 6.3a shows the surface view of a slightly lithiated Al foil, of which the random distribution of the  $\beta$  phase nuclei can be observed. As judged by the variety of the  $\beta$  phase patch sizes, progressive nucleation probably also occurs. The same technique using a BSE detector is used to identify the phases at the cross-section. Interestingly, it can be seen in Figure 6.3b-c that the  $\beta$  phase patch has a saucer shape and exhibits a loose structure consisting of noticeable voids while the fcc-Al nearby is still dense and stable. This saucer shape implies that the  $\beta$  phase growth exhibits different propagation rates horizontally and vertically. Through measuring multiple samples, the horizontal propagation rate is estimated to be  $\sim 3.5 \pm 0.6$  times faster than the vertical one. Once the patches become sufficiently large and coalesce with each other, 1D in-depth propagation of the  $\beta$ -LiAl should be expected.

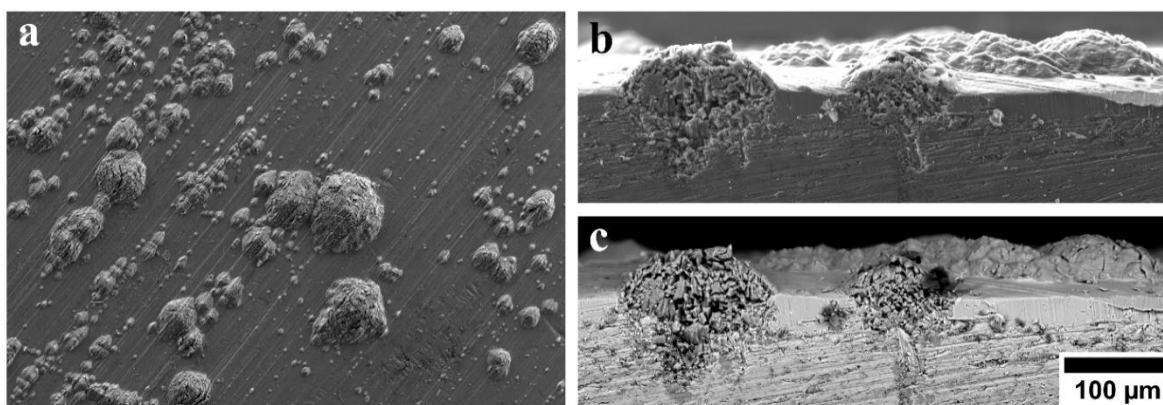


Figure 6.3. (a) An SEM image showing the surface view of a slightly lithiated Al foil; images taken at the cross-section of using (b) a SE detector and (c) a BSE detector at the same location.

An *operando* XRD test that collects the structural information of the Al foil simultaneously as the phase transformations are ongoing can be ideal in understanding this new  $\beta$  phase structure. The initial nucleation is elaborated together with the illustrations in Figure 6.4. The pristine 38  $\mu\text{m}$  thick Al foil is found to have a grain size in the order of 100  $\mu\text{m}$ . The 2D XRD image in Figure 6.4a clearly shows the evolution of Bragg reflections of individual Al  $\langle 111 \rangle$  grains. Once the foil starts being lithiated, the nuclei shall appear at the electrode/electrolyte interface since the Li ions can hardly diffuse within fcc-Al, presumably at grain boundaries (Figure 6.4b).[40, 50, 81] As the lithiation goes, the formation of  $\beta$ -LiAl leads to large mechanical stresses that push the neighboring fcc-Al grains, eventually causing localized plastic deformation (i.e. dislocations) in the Al foil electrode. This interesting behavior is evidenced by the 2D XRD images in Figure 6.4c-d, of which the Bragg reflections show a continuous pattern, indicating smaller Al  $\langle 111 \rangle$  grains. Due to this mechanical deformation induced by the nearly 100% volume difference between the two phases, fcc-Al grains turn into quite small grains before being lithiated and transformed into the  $\beta$ -LiAl.

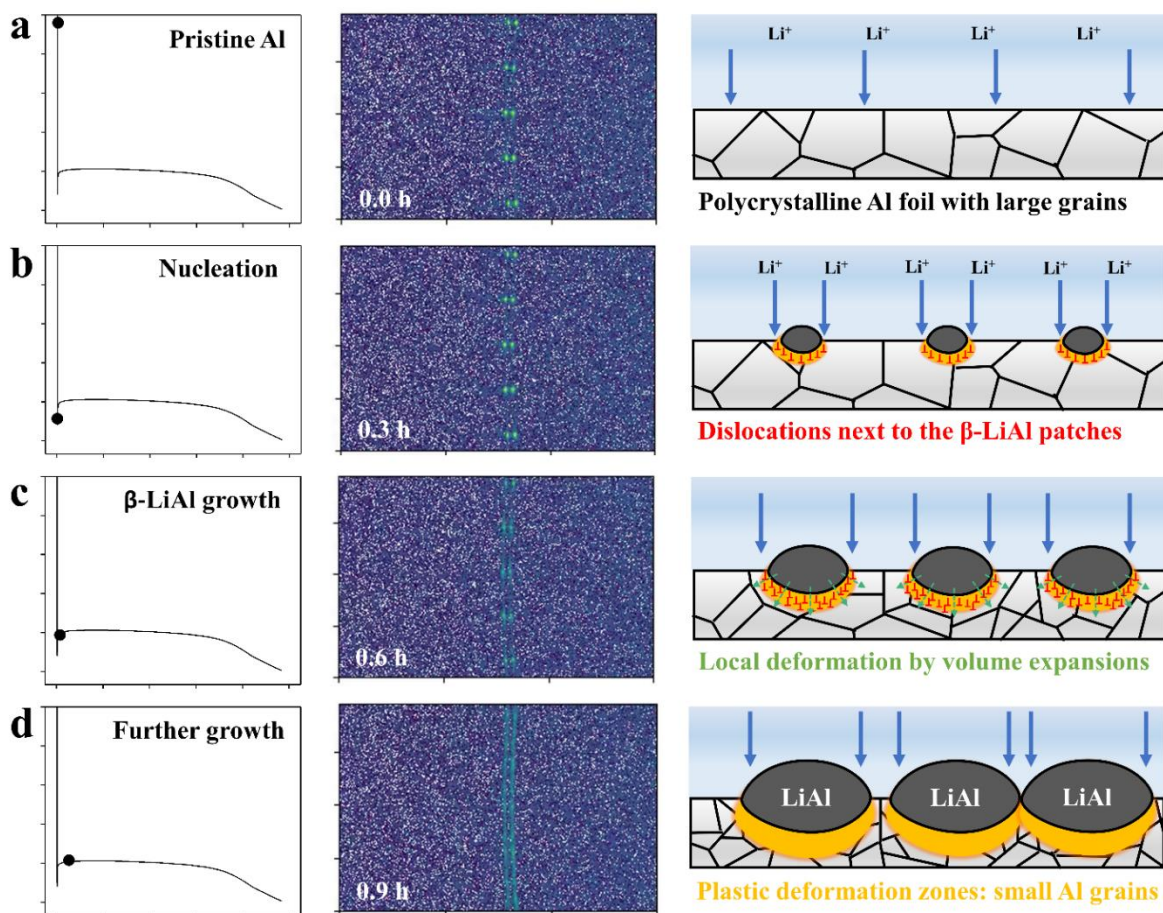


Figure 6.4. From left to right: the galvanostatic profile (black dot), the 2D image of XRD detector, and the schematic illustrations of (a) Pristine Al foil electrode, (b) right after nucleation, (c) expansion of initial nuclei, and (d) further growth of the  $\beta$  phase.

### 6.2.3 Initial propagation of the $\beta$ phase

This in-depth growth behavior is not pronounced for thin films but can be of vital importance in bulk Al foils, of which the thickness is not trivial. The same cross-sectional SEM is employed to explore how the  $\beta$ -LiAl propagates through the z-axis, especially that the electrode/electrolyte interface of Al foils is found to behave similarly as Al thin films. Figure 6.5a captures the surface as well as the cross-sectional morphology of a partly lithiated Al foil ( $\sim 7.5\%$  lithiation) by tilting the SEM sample holder by  $45^\circ$ . As expected, the full coverage of the  $\beta$  phase on the electrode surface is likely a result of coalescences as the isolated saucer-

shape patches in Figure 6.3 grow. Correspondingly, a continuous layer of the  $\beta$  phase is observed in the cross-section, such that further lithiation can only occur in a quasi-1D manner along the z-axis. By taking a closer look at the place of interest (i.e., the cross-section) at higher magnification (Figure 6.5b), one can notice that there exist hairy regions (highlighted by red arrows) within the lithiated regions at the cross-section, which exhibit the same color tone under the BSE detector as the unlithiated fcc-Al. Subsequently, the dark ( $\beta$ -LiAl), the bright (fcc-Al), and the hairy region are characterized by an EBSD detector. The obtained diffraction patterns in Figure 6.5c-d prove that the bright hair has the same crystal structure as fcc-Al, and it is not lithiated presumably due to a huge compression.[81] Since the surface and the cross-sectional view exhibit different morphologies, the XRD test with a low incident angle has been done to collect the structural information on the electrode surface. The diffractogram in Figure 6.5e elucidates that the  $\beta$ -LiAl is the only crystalline phase after this partial lithiation of an Al foil except for the inevitable oxides lithiation and SEI formation. The XRD suggests that the different morphology of the electrode surface is likely caused by the native oxide layer lithiation and SEI formation, which are not expected at the cross-section.

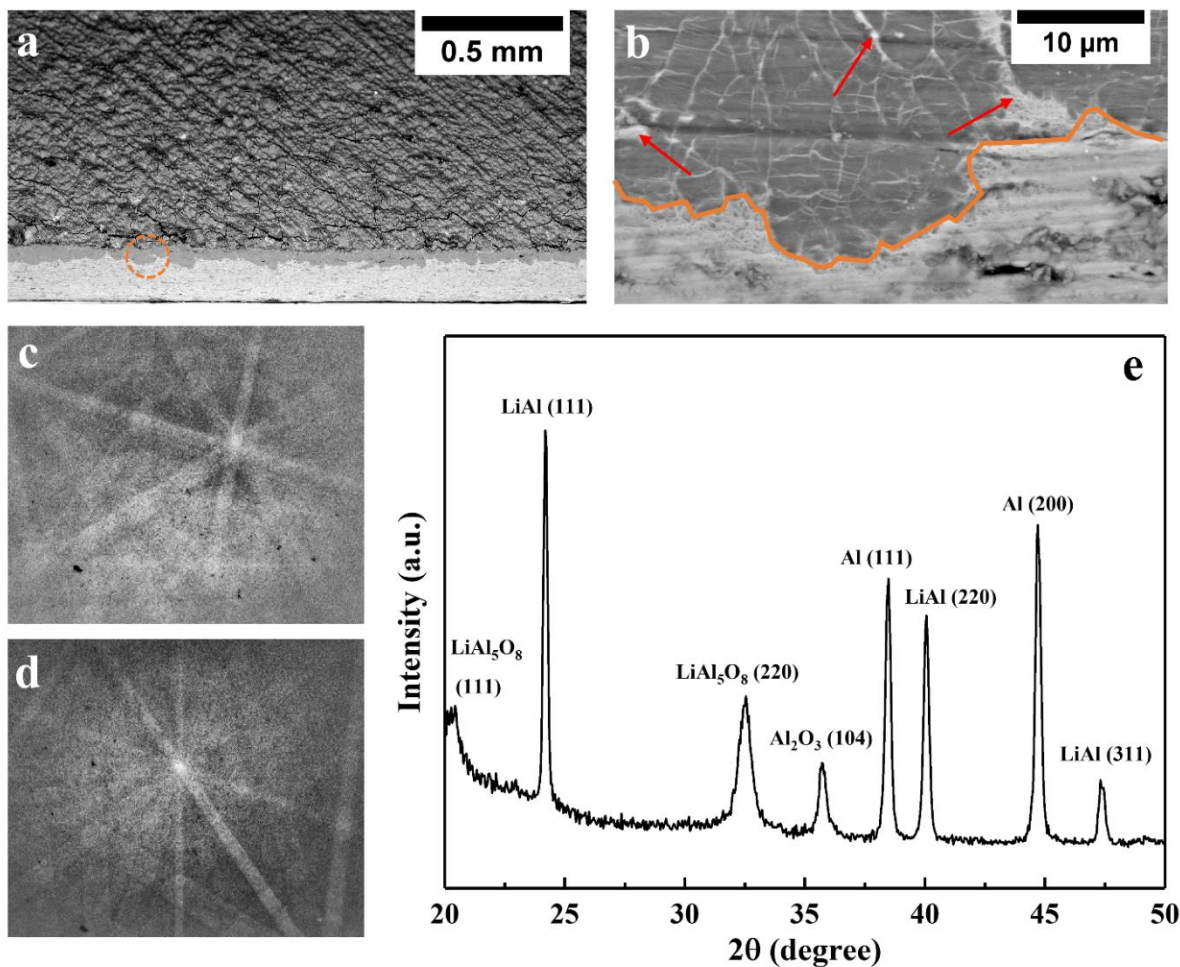


Figure 6.5. SEM images taken for a partially lithiated Al foil using a  $90^\circ$  sample holder (a) with a tilting angle of  $45^\circ$ , (b) the enlarged image at the cross-section. The EBSD pattern obtained at (c) the white region (fcc-Al) and (d) the dark region ( $\beta$ -LiAl) of (b). (e) XRD diffractogram with an incident angle of  $1^\circ$ , such that only the surface structural information is revealed.

The hairy region should be emphasized here as no study has ever reported such an observation. Based on the phase transformation theory for metals and alloys, certain mechanical work must be overcome to nucleate the Al foil electrode.[91] An extreme case should exist where fcc-Al at specific positions get pushed by the neighboring  $\beta$ -LiAl, and thereby under extraordinary compression. This amount of mechanical stress may prevent the compressed fcc-Al from being nucleated due to a significantly higher energy barrier, resulting in these observed hairy regions.

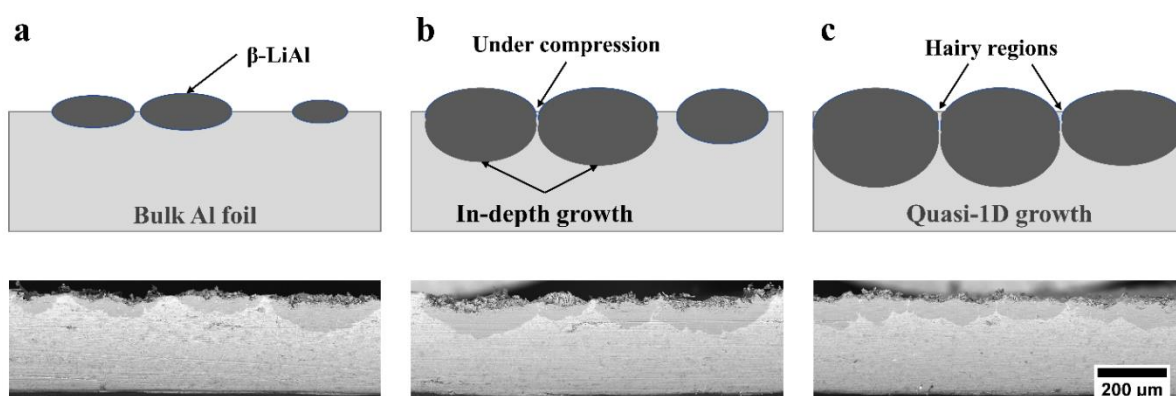


Figure 6.6. Schematic illustration in conjunction with the SEM images taken using a BSE detector: (a) nucleation and growth of the  $\beta$ -LiAl prior to coalescences, (b) the  $\beta$ -LiAl patches coalesces with each other, facilitating in-depth growth, (c) hairy regions of fcc-Al exists when the surface of the Al foil electrode is fully covered with the  $\beta$ -LiAl, after which only in-depth growth is allowed.

The whole process of the hairy region formation is schematically demonstrated and coupled with SEM images at the cross-section of a partly lithiated Al foil. Figure 6.6a displays that the  $\beta$ -LiAl nuclei grow and saucer-shape patches. Although the  $\beta$ -LiAl above the surface no longer exists due to its brittleness and the grinding process in the corresponding SEM image, the semi-circular shape of  $\beta$ -LiAl is clearly observed at the in-depth profile. As the patches grow larger and larger, they would eventually merge and form a semi-continuous matrix. However, the fcc-Al between the two patches is under considerable compression due to the volume expansion of the  $\beta$  phase (Figure 6.6b). As a result, this part of fcc-Al can hardly be nucleated due to the elevated energy barrier caused by mechanical compression. Instead, the further growth of the  $\beta$ -LiAl must develop via the z-axis (in-depth). When the surface of the Al foil electrode is completely covered with the  $\beta$ -LiAl, as illustrated in Figure 6.6c, this amount of fcc-Al forms lots of hair that exhibits contrast against  $\beta$ -LiAl under the BSE detector.

## 6.2.4 Initial delithiation of the $\beta$ phase

As the cross-sectional SEM is found to be quite ideal to be an experimental tool in probing the phase transformations of Al foil electrodes, the same procedure has been performed on a partly cycled Al foil. i.e., a partial lithiation and a full delithiation until 1.5 V vs. Li/Li<sup>+</sup>. Figure 6.7a shows that the electrode surface becomes catastrophic after delithiation. It is believed that the electrode/electrolyte interface of Al foil anodes behave similarly as Al thin film anodes, which have already been elaborated in Chapters 3, 4, and 5. It is rather surprising that the contrast between the two phases still present as evidenced by the generally flat interface in the cross-sectional SEM image (Figure 6.7b), although the electrode is delithiated and presumably no/little  $\beta$  phase exists. This contrast is an indication of a high porosity of the delithiated matrix because a similar color under a detector for backscattered electrons (BSE) represents the similar atomic mass. In other words, the  $\beta$ -LiAl formed after lithiation does not shrink significantly during delithiation, causing a uniform distribution of the nanopores inside the delithiation Al matrix. Consequently, the mean atomic mass of the matrix becomes similar to the  $\beta$  phase and exhibits similar contrast under the BSE detector.

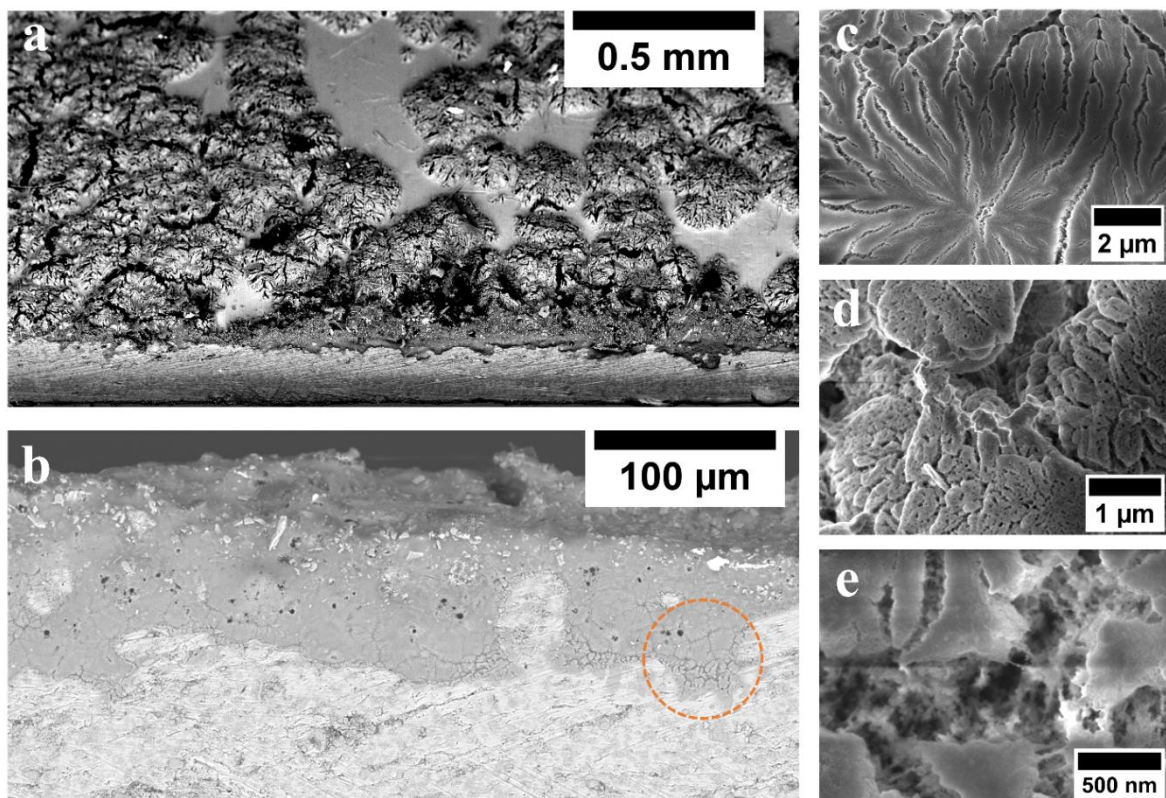


Figure 6.7. SEM images taken for a partially cycled Al foil (~7.5% lithiation depth) using a 90° sample holder (a) with a tilting angle of 45°, and (b) at the cross-section. (c) The high magnification SEM images obtained within the dashed orange circle in (b), revealing the structure of the delithiated Al matrix.

Under a higher magnification in Figure 6.7c, an interesting flower-like pattern is observed and is considered as a result of the grinding process for achieving a high-quality cross-section. Through further increasing the magnification, pores become visible on top of as well as beneath (Figure 6.7d) the flower-like pattern. It should be noted that it was challenging when taking the high magnification SEM image shown in Figure 6.7e due to a lack of electron transfer. Such a porous structure usually comes with a huge surface area that facilitates the cyclic SEI formation. The ligaments shown in Figure 6.7e may be covered with a thin layer of SEI, and thus resulting in poor electrical conductivity.

### 6.2.5 Repetitive cycling of Al foil electrodes

Then another Al foil is partly cycled against Li repetitively. Surprisingly, different from the partial lithiated Al foil shown in Figure 6.8a, the cycled one in Figure 6.8b clearly illustrates that the phase interface at the cross-section becomes perfectly flat after 10 (de-)lithiations. The uneven stress distribution at the interface facilitates the Li atoms to preferentially lithiate the fcc-Al that is under relatively small compression during the second lithiation.[81] After trimming for several times ( $\times 10$  cycles in this case), the obtained flat interface can be well explained. It should be noted that the cycled matrix can easily fall off from the fcc-Al foil underneath due to the porosity and brittleness (Figure 6.8b).[96] We also would like to note that a cyclic SEI formation is captured in Figure 6.8c-d, where two SEM detectors are used to explore the same position. Figure 6.8c was taken by a surface-sensitive in-lens detector while a SE detector used for Figure 6.8d is appropriate to reveal height differences. The former gives a larger cluster size than the latter, implying that some surface reactions are occurring, i.e. cyclic SEI formation. It becomes more evident by overlapping these two images (Figure 6.8a and b). Moreover, the evidence of nanoporous Al after cycling is provided in Figure 6.8e which exhibits the typical feature that is consistent with other nanoporous metals produced by selective dealloying.[103] This nanoporosity results in an extremely high surface area that reasonably facilitates the cyclic SEI formation.

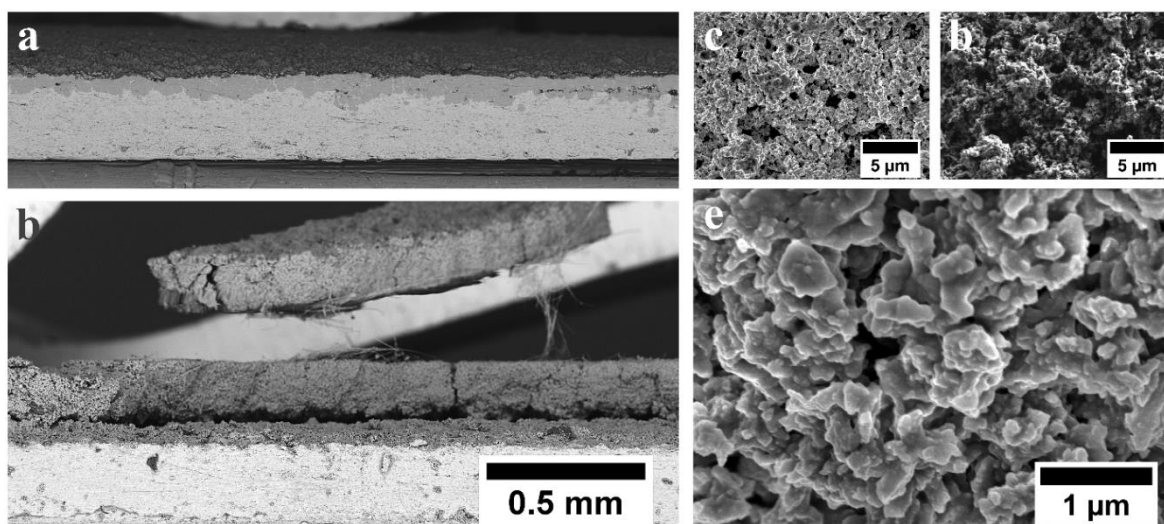


Figure 6.8. SEM images taken at the cross-section for (a) a partially lithiated and (b) a partially cycled ( $\times 10$  cycles) Al foil. The electrode morphology was evaluated under (c) a surface-sensitive and (d) a depth-sensitive detector. (e) The newly formed nanostructure of this Al foil after 10 partial cycles.

The obtained SEM image series offers direct proof of electrode morphology, thus yielding a comprehensive understanding of how Al foil electrodes evolve during electrochemical cycling. The overall processes are schematically illustrated in Figure 6.9. The volume of the Al foil electrode expands after the initial partial lithiation to form a layer of  $\beta$ -LiAl (Figure 6.9a-b). The volume does not contract significantly after the first delithiation, developing a porous structure (Figure 6.9c).[96] As the pores do not play a role in chemical reactions, only the newly formed ligaments get lithiated and elongated during the subsequent lithiations, eventually causing an extraordinary volume expansion upon cycling. Moreover, new cycles may engage slightly more fcc-Al due to the loss of material shown in Figure 6.8b. It should be noted that the subsequent lithiations develop a flat phase interface due to the mechanical effect (Figure 6.8d): the hairy regions in Figure 6.6 of the delithiated Al foil are not under the same compression as those of the lithiated state, and thus can be lithiated during the second cycle with a priority. After the second delithiation, the volume expansion with a factor of  $\sim 4$  is

expected due to a higher density of nanopores (Figure 6.8e). Reasonably, the third lithiation further increases the overall volume by solely lithiating the Al ligaments (Figure 6.8f). This volume increase upon cycling can be found from the SEM images in Figure 6.8a-b and can cause a more than 40 times volume expansion after 10 cycles.[96]

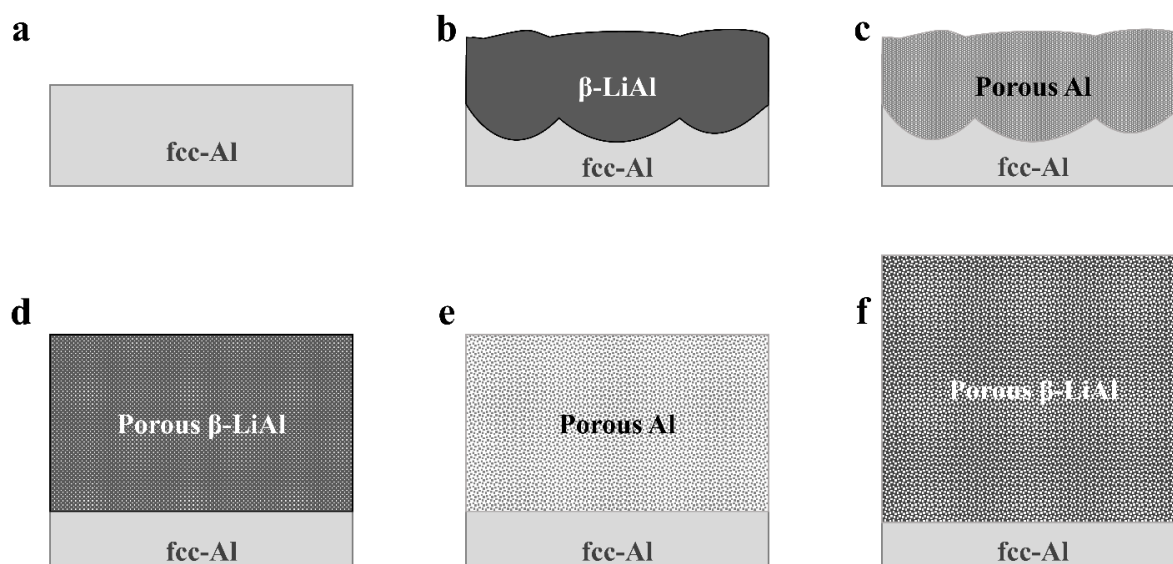


Figure 6.9. Schematic illustrations of the Al electrode during repetitive cycling: (a) pristine fcc-Al foil, (b) after initial lithiation, (c) after the first delithiation, (d) after the second lithiation, (e) after the second delithiation, and (f) after the third lithiation. The subsequent cycles will follow the same trend here.

### 6.3. Summary

Generally, the phase transformations of bulk Al foils exhibit similar features at the electrode/electrolyte interface like those of Al thin films on substrates, such as random nucleation, quasi-2D growth, and coalescences of the  $\beta$ -LiAl patches. In this chapter, the in-depth (z-axis) phase propagation that does not occur in thin film electrodes has been elaborated using *operando* XRD and *ex situ* SEM. Based on the experimental outcomes, several schematic models have been built to illustrate important findings. Firstly, the plastic deformation zone is defined to be the regions around the  $\beta$  phase. The larger volume of the  $\beta$ -LiAl pushes the

neighboring fcc-Al grains, explaining the progressive decrease in grain size during lithiation. Secondly, the hairy regions are highlighted and are considered as a result of the mechanical effect that prevents the compressed fcc-Al from being nucleated. Yet, the hairy regions should not remain after the second cycle due to the balance of the mechanical stress. Thirdly, the volume contraction is not observed after delithiation though the ~100% volume expansion occurs by transferring fcc-Al to the  $\beta$ -LiAl. The formation of nanopores most likely causes extraordinary volume expansion upon cycling. The mechanical stresses result in a perfectly flat phase interface after a few cycles but also cause structural damage, e.g., material fall-off. To summarize, several more intrinsic issues at the cross-section are realized in addition to the ones of thin films elaborated in Chapter 5.

## 7. Li solubility range of the $\beta$ phase

Up till now, these SEM observations explain why the Al/LiAl/Al ( $\alpha/\beta/\alpha$ ) phase transformations are problematic, thus resulting in a fast degradation and poor charge efficiency when Al is used as anodes in Li-based cells. In this part, the (de-)lithiation that occurs within the Li solubility range of the  $\beta$  phase (i.e., no phase transformation involved) is investigated. Various electrochemical analytic tools and methods are used to shed light on the Li solubility within the  $\beta$  phase.

### 7.1. Background

Although this Li solubility is highlighted by multiple versions of the Li-Al phase diagrams,[43, 44] the solubility range at low temperatures was not specified due to the experimental conditions of previous phase diagram studies ( $> 400$  °C). As can be seen from Figure 1.3 in Chapter 1.1.1.4.3, the solubility range is characterized to be close to none at room temperatures while Figure 1.4 projects this range to be roughly 10% that is similar to the one obtained at elevated temperatures. As this inconsistency was never acknowledged or specified by other studies, it causes lots of debates in academia. For instance, the lithiation potential plateau only contributes to ~80% of the total capacity and there are many explanations of the last ~20% lithiation when potential plateau no longer remains, such as  $\text{Li}_2\text{Al}_3$ ,  $\text{Li}_4\text{Al}_9$  phase formations,[29, 35] amorphous  $\text{Li}_{1+x}\text{Al}$  phases,[59] and only the  $\beta$ -LiAl formation.[50, 99] Therefore, it is of vital importance to resolve this inconsistency to facilitate relevant research in the field of Al anodes.

### 7.2. Characterization by chronoamperometry

Figure 7.1a presents the outcome of the potentiostatic charge counting done for 250  $\mu\text{m}$  Al foils. The thick foils could be ideal for conducting such an experiment by minimizing the

impact of surface reactions, such as SEI formation and oxide lithiation. In other words, the charge contributed by the limited electrolyte breakdown and the nanometer scale oxide layer can be reasonably neglected. As can be seen, the Li content varies from 48.9 to 53.6 at. % at room temperature. within a potential range between 250 mV and 0 mV. The dashed line in Figure 7.1a displays the Li solubility of the  $\beta$  phase and the boundary of the Li-rich phase (i.e., beyond  $\beta$ -LiAl), determined by the coulometric titration method at 415 °C.[108] The sharp decrease of potential can be caused by adding a small amount of Li on the Li-deficit side, in agreement with our results obtained at room temperature. On the Li-rich side, the  $\beta$  and the  $\Upsilon$  phase coexist exhibiting a potential plateau at  $\sim$ 70 mV where the Li content is beyond  $\sim$ 54 at. % at this elevated temperature. For our potentiostatic charge counting, however, no indication of the  $\Upsilon$  phase can be realized based on this coulometric titration curve and the phase diagram published in 1982.[43] To further confirm that no Li-Al alloys other than the  $\beta$  phase can be formed at room temperatures electrochemically, the XRD test has been done for a deep lithiated Al foil (holding at 10 mV for 3 days). It can be clearly seen from Figure 7.1b that only the  $\beta$ -LiAl peaks are attained. Both tests strongly suggest that crystal  $\text{Li}_{1+x}\text{Al}$  phases can hardly be formed at room temperatures. It should be noted that the actual Li solubility within the  $\beta$  phase should be higher than the 4.7 at. % determined by the potentiostatic charge counting method (room temperature) and lower than the 8.2 at. % determined by coulometric titration method (415 °C).[108] Correspondingly, this solubility range should contribute to a specific capacity of roughly 200 mAh  $\text{g}^{-1}$ , normalized to Al. Last but not least, the Li solubility range of the  $\beta$  phase is clarified based on these charge counting experiments, specifically at room temperature in addition to the existing Li-Al phase diagrams, where inconsistencies still exist.

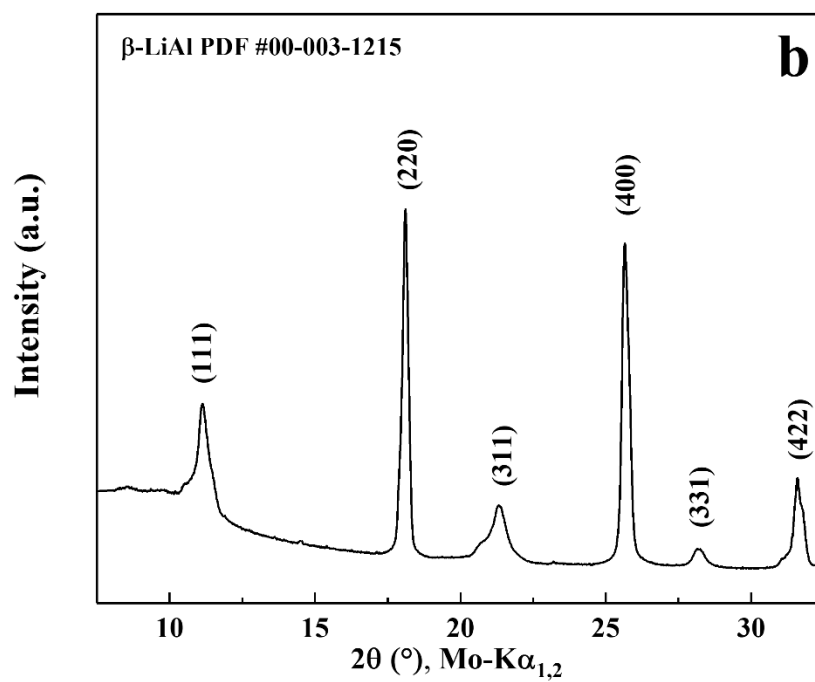
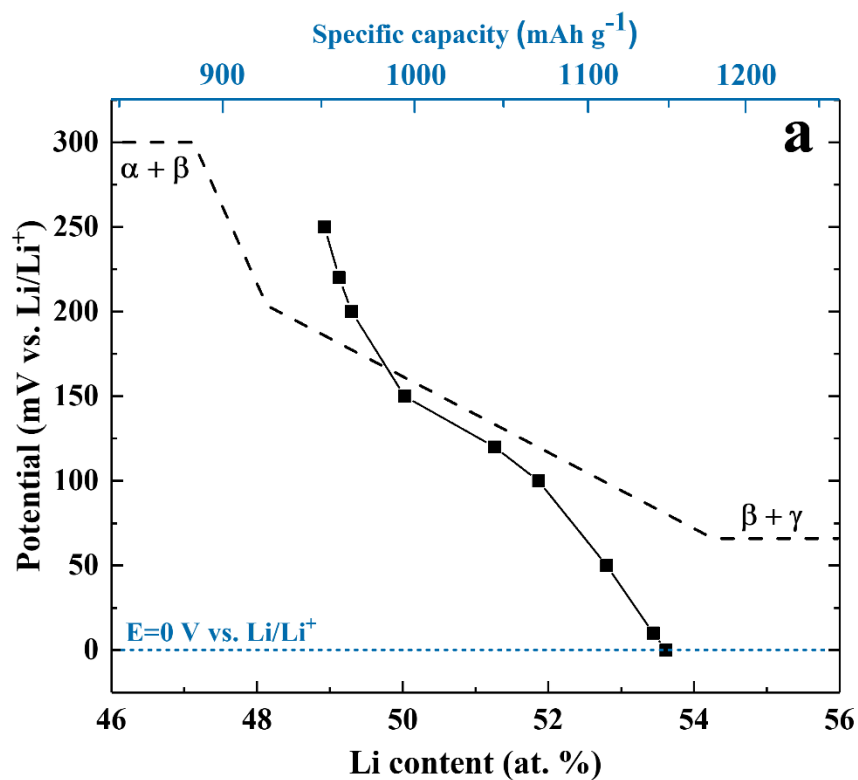


Figure 7.1. (a) Potentiostatic charge counting data obtained from 250  $\mu\text{m}$  thick Al foils covering a potential range from 250 mV to 0 mV vs. Li/Li<sup>+</sup> at room temperature. The dashed line indicates the coulometric titration curve of LiAl at 415 °C. (b) X-ray diffractogram of the deep lithiated Al foil.

### 7.3. Characterization by cyclic voltammetry

Figure 7.2a shows a typical cyclic voltammogram of Al foils against Li metal obtained at a slow scan rate of  $0.01 \text{ mV s}^{-1}$ . The sharp peaks near 0.2 V (reduction) and 0.5 V (oxidation) depict the formation of the  $\beta$ -LiAl and the reformation of the  $\alpha$  phase, respectively. Apart from the reactions of alloying and dealloying, there is also a broad but weak peak at  $\sim 0.3 \text{ V}$  (red dashed arrow) that was considered by Hudak et al. as “unexplained”. [80] Furthermore, one can notice that the CV current is almost zero prior to the lithiation peak while it does not go back to zero after the lithiation peak (red solid arrow). Surprisingly, the electrical charge integrated from the reduction current after the  $\beta$  phase formation peak (i.e.,  $\sim 0.2 \text{ V}$  to  $0 \text{ V}$ ) is the same as the one integrated from the oxidation current prior to the delithiation peak (i.e.,  $0 \text{ V}$  to  $\sim 0.4 \text{ V}$ ). This electrochemical indication suggests that the Li solubility within the  $\beta$  phase should play a role, especially that no evidence of other phases can be found.

Therefore, CV tests have been done for a partly prelithiated Al foil with a potential range from  $0.4 \text{ V}$  to  $0.1 \text{ V}$  vs.  $\text{Li/Li}^+$ , such that the formed  $\beta$ -LiAl is not transformed back to the  $\alpha$  phase. The partial prelithiation is done by initiating the potential at  $10 \text{ mV}$  for 15 minutes to achieve a homogenous nuclei distribution covering the whole electrode surface, and then holding at  $100 \text{ mV}$  to allow a one-dimensional phase boundary propagation until the amount of charge that is sufficient to lithiate a certain depth. [50, 55, 56] As illustrated in Figure 7.2b, the potential is brought down from the open-circuit voltage after prelithiation ( $\sim 0.35 \text{ V}$  vs.  $\text{Li/Li}^+$ ), a quasi-linear increase of current can be observed, agreeing with Geronov’s rule that the speed of the phase boundary propagation rate should be linearly correlated with the driving force (i.e., overpotential). [55, 56]

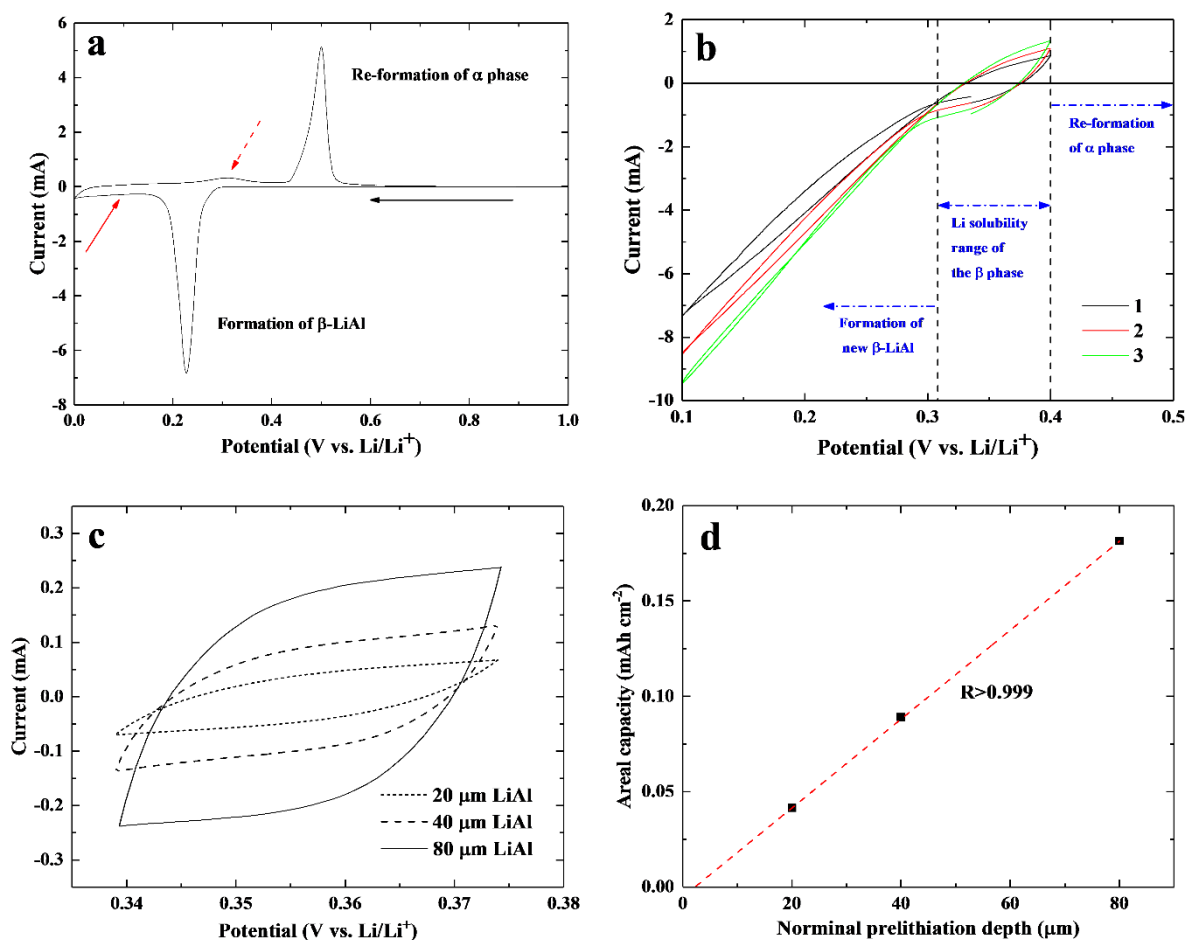


Figure 7.2. (a) The typical cyclic voltammogram of an Al foil obtained at a scan rate of  $0.01 \text{ mV s}^{-1}$  (the 2nd cycle). (b) The CV scans between 0.4 V and 0.1 V vs.  $\text{Li/Li}^+$  for the prelithiated  $100 \mu\text{m}$  Al foils under the same scan rate; the nominal prelithiation depth is  $20 \mu\text{m}$  based on the calculation of electric charge. (c) The CV cycling within the determined Li solubility range while maintaining the  $\beta\text{-LiAl}$  structure for the Al foils with various nominal prelithiation depth. (d) The areal capacity integrated from the cyclic voltammograms as a function of the prelithiation depth.

From a thermodynamic point of view, one may argue that the inserted Li atoms might preferentially drive the phase interface to lithiate more fresh Al underneath when the two phases coexist rather than saturating the  $\beta$  phase on top of the electrode. Nevertheless, the lithiation kinetics generally follow the one-dimensional thickening process (i.e., the Deal-Grove model), during which the saturation of the  $\beta$  phase is indeed possible because the Li ions

from the electrolyte must travel via the  $\beta$  phase in order to reach the phase interface and finally to facilitate continuous phase propagation. This behavior agrees with the physical nature that the  $\beta$ -LiAl is known as a superionic conductor for Li transportation while the Li diffusion in fcc-Al is extra slow.[109] Accordingly, a narrower potential window (i.e., 0.34 to 0.375 V) is chosen for CV tests to ensure a null propagation of the phase boundary while investigating whether the  $\beta$  phase can be (de)saturated.

Figure 7.2c compares the cyclic voltammograms obtained from the Al foil with various depths of prelithiation. It can be clearly seen that the deeper the prelithiation the larger the CV area (i.e., capacity, energy stored, etc.) is, suggesting that the prelithiated  $\beta$  phase is cycled within the solubility range. Otherwise, all cases would yield similar CV curves if the current is contributed by the propagation of the phase interface (i.e., growth of more  $\beta$ -LiAl). Quantitatively, the capacity is calculated based on the integration of the CV area and is plotted against prelithiation depth. As shown in Figure 7.2d, although the areal capacities exhibit perfect linearity vs. nominal lithiation depth, a value of  $\sim 2.5 \mu\text{m}$  instead of the coordinate origin is achieved by extrapolating the linear fit towards the left. This observation is indicative of the SEI formation, and thus the actual lithiation depth seems to be smaller by a constant than the nominal one calculated from the electrical charge. Quantitatively, the capacity estimated from the Al foil with a nominal lithiation depth of  $20 \mu\text{m}$  ( $0.041 \text{ mAh cm}^{-2}$ ) is slightly lower than a half and one-fourth of those from the ones with the  $40 \mu\text{m}$  ( $0.089 \text{ mAh cm}^{-2}$ ) and the  $80 \mu\text{m}$  ( $0.181 \text{ mAh cm}^{-2}$ ), respectively. If taking into consideration the electrical charge that is consumed by SEI formation, perfect two-fold relationships can be achieved.

In addition, CV tests at  $0.1 \text{ mV s}^{-1}$  have been done to examine how the prelithiated Al foil behaves under a higher rate. The complete cyclic voltammograms are plotted in Figure S7.1 and the calculated capacities are plotted in Figure S7.1b for the comparison with Figure 7.2c-d. As can be seen, a nominal prelithiation depth of  $20 \mu\text{m}$  (i.e.,  $\sim 40 \mu\text{m}$   $\beta$ -LiAl) gives

similar capacities under both  $0.01 \text{ mV s}^{-1}$  and  $0.1 \text{ mV s}^{-1}$ . Once the nominal prelithiation depth is increased to  $40 \text{ }\mu\text{m}$ , the capacity obtained at  $0.01 \text{ mV s}^{-1}$  is already larger than that at  $0.1 \text{ mV s}^{-1}$ . This difference becomes more and more evident with deeper prelithiations, implying that a scan rate of  $0.1 \text{ mV s}^{-1}$  might still be too high though the Li diffusion within the  $\beta$  phase is relatively fast.

#### 7.4. Characterization by galvanostatic charge-discharge

Figure 7.3a illustrates the characteristic galvanostatic profile of an Al foil using Li metal as the counter electrode (i.e., half-cell). Two wide plateaus can be observed at  $\sim 0.3 \text{ V}$  and  $\sim 0.45 \text{ V}$ , corresponding to the lithiation and the delithiation process, respectively. The instantaneous potential drop at time zero (i.e. the potential dip at  $\sim 0.1 \text{ V}$ ) refers to the extra energy required for the nucleation that is probably due to the localized distortion and mechanical strain.[27, 32, 50, 81] It should be noted that the plateau at  $\sim 0.3 \text{ V}$  no longer preserves during the last  $\sim 20\%$  of the lithiation process. Qin et al. observe a disappearance of the  $\beta$  phase peak during *in situ* XRD test and suggest the formation of amorphous  $\text{Li}_{1+x}\text{Al}$  phases after this long two-phase plateau.[59] Nevertheless, another study points out that Li-rich phases (i.e. higher Li content than the  $\beta$ -LiAl) can only form at elevated temperature regime, e.g.,  $>60 \text{ }^\circ\text{C}$ . As no direct evidence of the phase formation other than the  $\beta$  phase can be found, it is believed that the last  $\sim 20\%$  capacity (indicated by a red arrow) is attributed by the Li solubility while maintaining the crystalline structure of the  $\beta$ -LiAl.

As the  $\beta$ -LiAl is considered as a superionic conductor,[110] the capacity originated from the solubility range is unlikely limited by the Li diffusion. Based on the outcome from the CV tests, GCD cycling is conducted in the potential range from  $0.33 \text{ V}$  to  $0.4 \text{ V}$ , between which the phase propagation (i.e., growth of more  $\beta$ -LiAl) is not expected to occur. Figure 7.3b displays the GCD profiles at under various C-rates of the same electrode (i.e., the Al foil with

80  $\mu\text{m}$  nominal lithiation depth), which generally stick to the higher the rate, the lower the capacity. Importantly, the capacity difference between 2 C and 1 C is  $\sim 0.09 \text{ mAh cm}^{-2}$  and decreases to less than  $\sim 0.02 \text{ mAh cm}^{-2}$  when comparing 0.5 C with 0.2 C.

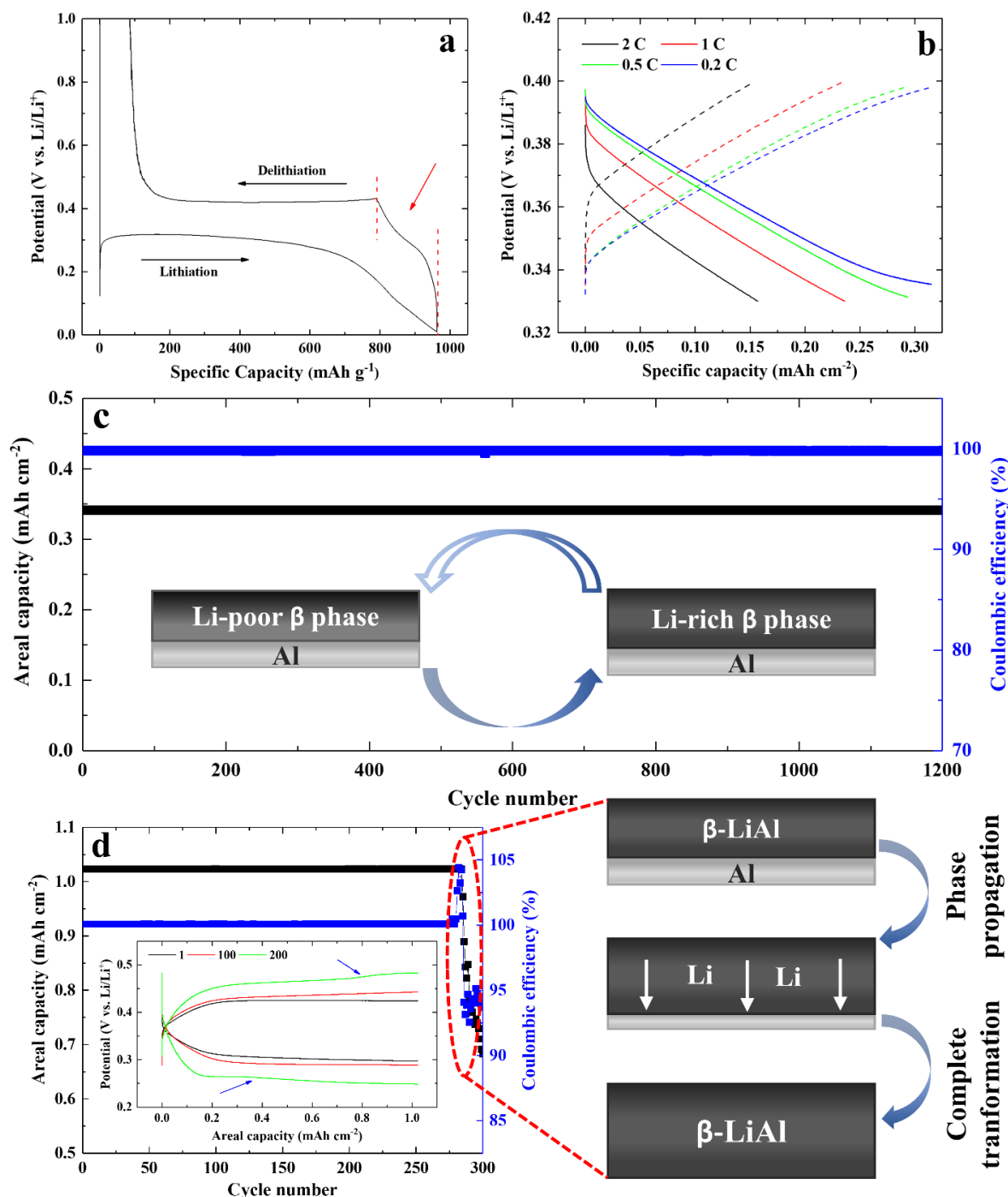


Figure 7.3. (a) The typical galvanostatic curves of an Al foil obtained at a rate of C/40 (the 2nd cycle). (b) The GCD profiles at various C rates obtained from a 100  $\mu\text{m}$  Al foil electrode with

a nominal prelithiation depth of 80  $\mu\text{m}$ . The potential range is fixed between 0.33 V and 0.4 V vs.  $\text{Li}/\text{Li}^+$  to avoid the formation of more  $\beta\text{-LiAl}$ . The cycling performance of such an electrode is presented in (c) by precisely controlling the (de-)lithiation depth within the solubility range and (d) by exploring the full capacity of the solubility range of the  $\beta\text{-LiAl}$  layer. The inset and illustration of (d) describe the electrode degradation process (i.e., gradual propagation of the phase front) when cycling near the Li solubility limit.

Upon understanding these features, prolonged cycling life can be realized by this partially prelithiated Al foil electrode. Such an electrode (i.e., a  $\sim 160\ \mu\text{m}$   $\beta\text{-LiAl}$  layer as the active material on top of a  $\sim 20\ \mu\text{m}$  Al layer as the current collector is prepared to mimic the structure of commercially available graphite anodes (i.e., a  $\sim 100\ \mu\text{m}$  slurry-based graphite composite electrode pasted on a  $10\ \mu\text{m}$  copper foil).[106] The cycling performance of a half-cell architecture was evaluated under GCD mode using  $0.25\ \text{mA cm}^{-2}$  with a capacity of  $\sim 0.34\ \text{mAh cm}^{-2}$ , which was determined by the preliminary electrochemical tests. It can be clearly seen that Figure 7.3c exhibits an extraordinary 1000 stable cycles. Although the capacity is still small, one can always adjust the thickness of the Al foil to reach the desired areal capacity, especially that Al is an industrial approachable product. For instance, an exceptionally thick Al foil (e.g., 1 mm) can significantly boost the areal capacity by slightly increasing the cell volume. In this case, the 1 mm thick foil with a nominal prelithiation depth of 0.8 mm will yield an areal capacity of more than  $10\ \text{mAh cm}^{-2}$  while another 0.2 mm unlithiated Al layer can ensure the overall electrode stability.

Moreover, it should be noted that there is a mismatch between the capacity shown in Figure 7.3b and the one calculated from the charge counting experiments, implying that the solubility range of the  $\beta\text{-LiAl}$  might not be fully engaged. One of the possible explanations could be that it is not an accurate way to (de-)saturate the solubility range of the  $\beta\text{-LiAl}$  via potential control because potential is considered as a surface property. The Li concentration

gradient should still exist if the  $\beta$ -LiAl is too thick at the given charge-discharge rate, especially that the Li diffusivity in the  $\beta$  phase is known to be at least three orders of magnitude higher than that in the  $\alpha$  phase.[39, 50, 61, 67] In other words, the potential range used in Figure 7.3b (i.e. between 0.33 V and 0.4 V) does not represent the full capacity of the solubility range of the  $\beta$ -LiAl. As a result, another cycling test is done by fixing the capacity at a higher level of  $\sim 1 \text{ mAh cm}^{-2}$  and the outcome is shown in Figure 7.3d. It can be noticed that the same electrode exhibits  $\sim 280$  stable cycles and suddenly collapse to almost no capacity at the 300<sup>th</sup> cycle. The illustration aside describes the electrode degradation process, which includes a gradual propagation of the phase front during the repetitive cycles, and finally, the  $\sim 20 \text{ }\mu\text{m}$  Al under the  $\beta$ -LiAl gets fully lithiated. As can be seen from the inset of Figure 7.3d, the potential window is getting larger and larger to maintain the capacity of  $\sim 1 \text{ mAh cm}^{-2}$  with noticeable potential kinks (blue arrows) that may refer to the nucleation of the  $\beta$  and the  $\alpha$  phase during lithiation and delithiation, respectively. This can be another indication of this gradual phase propagation if the cycled capacity is close/beyond the actual solubility range. Once the Al layer underneath the  $\beta$ -LiAl is completely transformed, the electrode lost its integrity and exhibits the intrinsic shortcomings (i.e., electrode collapse after 280 cycles). Nevertheless, this problematic phase propagation will be unlikely occurring in a full cell, in which the amount of Li is fixed.

## 7.5. Li diffusivity within the $\beta$ phase

The CV sequence shown in Figure 7.2c can also help to shed light on the Li diffusivity in the  $\beta$  phase. Our results suggest that the Li diffusivity will be sufficient for a 160  $\mu\text{m}$   $\beta$ -LiAl layer, but not for a 200  $\mu\text{m}$   $\beta$ -LiAl layer (Figure S7.2). It seems that Li diffusion within the  $\beta$ -LiAl is partly dependent on mechanical stress. By conducting the same CV tests (Figure S7.2a-c) shown in Figure 7.2c for a thicker Al foil (0.25 mm), a perfect linear relationship obtained at 0.01  $\text{mV s}^{-1}$  can hardly be achieved by decreasing the scan rate to as low as 0.002  $\text{mV s}^{-1}$  (Figure S7.2d). A possible explanation would be that a 2.5 times thicker foil causes a higher mechanical force that compresses the  $\beta$ -LiAl layer, thereby restricting the Li diffusion. The Li diffusion variation that is caused by the foil thickness becomes more evident once the capacities calculated from the CV curves are plotted against prelithiation depths (Figure S7.3). Nevertheless, it requires independent investigations to establish the correlations between Li diffusivities and mechanical compressions.[111]

Therefore, in this chapter, only a diffusivity range of Li within the  $\beta$  phase can be reasonably estimated for 0.1 mm thick foils from the cyclic voltammograms assuming the driving force does not vary significantly within the narrow potential range shown in Figure 7.2c. Based on Fick's law of diffusion in Equation 7.1:

$$J = -D \frac{C_2 - C_1}{\Delta z} \quad (7.1)$$

Where  $J$  represents the Li flux from the electrolyte to the  $\beta$ -LiAl electrode in  $\text{cm}^{-2} \text{s}^{-1}$ ,  $D$  is the diffusion coefficient of Li within the  $\beta$  phase,  $C_1$  and  $C_2$  are the concentrations of the Li-rich  $\beta$  phase and the Li-poor  $\beta$  phase in  $\text{mol cm}^{-3}$ , respectively,  $\Delta z$  is the diffusion distance that is equivalent to the thickness of the  $\beta$ -LiAl layer in our case.

Firstly, the Li flux can be estimated by the electrical charge integrated from the cyclic voltammogram of the Al foil with 80  $\mu\text{m}$  nominal prelithiation:

$$J = \frac{0.182 \times 10^{-3} Ah \text{ cm}^{-2} \times 3600 \text{ s h}^{-1} \times 1.036 \times 10^{-5} \text{ mol C}^{-1}}{(35 \text{ mV} \times 2)/0.01 \text{ mV s}^{-1}}$$

$$= 9.7 \times 10^{-10} \text{ mol cm}^{-2} \text{ s}^{-1}$$

Secondly, the Li concentrations within the Li-poor  $\beta$ -LiAl (49:51 ratio) and within the Li-rich  $\beta$ -LiAl (54:46) can be calculated from the chemical stoichiometry to be  $0.0474 \text{ mol cm}^{-3}$  and  $0.0476 \text{ mol cm}^{-3}$ , respectively. In other words, the Li concentration difference in the  $\beta$ -LiAl between the electrode/electrolyte interface and the  $\alpha/\beta$  interface will be  $-0.0002 \text{ mol cm}^{-3}$  ( $\Delta C$ ). Moreover, the distance of diffusion will be the thickness of the  $\beta$ -LiAl layer, which should be  $160 \text{ }\mu\text{m}$  assuming a 100% volume expansion. From our analysis, we know that the Li diffusivity will be sufficient for a  $160 \text{ }\mu\text{m}$   $\beta$ -LiAl layer, but not for a  $200 \text{ }\mu\text{m}$   $\beta$ -LiAl layer. As a result, the diffusivity range of Li in the  $\beta$ -LiAl can be estimated based on the same calculations to be within the range from  $6.8 \times 10^{-8}$  to  $7.8 \times 10^{-8} \text{ cm}^2 \text{ s}^{-1}$ , which is consistent with the previously reported value of  $7.7 \pm 0.2 \times 10^{-8} \text{ cm}^2/\text{s}$  that was determined at room temperature [39].

In addition, the Li diffusivity is estimated to be  $7 \times 10^{-8} \text{ cm}^2 \text{ s}^{-1}$  using the cyclic voltammogram at  $0.1 \text{ mV s}^{-1}$  with  $40 \text{ }\mu\text{m}$  nominal prelithiation, further strengthening the reliability of the diffusivity range reported here. Although the  $\beta$ -LiAl is defined as a superionic conductor, the diffusion speed can be strongly dependent on the temperature.[61, 109] In other words, the Li diffusion speed with the  $\beta$  phase may be significantly slower at room temperatures, which can be partly supported by the estimated diffusivity values here and by other studies.[39, 40, 67] Nevertheless, systematic investigations are necessary to achieve the accurate Li diffusion coefficient at room temperature, e.g., potentiostatic experiments.

The similar capacities obtained at 0.2/0.5 C and the different capacities at 1C/2C during GCD tests (Figure 7.3a) can also shed light on the Li diffusion in the  $\beta$ -LiAl together with the calculated diffusivity values, and optimized C-rate can be calculated and coupled with a proper

depth of prelithiation. For instance, an areal current of  $\sim 0.25 \text{ mA cm}^{-2}$  is equivalent to  $\sim 1 \text{ C}$  (or  $\sim 0.15 \text{ mA cm}^{-2}$  to  $0.5 \text{ C}$ ), considering the capacity contributed by the solubility range of an Al foil with  $80 \text{ }\mu\text{m}$  prelithiation depth (i.e.,  $\sim 160 \text{ }\mu\text{m}$   $\beta$ -LiAl). The sufficient Li diffusion speed along the z-axis of the  $\beta$ -LiAl layer is calculated to be at least  $0.044 \text{ }\mu\text{m s}^{-1}$  without limiting the (de)saturation processes, while the actual Li diffusion velocity is greater (between  $0.046 \text{ }\mu\text{m s}^{-1}$  and  $0.053 \text{ }\mu\text{m s}^{-1}$ ) based on the diffusivity values presented before.

## 7.6. Full cell demonstration with the $\beta$ -LiAl anode

Upon realizing the solubility range of the  $\beta$ -LiAl, the electrode behavior covering a complete potential range is illustrated in Figure 7.4a. The  $\beta$ -LiAl should be stable as long as it is properly maintained within the solubility range (i.e., dashed rectangle) where no phase propagation exists. In addition, the volume change is only  $\sim 5\%$ , thus maintaining the mechanical stability of the electrode. Although the capacity of the  $\beta$ -LiAl solubility region is still less than 20% as compared to the one that originated from the  $\alpha/\beta/\alpha$  phase transformations, it can already match some of the state-of-the-art cathodes. Coupling with a commercial  $\text{LiFePO}_4$  electrode (CUSTOMCELLS, Germany) which has an areal of  $\sim 1 \text{ mAh cm}^{-2}$ , the cycling performance of the  $\beta$ -LiAl is evaluated in a full cell to demonstrate the feasibility for practical uses. The assembled full cell exhibits an excellent cycle life with 87% capacity retention after 600 cycles, corresponding to  $\sim 99.96\%$  capacity retention per cycle (Figure 7.4b). This cycling performance already surpasses some of the commercially available batteries, exhibiting great potentials in real applications. Scientifically, it also explains the inconsistencies from the literature regarding the cycling performance of Al anodes: some studies report less than ten cycles while others achieved hundreds of cycles. For full cells where the capacity of the cathode is small compared to the capacity stemming from the Li solubility range in the  $\beta$  phase, an indefinite cycle life can be expected for Al anodes. In addition to the

outstanding cycling performance demonstrated here, multiple optimization approaches in a scientific and systematic way, are recommended to explore methodologies for the best performance of such Al anodes.

The cross-sectional SEM of the prelithiated  $\beta$ -LiAl electrode prior to the cycling test is provided in Figure 7.4c, which clearly illustrates the active layer ( $\beta$ -LiAl) and the current collector layer (Al, fcc). Optical images are also taken for the  $\beta$ -LiAl electrode right after electrochemical prelithiation (Figure 7.4d). The surface of the as-lithiated electrode is covered with a dense layer of the dark  $\beta$ -LiAl while the backside is clearly fcc-Al (i.e., current collector) but with tiny creases. In the middle of the cycling, the cell is disassembled, and the front/back sides of the cycled  $\beta$ -LiAl are also shown in Figure 7.4d. It can be observed that the  $\beta$ -LiAl on the front side becomes larger with slight cracking. As for the backside, the horizontally enlarged  $\beta$ -LiAl layer is proved by observing a ring of the  $\beta$  phase. Furthermore, the creases have become more evidence but are still sufficient to help ensure the integrity of the electrode, even after hundreds of cycles. It should be noted that the crease development on the backside can be due to the mechanical deformation of the soft Al matrix that is elaborated in a previous study.[95]

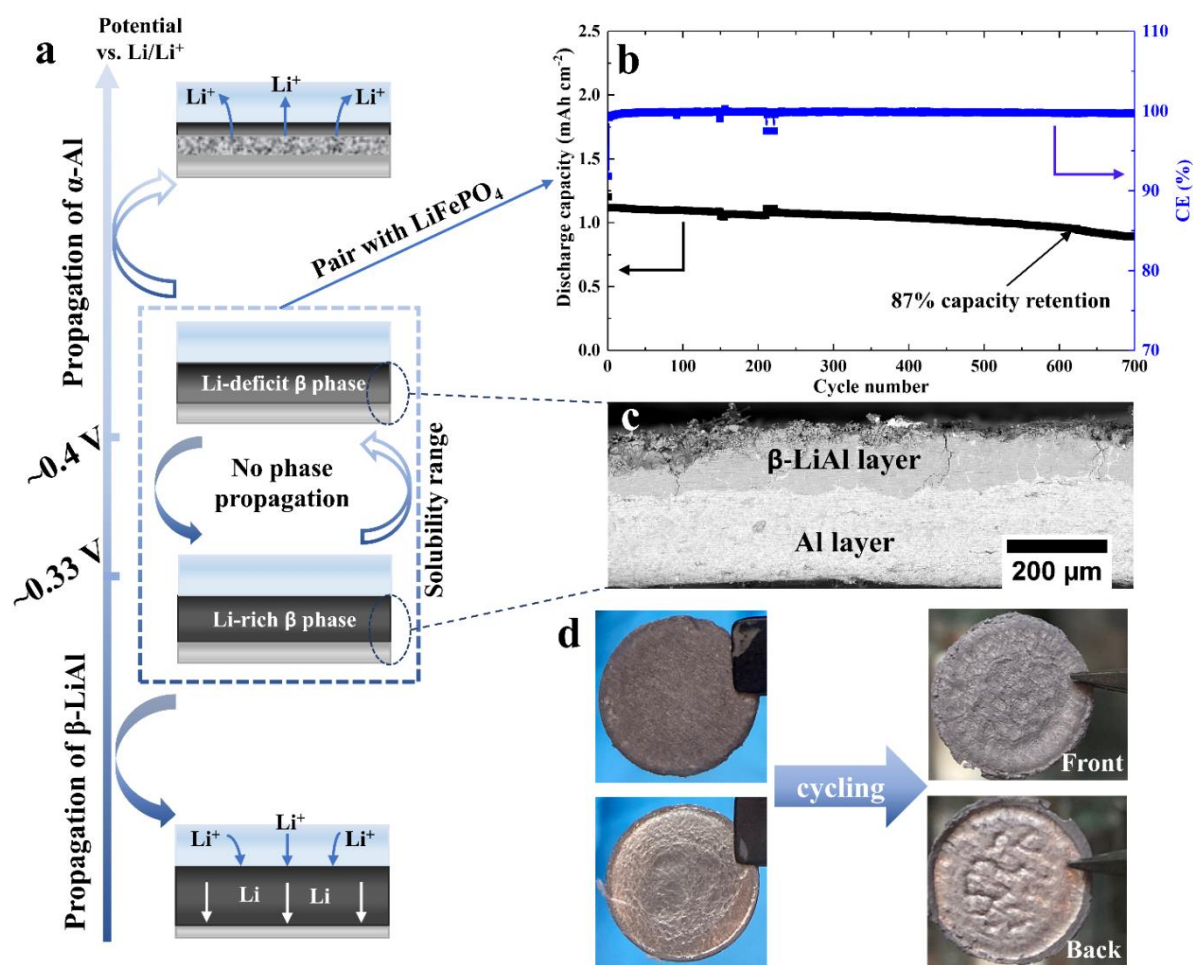


Figure 7.4. (a) Schematic profiles of the LiAl electrode state under gradients of electric potential that clearly illustrate the solubility range of the  $\beta$  phase. (b) The cycling performance of the full cell consisting of a  $\beta$ -LiAl anode and a commercial LFP cathode. (c) Cross-sectional SEM image of a prelithiated Al foil taken by a BSE detector, of which the lithiated  $\beta$ -LiAl layer and the unlithiated Al layer can be observed. (d) Photographs of the front and the backside of the as-lithiated and the cycled  $\beta$ -LiAl electrodes.

## 7.7. Summary

To summarize, various electrochemical analytic tools and methods are used to shed light on the Li solubility within the  $\beta$ -LiAl. The Li solubility range of the  $\beta$  phase is determined to be roughly 5 at% by a series of potentiostatic charge counting experiments at room temperature. Moreover, the CV tests of partially lithiated Al foils show that the  $\beta$  phase can be

(de-)saturated without propagating the phase front towards the unlithiated  $\alpha$  phase. If the GCD mode is strategically controlled by taking into consideration the solubility range, the cycling life of  $\beta$ -LiAl anode can be significantly improved. A full cell consisting of such an anode and a commercial LiFePO<sub>4</sub> cathode demonstrates an impressive cycling performance of 600 cycles with 87% capacity retention at 1 C rate. Besides presenting the technical and the financial feasibility of a prelithiated Al foil electrode towards commercialization, this part also provides fundamental data for the  $\beta$ -LiAl phase at room temperature that complements the existing Li-Al phase diagrams.

## 8. Conclusions and Outlook

Aluminum has been explored as an electrode material for lithium storage since 1970s. The chemical properties make Al a competitive anode candidate for lithium-ion or lithium-based batteries. However, Al-based anodes hardly draw same attention as compared to silicon or carbon counterparts, and thus leave substantial research gaps. Not only did this dissertation try to fill these research gaps via systematic investigation, but also sheds light on the possible applications of Al-based anodes for electrochemical energy storage.

### 8.1. Summary of literature review

Lithium storage has been playing a crucial role since Sony introduced the concept of LIBs in early 1990s. The current state-of-the-art anode has not been changed significantly since then, and remains a slurry-based graphite powder, although little silicon inclusion is demonstrated to increase the specific capacity to some extent. Alloy materials are surely one of the possible anode candidates for future energy storage. While researchers are attracted by the extraordinarily high specific capacity of silicon, other important aspects that determine whether an electrode material can potentially be commercialized are somehow ignored. In other words, a successful electrode product always reaches a balance of financial feasibilities, manufacturing simplicities, performance effectiveness, and so forth. By considering those criteria, this Ph.D. project focuses on aluminum, of which some properties can be beneficial for practical applications.

Aluminum is a popular technical material that can be easily found in daily life due to its light weight, low cost, and easy-to-fabricate features. Electrochemically, Al can be lithiated at a relatively low potential vs.  $\text{Li/Li}^+$  upon the formation of  $\beta\text{-LiAl}$  at room temperature, giving a wide potential plateau and a simple stoichiometry. More importantly, Al foils already

function as cathodic current collectors in commercial LIB cells. If a piece of Al foil can be used to replace the current anode, the copper foil current collectors can potentially be omitted. In addition, the Al foil anode becomes completely monolithic and solid-state without adding polymer binders and conductive additives, thereby significantly simplifying the manufacturing processes, and reducing the production costs. All in all, Al exhibits great potentials as a future anode material for LIBs by counting all important aspects, though the specific capacity is not the highest.

The drawbacks of Al as an anode in LIBs are also obvious, including a short cycling life, poor charge efficiencies, and possible Li trappings. Nevertheless, none of these issues has been elaborated and the underlying mechanisms are still unclear. Unlike graphite or silicon anodes, the literature is significantly limited, and most studies were done in the last century. Moreover, inconsistencies can still be found from the available literature, such as Li-Al phase diagrams and the formation of Li-rich phases.

## **8.2. Conclusions from experimental results**

The experimental data of this thesis are presented based upon an *operando* light microscopy platform, thus yielding a series of dynamic observations of the phase transformations between fcc-Al and the  $\beta$ -LiAl at room temperature. With the help of other characterization techniques mentioned in the Experimental Section, the collected results successfully fill the research gaps and highlight the random nucleation, the 3D to 2D phase growth, and the coalescences among the isolated  $\beta$ -LiAl patches during lithiation (**Chapter 3**). The phase transformation from fcc-Al to the  $\beta$ -LiAl is elaborated at a granular level. The results suggest that the growth and propagation of the  $\beta$ -LiAl are dependent on the out-of-plane orientations of Al grains (**Chapter 4**). Once delithiation starts, cracks are formed within the  $\beta$ -LiAl patches due to its brittleness while delamination occurs simultaneously. The subsequent

lithiation always continues at the delithiated regions because of a lower energy barrier for nucleation. Furthermore, it is the first time to report the formation of nanopores upon cycling, verifying that the  $\beta$ -LiAl does not contract significantly as Li is being extracted. Therefore, the overall volume of the Al electrode keeps increasing during cycling as nanoporosities occupy more and more space. This behavior is also supported by the *in situ* stress test tool that yields an asymmetrical stress profile during an electrochemical cycle (**Chapter 5**). Both the nanoporosity and the stress profile are new and unique, providing relevant information towards the field of Al-based anodes for LIBs.

However, the interesting observations and behaviors are seemingly intrinsically bonded to the phases transformations of the Li-Al system since substrate-based Al thin films and monolithic Al foils exhibit similar features during electrochemical cycling against Li (**Chapter 6**). Hence, the successful utilization of Al anodes requires strategical pathways that are capable of resolving or circumventing those intrinsic shortcomings. This thesis proposes a novel approach to cycle the  $\beta$ -LiAl anode within a specific range once its Li solubility range is realized at room temperature (**Chapter 7**). A homogenous layer of the  $\beta$ -LiAl is grown on top of a piece of Al foil via prelithiation, resulting in a unique anode architecture with the top and the bottom layer as the active material and the current collector, respectively. A full LIB cell with such an anode and a commercially available cathode exhibit an excellent cycling capability that competes with the stage-of-the-art LIB products. Last but not least, this thesis also provides new and relevant scientific insights along with experimental observations and performance assessment.

### **8.3. Outlook and perspectives**

Clearly, there are always gaps between scientific data and practical applications, although utilization of Al-based anodes is preliminarily shown to be financially and technically

feasible on a lab scale. This dissertation has laid the foundation for a strategical utilization of Al-based anodes, and thus the future work should focus on the performance optimization via non-material aspects. Firstly, electrolyte/additive engineering holds great potentials for enhancing the reliability of Al-based anodes by growing stable and protective SEI.[112, 113] As the low potential vs. Li/Li<sup>+</sup> nature of Al-based anodes makes SEI unavoidable, electrolyte selection that is closely related to properties of SEI layers should be of vital importance. Moreover, the electrode stability is found to be heavily dependent on mechanical strain/stress in this work. Therefore, delicate electrode shapes or surface coatings may be beneficial through uniformly distributing the mechanical stress and circumventing/minimizing the localized strain,[28, 95, 114] such that the electrode integrity can be maintained during cycling. Systematic investigations are suggested for the proposed future works to achieve conclusive understandings.

The author has been working on the topics from the EES field for more than 4 years and realized that the term “specific capacity” in “mAh g<sup>-1</sup>” is often marked as the make-or-break metrics in academia for assessing if an electrode material is competitive. Nevertheless, the reported “mAh g<sup>-1</sup>” is normalized to active material as an unwritten rule. In this way, other components, such as current collectors, binders, and electrical conductivity enhancers are intentionally neglected. Usually, these components occupy a major portion of a LIB cell, both in weight and volume. Furthermore, manufacturing complexity, safety compliance, and financial feasibility should indeed be considered as well. Gogotsi and Simon have already argued that the numbers in “mAh g<sup>-1</sup>” might not be 100% representative.[107] An example could be a very low-density graphene electrode that yields an extraordinarily high number of “mAh g<sup>-1</sup>”, but the low density is only equivalent to a moderate volumetric capacity in “mAh cm<sup>-3</sup>”. The number becomes even lower by counting typical components of a device and can barely match the current-state-of-the-art products. It undoubtedly reminds academia what are

the true performance metrics in EES field.

The above perspectives do not aim to underestimate the importance of “mAh g<sup>-1</sup>”, nor to overestimate that of “mAh cm<sup>-3</sup>”. The author is just trying to convey the idea that some properties may make an electrode material perform extremely well in certain fields and applications. Taking the low-density graphene electrode mentioned previously as an example, it can hardly be competitive in EV applications as EVs may become oversized due to the low “mAh cm<sup>-3</sup>” and cause traffic issues. Yet its high “mAh g<sup>-1</sup>” could be ideal for drone applications, where the weight of a battery pack is still one of the main obstacles that prevent a drone from flying longer and farther. Similarly, we may extend the knowledge to other fields, such as printed batteries for on-chip applications or stationary batteries for renewable energy storage. In the former case, the battery pack is extraordinarily thin to match the size of microelectronics, such that an areal capacity in “mAh cm<sup>-2</sup>” should be more indicative. In the latter case, neither weight nor space is the limiting factor anymore because this kind of equipment is always located in remote areas, e.g., wind or solar farms. Therefore, people might concern “mAh \$<sup>-1</sup>” more than other factors. It is believed that the Al-based anodes presented in this thesis should show great potentials in lowering “mAh \$<sup>-1</sup>”, while acceptable “mAh g<sup>-1</sup>”, “mAh cm<sup>-3</sup>”, and “mAh cm<sup>-2</sup>” are maintained.

Moreover, it shall be noted that research in anode and cathode materials is usually isolated to gain neat scientific insights. For instance, a half-cell configuration of anode vs. Li metal would eliminate the influences of a cathode and vice versa. Nonetheless, we should not completely neglect the other electrode as a battery product is in the full-cell format. When pushing the anode capacity towards an extremely high level, e.g., Si anode, one should consider: will an anode with ~3,500 mAh g<sup>-1</sup> be greatly beneficial if it is going to be paired with a cathode with ~150-300 mAh g<sup>-1</sup>? The specific capacity of cathode materials can hardly be improved since the brittle nature of these layered ceramic oxides are almost impossible to

tolerate  $\geq 10\%$  volume expansion. Comments are indeed required in this regard to shed light on the manufacturing aspects. A question associated with such a high-capacity anode is whether the  $\sim 300\%$  volume change can be tolerated by the state-of-the-art battery pack. Here, technical feasibilities might be negatively affected if a new battery design is needed, although outstanding capacity merits are achieved.

All in all, this dissertation suggests that, apart from aiming for extraordinarily high the capacity merits of the active materials, other aspects such as mass of each component, thickness of each layer, and N/P ratio for a full cell should be clearly stated in scientific reports. Recommendations in engineering perspectives, e.g., how to pursue an electrode material within the current battery industry, are also very helpful for future applications.

## References

1. *Today in Energy*, in *U.S. Energy Information Administration*. 2019.
2. Obrovac, M.N. and V.L. Chevrier, *Alloy Negative Electrodes for Li-Ion Batteries*. Chemical Reviews, 2014. **114**(23): p. 11444-11502.
3. Nitta, N., et al., *Li-ion battery materials: present and future*. Materials Today, 2015. **18**(5): p. 252-264.
4. Scrosati, B. and J. Garche, *Lithium batteries: Status, prospects and future*. Journal of Power Sources, 2010. **195**(9): p. 2419-2430.
5. Etacheri, V., et al., *Challenges in the development of advanced Li-ion batteries: a review*. Energy & Environmental Science, 2011. **4**(9): p. 3243-3262.
6. Yoo, H.D., et al., *On the challenge of developing advanced technologies for electrochemical energy storage and conversion*. Materials Today, 2014. **17**(3): p. 110-121.
7. Zu, C.-X. and H. Li, *Thermodynamic analysis on energy densities of batteries*. Energy & Environmental Science, 2011. **4**(8): p. 2614-2624.
8. Steiger, J., *Mechanisms of dendrite growth in lithium metal batteries*. 2015.
9. Yoshio, M., *Lithium-Ion Batteries*. Lithium-Ion Batteries : Science and Technologies, ed. R.J. Brodd, A. Kozawa, and SpringerLink. 2010: New York, NY : Springer New York.
10. Steiger, J., D. Kramer, and R. Mönig, *Mechanisms of dendritic growth investigated by in situ light microscopy during electrodeposition and dissolution of lithium*. Journal of Power Sources, 2014. **261**(Supplement C): p. 112-119.
11. Kim, Y.-J., et al., *Guided Lithium Deposition by Surface Micro-Patterning of Lithium-Metal Electrodes*. ChemElectroChem, 2018. **5**(21): p. 3169-3175.
12. An, S.J., et al., *The state of understanding of the lithium-ion-battery graphite solid electrolyte interphase (SEI) and its relationship to formation cycling*. Carbon, 2016. **105**: p. 52-76.
13. Sandhya, C.P., B. John, and C. Gouri, *Lithium titanate as anode material for lithium-ion cells: a review*. Ionics, 2014. **20**(5): p. 601-620.
14. Jia, X., et al., *Building flexible Li<sub>4</sub>Ti<sub>5</sub>O<sub>12</sub>/CNT lithium-ion battery anodes with superior rate performance and ultralong cycling stability*. Nano Energy, 2014. **10**: p. 344-352.
15. Su, X., et al., *Silicon-Based Nanomaterials for Lithium-Ion Batteries: A Review*. Advanced Energy Materials, 2014. **4**(1): p. 1300882-n/a.
16. Ashuri, M., Q. He, and L.L. Shaw, *Silicon as a potential anode material for Li-ion batteries: where size, geometry and structure matter*. Nanoscale, 2016. **8**(1): p. 74-103.
17. Lee, P.-K., et al., *Polyimide capping layer on improving electrochemical stability of silicon thin-film for Li-ion batteries*. Materials Today Energy, 2019. **12**: p. 297-302.
18. Miao, J. and C.V. Thompson, *Kinetic Study of the Initial Lithiation of Amorphous Silicon Thin Film Anodes*. Journal of The Electrochemical Society, 2018. **165**(3): p. A650-A656.
19. Xiao, X., et al., *Nanostructured Germanium Anode Materials for Advanced Rechargeable Batteries*. 2017. **4**(6): p. 1600798.
20. Al-Obeidi, A., et al., *Mechanical stresses and crystallization of lithium phosphorous oxynitride-coated germanium electrodes during lithiation and delithiation*. Journal of Power Sources, 2016. **306**: p. 817-825.
21. Liu, L., et al., *Tin-based anode materials with well-designed architectures for next-generation lithium-ion batteries*. Journal of Power Sources, 2016. **321**: p. 11-35.
22. Zhang, W.-J., *Lithium insertion/extraction mechanism in alloy anodes for lithium-ion batteries*. Journal of Power Sources, 2011. **196**(3): p. 877-885.
23. Bogart, T.D., A.M. Chockla, and B.A. Korgel, *High capacity lithium ion battery anodes of silicon and germanium*. Current Opinion in Chemical Engineering, 2013. **2**(3): p. 286-293.
24. Hamon, Y., et al., *Aluminum negative electrode in lithium ion batteries*. Journal of Power Sources, 2001. **97-98**(Supplement C): p. 185-187.
25. Li, Q. and N.J. Bjerrum, *Aluminum as anode for energy storage and conversion: a review*. Journal of Power Sources, 2002. **110**(1): p. 1-10.
26. Lindsay, M.J., G.X. Wang, and H.K. Liu, *Al-based anode materials for Li-ion batteries*. Journal of Power Sources, 2003. **119-121**(Supplement C): p. 84-87.

27. Wang, C., et al., *Electrochemical Properties of Nanostructured Al<sub>1-x</sub>Cu<sub>x</sub> Alloys as Anode Materials for Rechargeable Lithium-Ion Batteries*. Journal of the Electrochemical Society, 2008. **155**(9): p. A615-A622.
28. Tong, X., et al., *Carbon-Coated Porous Aluminum Foil Anode for High-Rate, Long-Term Cycling Stability, and High Energy Density Dual-Ion Batteries*. Advanced Materials, 2016. **28**(45): p. 9979-9985.
29. Doglione, R., et al., *Microstructure evolution and capacity: Comparison between 2090-T8 aluminium alloy and pure aluminium anodes*. Journal of Alloys and Compounds, 2017. **727**: p. 428-435.
30. Ji, B., et al., *A Novel and Generalized Lithium-Ion-Battery Configuration utilizing Al Foil as Both Anode and Current Collector for Enhanced Energy Density*. Advanced Materials, 2017. **29**(7): p. 1604219.
31. Wang, M., et al., *Low-Cost Metallic Anode Materials for High Performance Rechargeable Batteries*. Advanced Energy Materials, 2017. **7**(23): p. 1700536.
32. Tahmasebi, M.H., et al., *Insights into Phase Transformations and Degradation Mechanisms in Aluminum Anodes for Lithium-Ion Batteries*. Journal of The Electrochemical Society, 2019. **166**(3): p. A5001-A5007.
33. Liu, Y., et al., *In Situ Transmission Electron Microscopy Observation of Pulverization of Aluminum Nanowires and Evolution of the Thin Surface Al<sub>2</sub>O<sub>3</sub> Layers during Lithiation–Delithiation Cycles*. Nano Letters, 2011. **11**(10): p. 4188-4194.
34. Oltean, G., et al., *On the origin of the capacity fading for aluminium negative electrodes in Li-ion batteries*. Journal of Power Sources, 2014. **269**(Supplement C): p. 266-273.
35. Kwon, G.D., et al., *Graphene-Coated Aluminum Thin Film Anodes for Lithium-Ion Batteries*. ACS Applied Materials & Interfaces, 2018. **10**(35): p. 29486-29495.
36. Chang, X., et al., *Aluminum: An underappreciated anode material for lithium-ion batteries*. Energy Storage Materials, 2020. **25**: p. 93-99.
37. Sharma, S.K., et al., *Al nanorod thin films as anode electrode for Li ion rechargeable batteries*. Electrochimica Acta, 2013. **87**(Supplement C): p. 872-879.
38. Huang, T.S. and J.O. Brittain, *The mechanical behavior of β-LiAl*. Materials Science and Engineering, 1987. **93**: p. 93-97.
39. Baranski, A. and W. Fawcett, *The Formation of Lithium-Aluminum Alloys at an Aluminum Electrode in Propylene Carbonate*. Journal of The Electrochemical Society, 1982. **129**(5): p. 901-907.
40. Wen, C.J., *Thermodynamic and Mass Transport Properties of “LiAl”*. Journal of The Electrochemical Society, 1979. **126**(12): p. 2258.
41. Wen, C.J., et al., *Electrochemical investigation of solubility and chemical diffusion of lithium in aluminum*. Metallurgical Transactions B, 1980. **11**(1): p. 131-137.
42. Melendres, C.A., *Kinetics of electrochemical incorporation of lithium into aluminum*. Journal of The Electrochemical Society, 1977. **124**(5): p. 650-655.
43. McAlister, A., *The Al–Li (aluminum–lithium) system*. Bulletin of alloy phase diagrams, 1982. **3**(2): p. 177-183.
44. Murray, J.L., L.H. Bennett, and H. Baker, *Binary alloy phase diagrams*. Vol. 2. 1986: ASM International (OH).
45. Kishio, K. and J.O. Brittain, *Defect structure of β-LiAl*. Journal of Physics and Chemistry of Solids, 1979. **40**(12): p. 933-940.
46. Ou, X., et al., *Simultaneously pre-alloying and artificial solid electrolyte interface towards highly stable aluminum anode for high-performance Li hybrid capacitor*. Energy Storage Materials, 2020. **28**: p. 357-363.
47. Zheng, T., et al., *Sputtered Titanium Nitride Films on Titanium Foam Substrates as Electrodes for High-Power Electrochemical Capacitors*. ChemElectroChem, 2018. **5**(16): p. 2199-2207.
48. Yin, H., et al., *Faradaically selective membrane for liquid metal displacement batteries*. Nature Energy, 2018: p. 1.
49. Choi, Z., D. Kramer, and R. Mönig, *Correlation of stress and structural evolution in Li<sub>4</sub>Ti<sub>5</sub>O<sub>12</sub>-based electrodes for lithium ion batteries*. Journal of Power Sources, 2013. **240**: p.

- 245-251.
50. Zheng, T., et al., *Improvement of the Cycling Performance of Aluminum Anodes through Operando Light Microscopy and Kinetic Analysis*. ChemSusChem, 2020. **13**(5): p. 974-985.
  51. Deal, B.E. and A.S. Grove, *General Relationship for the Thermal Oxidation of Silicon*. Journal of Applied Physics, 1965. **36**(12): p. 3770-3778.
  52. Pharr, M., et al., *Kinetics of Initial Lithiation of Crystalline Silicon Electrodes of Lithium-Ion Batteries*. Nano Letters, 2012. **12**(9): p. 5039-5047.
  53. Carpio, R.A. and L.A. King, *Deposition and Dissolution of Lithium-Aluminum Alloy and Aluminum from Chloride-Saturated LiCl-AlCl<sub>3</sub> and NaCl-AlCl<sub>3</sub> Melts*. Journal of The Electrochemical Society, 1981. **128**(7): p. 1510-1517.
  54. Geronov, Y., P. Zlatilova, and R.V. Moshtev, *The secondary lithium—aluminium electrode at room temperature: I. Cycling in LiClO<sub>4</sub>—propylene carbonate solutions*. Journal of Power Sources, 1984. **12**(2): p. 145-153.
  55. Geronov, Y., P. Zlatilova, and G. Staikov, *The secondary lithium—aluminium electrode at room temperature: II. Kinetics of the electrochemical formation of the lithium—aluminium alloy*. Journal of Power Sources, 1984. **12**(2): p. 155-165.
  56. Geronov, Y., P. Zlatilova, and G. Staikov, *Electrochemical nucleation and growth of  $\beta$ -LiAl alloy in aprotic electrolyte solutions*. Electrochimica Acta, 1984. **29**(4): p. 551-555.
  57. Wood, K.N., et al., *Dendrites and Pits: Untangling the Complex Behavior of Lithium Metal Anodes through Operando Video Microscopy*. ACS Central Science, 2016. **2**(11): p. 790-801.
  58. Wood, K.N., M. Noked, and N.P. Dasgupta, *Lithium Metal Anodes: Toward an Improved Understanding of Coupled Morphological, Electrochemical, and Mechanical Behavior*. ACS Energy Letters, 2017. **2**(3): p. 664-672.
  59. Qin, B., et al., *Revisiting the Electrochemical Lithiation Mechanism of Aluminum and the Role of Li-rich Phases (Li<sub>1+x</sub>Al) on Capacity Fading*. ChemSusChem, 2019. **12**(12): p. 2609-2619.
  60. McAlister, A.J., *The Al–Li (Aluminum–Lithium) system*. Bulletin of Alloy Phase Diagrams, 1982. **3**(2): p. 177-183.
  61. Maskell, W. and J. Owen, *Cycling behavior of thin film LiAl electrodes with liquid and solid electrolytes*. Journal of The Electrochemical Society, 1985. **132**(7): p. 1602-1607.
  62. Rao, B., R. Francis, and H. Christopher, *Lithium-aluminum electrode*. Journal of The Electrochemical Society, 1977. **124**(10): p. 1490-1492.
  63. Bang, H.J., S. Kim, and J. Prakash, *Electrochemical investigations of lithium-aluminum alloy anode in Li/polymer cells*. Journal of Power Sources, 2001. **92**(1): p. 45-49.
  64. Leite, M.S., et al., *Insights into capacity loss mechanisms of all-solid-state Li-ion batteries with Al anodes*. Journal of Materials Chemistry A, 2014. **2**(48): p. 20552-20559.
  65. Gooranorimi, O. and A. Ghahremaninezhad, *Investigating surface morphology and cracking during lithiation of Al anodes*. AIMS Materials Science, 2016. **3**(4): p. 1632-1648.
  66. Machill, S. and D. Rahner, *In situ electrochemical characterization of lithium-alloying materials for rechargeable anodes in lithium batteries*. Journal of Power Sources, 1995. **54**(2): p. 428-432.
  67. Jow, T. and C. Liang, *Lithium-Aluminum Electrodes at Ambient Temperatures*. Journal of The Electrochemical Society, 1982. **129**(7): p. 1429-1434.
  68. Wen, C.J., et al., *Thermodynamic and mass transport properties of “LiAl”*. Journal of The Electrochemical Society, 1979. **126**(12): p. 2258-2266.
  69. Avrami, M., *Kinetics of Phase Change. I General Theory*. The Journal of Chemical Physics, 1939. **7**(12): p. 1103-1112.
  70. Avrami, M., *Kinetics of Phase Change. II Transformation-Time Relations for Random Distribution of Nuclei*. The Journal of Chemical Physics, 1940. **8**(2): p. 212-224.
  71. Avrami, M., *Granulation, Phase Change, and Microstructure Kinetics of Phase Change. III*. The Journal of Chemical Physics, 1941. **9**(2): p. 177-184.
  72. Pang, E.L., et al., *Modeling interface-controlled phase transformation kinetics in thin films*. Journal of Applied Physics, 2015. **117**(17): p. 175304.
  73. Očenášek, J., P. Novák, and S. Agbo, *Finite-thickness effect on crystallization kinetics in thin films and its adaptation in the Johnson–Mehl–Avrami–Kolmogorov model*. Journal of Applied

- Physics, 2014. **115**(4): p. 043505.
74. Ruitenbergh, G., A.K. Petford-Long, and R.C. Doole, *Determination of the isothermal nucleation and growth parameters for the crystallization of thin Ge<sub>2</sub>Sb<sub>2</sub>Te<sub>5</sub> films*. Journal of Applied Physics, 2002. **92**(6): p. 3116-3123.
  75. Allen, J.L., T.R. Jow, and J. Wolfenstine, *Kinetic Study of the Electrochemical FePO<sub>4</sub> to LiFePO<sub>4</sub> Phase Transition*. Chemistry of Materials, 2007. **19**(8): p. 2108-2111.
  76. Allen, J.L., T.R. Jow, and J. Wolfenstine, *Analysis of the FePO<sub>4</sub> to LiFePO<sub>4</sub> phase transition*. Journal of Solid State Electrochemistry, 2008. **12**(7): p. 1031-1033.
  77. Liu, X.H., et al., *Ultrafast Electrochemical Lithiation of Individual Si Nanowire Anodes*. Nano Letters, 2011. **11**(6): p. 2251-2258.
  78. Zhong, H., et al., *Conformation of lithium-aluminium alloy interphase-layer on lithium metal anode used for solid state batteries*. Electrochimica Acta, 2018. **277**: p. 268-275.
  79. Ichitsubo, T., et al., *Influence of mechanical strain on the electrochemical lithiation of aluminum-based electrode materials*. Journal of The Electrochemical Society, 2011. **159**(1): p. A14-A17.
  80. Hudak, N. and D. Huber, *Nanostructured lithium-aluminum alloy electrodes for lithium-ion batteries*. ECS Transactions, 2011. **33**(24): p. 1-13.
  81. Zheng, T., et al., *Granular phase transformation of polycrystalline aluminum during electrochemical lithiation*. Scripta Materialia, 2020. **188**: p. 164-168.
  82. Lee, S.W., et al., *Anomalous Shape Changes of Silicon Nanopillars by Electrochemical Lithiation*. Nano Letters, 2011. **11**(7): p. 3034-3039.
  83. Goldman, J.L., et al., *Strain Anisotropies and Self-Limiting Capacities in Single-Crystalline 3D Silicon Microstructures: Models for High Energy Density Lithium-Ion Battery Anodes*. Advanced Functional Materials, 2011. **21**(13): p. 2412-2422.
  84. Szilagy, A., *Twinning and nonlinear optics*. 1984, Massachusetts Institute of Technology.
  85. Thompson, C., *Secondary grain growth in thin films of semiconductors: Theoretical aspects*. Journal of applied physics, 1985. **58**(2): p. 763-772.
  86. Thornton, J.A., *High rate thick film growth*. Annual review of materials science, 1977. **7**(1): p. 239-260.
  87. Thompson, C.V. and R. Carel, *Stress and grain growth in thin films*. Journal of the Mechanics and Physics of Solids, 1996. **44**(5): p. 657-673.
  88. Thompson, C.V., *Structure Evolution During Processing of Polycrystalline Films*. Annual Review of Materials Science, 2000. **30**(1): p. 159-190.
  89. Kumagai, N., Y. Kikuchi, and K. Tanno, *Cycling behaviour of lithium-aluminium alloys formed on various aluminium substrates as negative electrodes in secondary lithium cells*. Journal of Applied Electrochemistry, 1992. **22**(7): p. 620-627.
  90. Yao, N., L. Heredy, and R. Saunders, *Emf Measurements of Electrochemically Prepared Lithium-Aluminum Alloy*. Journal of The Electrochemical Society, 1971. **118**(7): p. 1039-1042.
  91. Porter, D.A., K.E. Easterling, and M. Sherif, *Phase Transformations in Metals and Alloys, (Revised Reprint)*. 2009: CRC press.
  92. McDowell, M.T., et al., *25th Anniversary Article: Understanding the Lithiation of Silicon and Other Alloying Anodes for Lithium-Ion Batteries*. 2013. **25**(36): p. 4966-4985.
  93. Ziegenhain, G., H.M. Urbassek, and A. Hartmaier, *Influence of crystal anisotropy on elastic deformation and onset of plasticity in nanoindentation: A simulational study*. 2010. **107**(6): p. 061807.
  94. Spigarelli, S. and R. Sandström, *Basic creep modelling of aluminium*. Materials Science and Engineering: A, 2018. **711**: p. 343-349.
  95. Li, H., et al., *Circumventing huge volume strain in alloy anodes of lithium batteries*. Nature Communications, 2020. **11**(1): p. 1584.
  96. Zheng, T., et al., *Exploring the Reversibility of Phase Transformations in Aluminum Anodes through Operando Light Microscopy and Stress Analysis*. ChemSusChem, 2020. **13**(22): p. 5910-5920.
  97. Al-Obeidi, A., et al., *Mechanical measurements on lithium phosphorous oxynitride coated silicon thin film electrodes for lithium-ion batteries during lithiation and delithiation*. Applied

- Physics Letters, 2016. **109**(7): p. 071902.
98. Al-Obeidi, A., et al., *Mechanical stresses and morphology evolution in germanium thin film electrodes during lithiation and delithiation*. Journal of Power Sources, 2015. **297**: p. 472-480.
  99. Ghavidel, M.Z., et al., *Electrochemical Formation of Four Al-Li Phases ( $\beta$ -AlLi, Al<sub>2</sub>Li<sub>3</sub>, AlLi<sub>2-x</sub>, Al<sub>4</sub>Li<sub>9</sub>) at Intermediate Temperatures*. 2019. **166**(16): p. A4034-A4040.
  100. Erlebacher, J., et al., *Evolution of nanoporosity in dealloying*. Nature, 2001. **410**(6827): p. 450-453.
  101. Weissmüller, J. and K. Sieradzki, *Dealloyed nanoporous materials with interface-controlled behavior*. MRS Bulletin, 2018. **43**(1): p. 14-19.
  102. Rösner, H., et al., *Reconstructing a Nanoporous Metal in Three Dimensions: An Electron Tomography Study of Dealloyed Gold Leaf*. Advanced Engineering Materials, 2007. **9**(7): p. 535-541.
  103. Chen, Q. and K. Sieradzki, *Spontaneous evolution of bicontinuous nanostructures in dealloyed Li-based systems*. Nature Materials, 2013. **12**: p. 1102.
  104. Li, R. and K. Sieradzki, *Ductile-brittle transition in random porous Au*. Physical Review Letters, 1992. **68**(8): p. 1168-1171.
  105. Badwe, N., X. Chen, and K. Sieradzki, *Mechanical properties of nanoporous gold in tension*. Acta Materialia, 2017. **129**: p. 251-258.
  106. Boles, S.T. and M.H. Tahmasebi, *Are Foils the Future of Anodes?* Joule, 2020. **4**(7): p. 1342-1346.
  107. Gogotsi, Y. and P. Simon, *True Performance Metrics in Electrochemical Energy Storage*. Science, 2011. **334**(6058): p. 917.
  108. Wen, C.J., et al., *Use of electrochemical methods to determine chemical-diffusion coefficients in alloys: application to 'LiAl'*. International Metals Reviews, 1981. **26**(1): p. 253-268.
  109. Cucinotta, C.S., et al., *Superionic Conduction in Substoichiometric LiAl Alloy: An Ab Initio Study*. Physical Review Letters, 2009. **103**(12): p. 125901.
  110. Tokuhito, T., et al., *<sup>7</sup>Li NMR Relaxation in Supreionic  $\beta$ -Lithium Aluminum*. Journal of the Physical Society of Japan, 1989. **58**(7): p. 2553-2569.
  111. *Driving Forces and Fluxed For Diffusion*, in *Kinetics of Materials*. 2005. p. 41-76.
  112. Qin, B., et al., *Enabling Reversible (De)Lithiation of Aluminum by using Bis(fluorosulfonyl)imide-Based Electrolytes*. ChemSusChem, 2019. **12**(1): p. 208-212.
  113. Chan, A.K., et al., *Concentrated Electrolytes for Enhanced Stability of Al-Alloy Negative Electrodes in Li-Ion Batteries*. Journal of The Electrochemical Society, 2019. **166**(10): p. A1867-A1874.
  114. Zhang, M., et al., *Uniform Distribution of Alloying/Dealloying Stress for High Structural Stability of an Al Anode in High-Areal-Density Lithium-Ion Batteries*. Advanced Materials, 2019. **31**(18): p. 1900826.
  115. Aleshin, A.N., et al., *Kinetic properties of  $\langle 111 \rangle$  tilt boundaries in aluminium*. physica status solidi (a), 1978. **45**(1): p. 359-366.

# Appendix-I: Supporting Information of Chapter 3

## Supplementary Figures

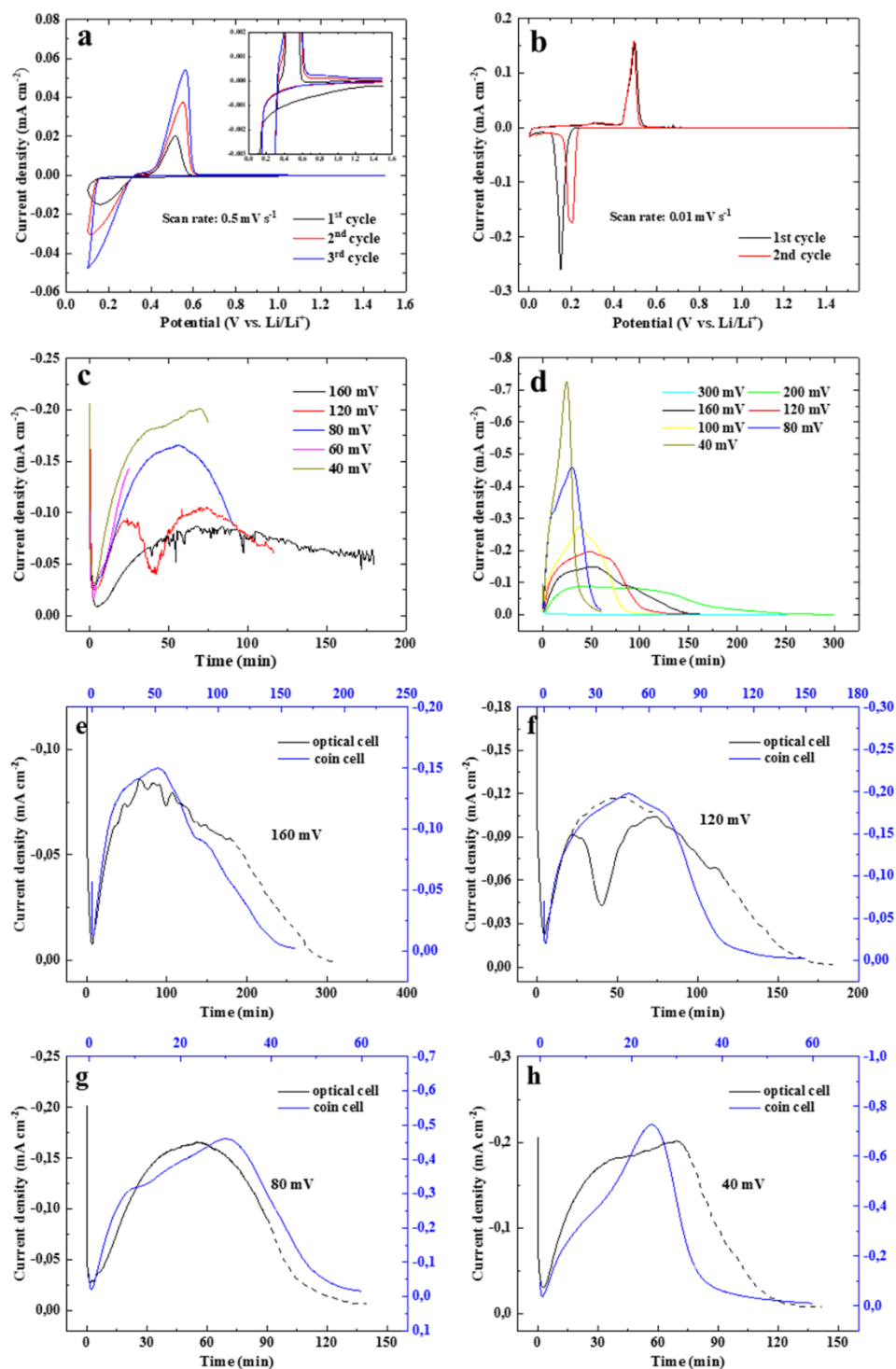


Figure S3.1. The cyclic voltammograms of (a) the optical cells (0.5 mV s<sup>-1</sup>) and (b) the coin cells (0.01 mV s<sup>-1</sup>); the systematic potentiostatic transients obtained from various applied

potentials used for analyzing the electrochemical incorporation of lithium into aluminum thin film in this study for (c) the optical cells and (d) the coin cells; (e-h) overlaid potentiostatic curves between the two cell geometries at various potentials, of which the shapes are identical. It should be mentioned that the kink of 120 mV of the optical cells of the potentiostatic tests were likely caused by an intermittent connection issue, but they do not affect the electrochemical analysis. The dashed lines are the prediction of the current response in potentiostatic transients.

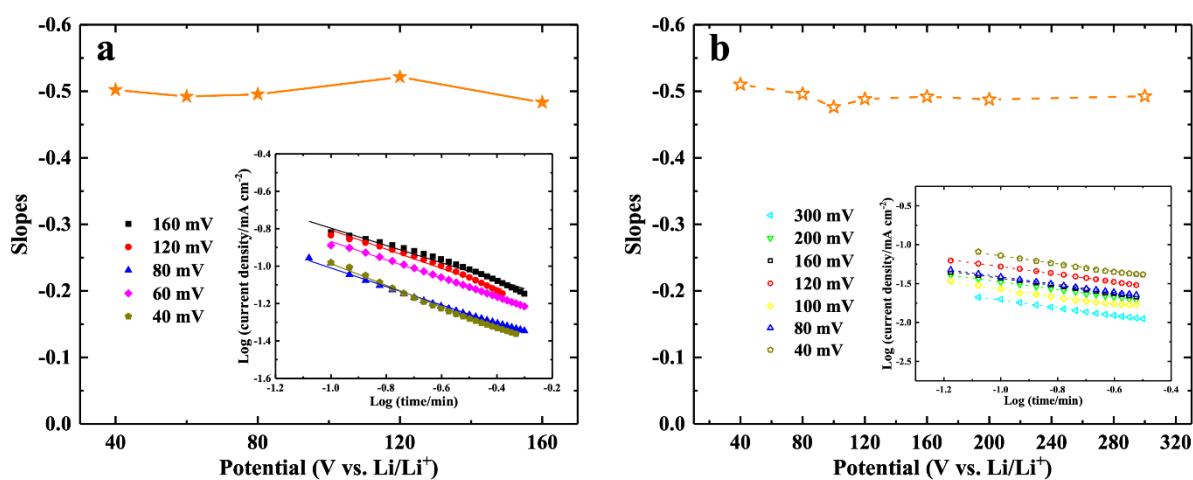


Figure S3.2. The logarithmic relations of current vs. time of the potentiostatic tests, of which the slopes are plotted against each applied potential for (a) optical cells and (b) coin cells during stage 1.

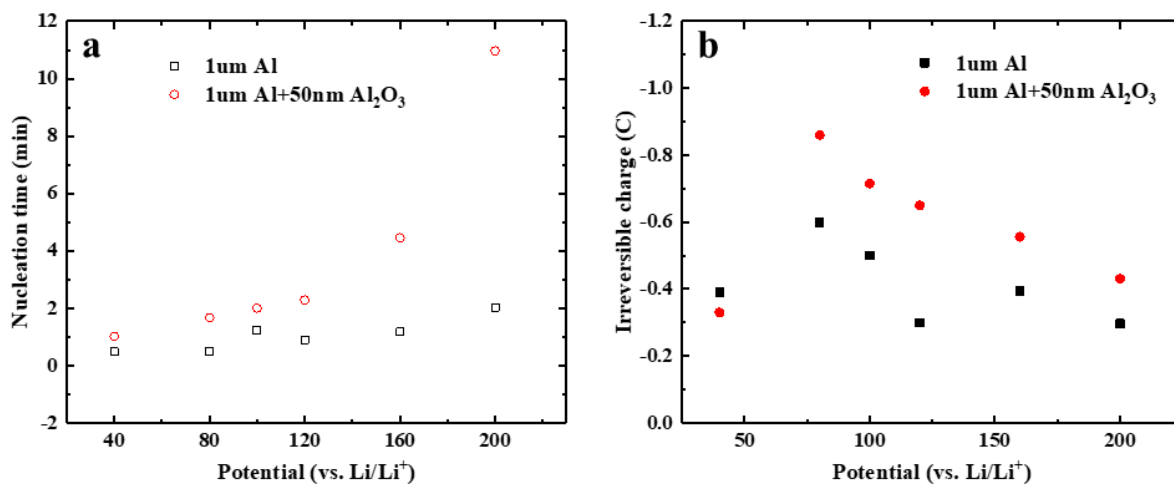


Figure S3.3. (a) The nucleation time required for Al thin films with and without ALD-coated Al<sub>2</sub>O<sub>3</sub> layer (50 nm), and (b) the irreversible charges of the initial cycle (lithiation charge minus delithiation charge), which represents the charges consumed for the Al<sub>2</sub>O<sub>3</sub> layer lithiation at various applied potential.

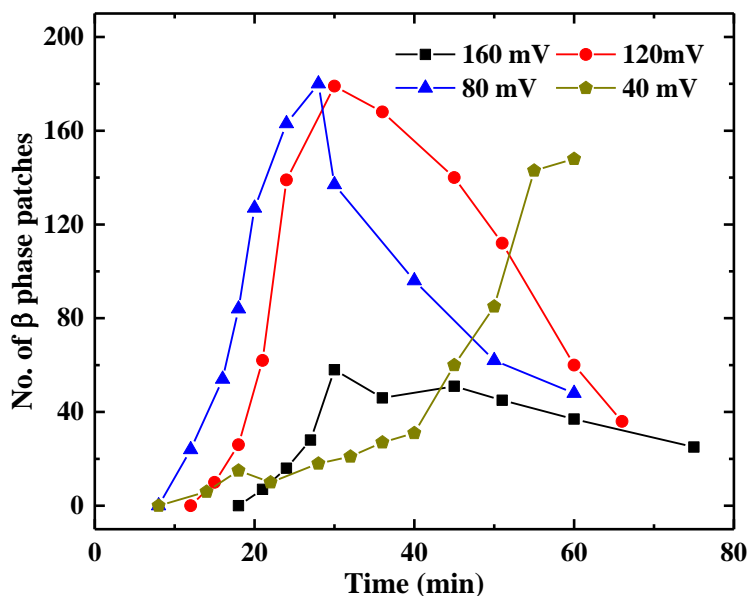


Figure S3.4. Number of the β phase patches within the observed region of the light microscope as a function of time at various applied potentials; the number of the β phase patches observed at 160 mV, 120 mV and 80 mV have a trend as expected: for a smaller voltage/larger overvoltage, the nucleation gets faster (both the times until the first nuclei and the time until a certain number of nuclei are observed gets smaller). Clearly, the nucleation rate at 120 mV is

higher than that at 160 mV, and it is likely that the nucleation rate at 80 mV is even higher, but the largest slope is obtained for 120 mV here, possibly because the  $\alpha$  phase area is getting smaller at a faster rate at 80 mV. At 40 mV, the nucleation rate is relatively small. This might be caused by a difference in the oxide layer thickness.

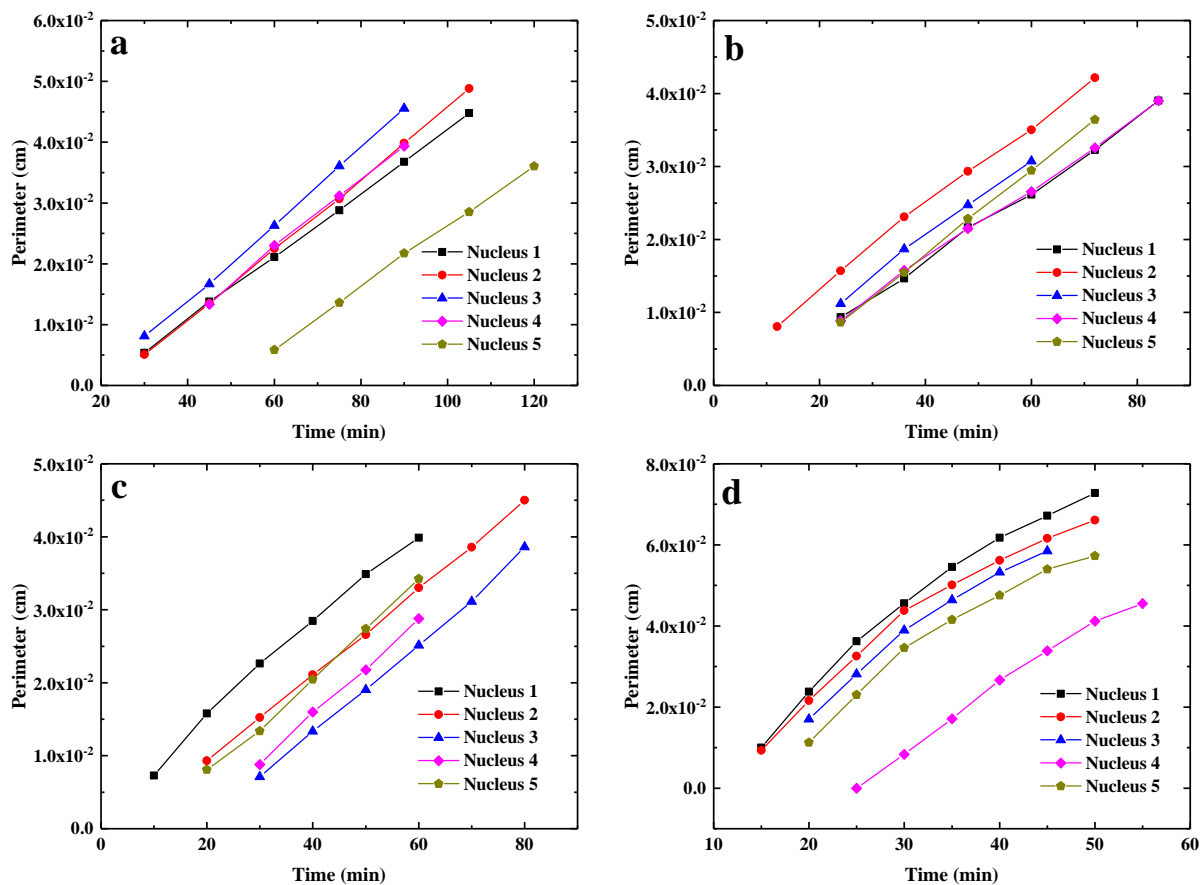


Figure S3.5. Perimeter vs. time relations of the  $\beta$  phase single patches under potentiostatic mode for (a) 160 mV, (b) 120 mV, (c) 80 mV and (d) 40 mV; 5 nuclei were randomly picked at different time points for the analysis

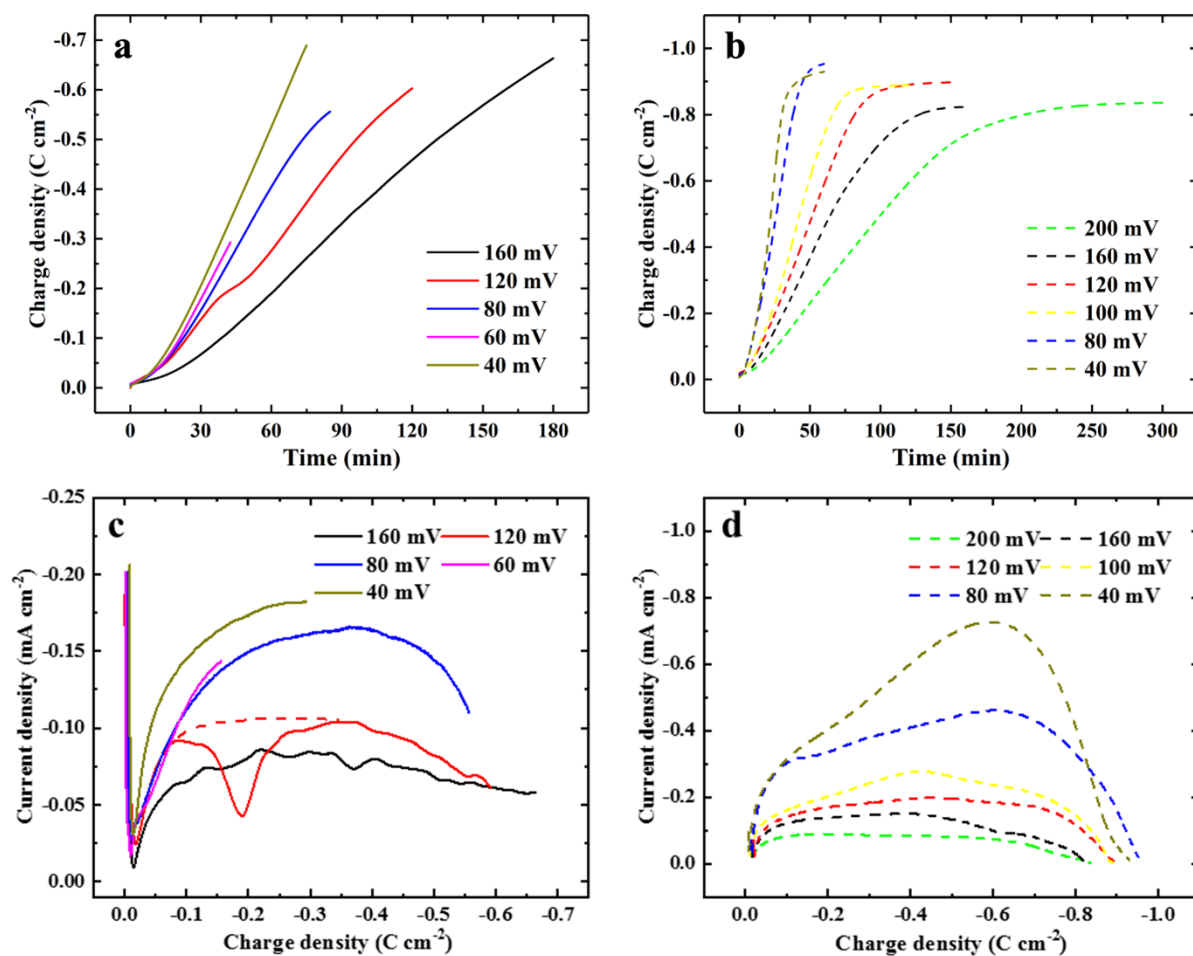


Figure S3.6. Charge density vs. time curves of (a) the optical cells and (b) the coin cells; current vs. charge density curves of (c) the optical cells and (d) the coin cells for electrochemical incorporation of Li into Al thin films at various potentials. It should be mentioned that the kink of 120 mV and the short duration of 60 mV of the optical cells were likely caused by an intermittent connection issue, but they do not affect the ongoing electrochemical analysis

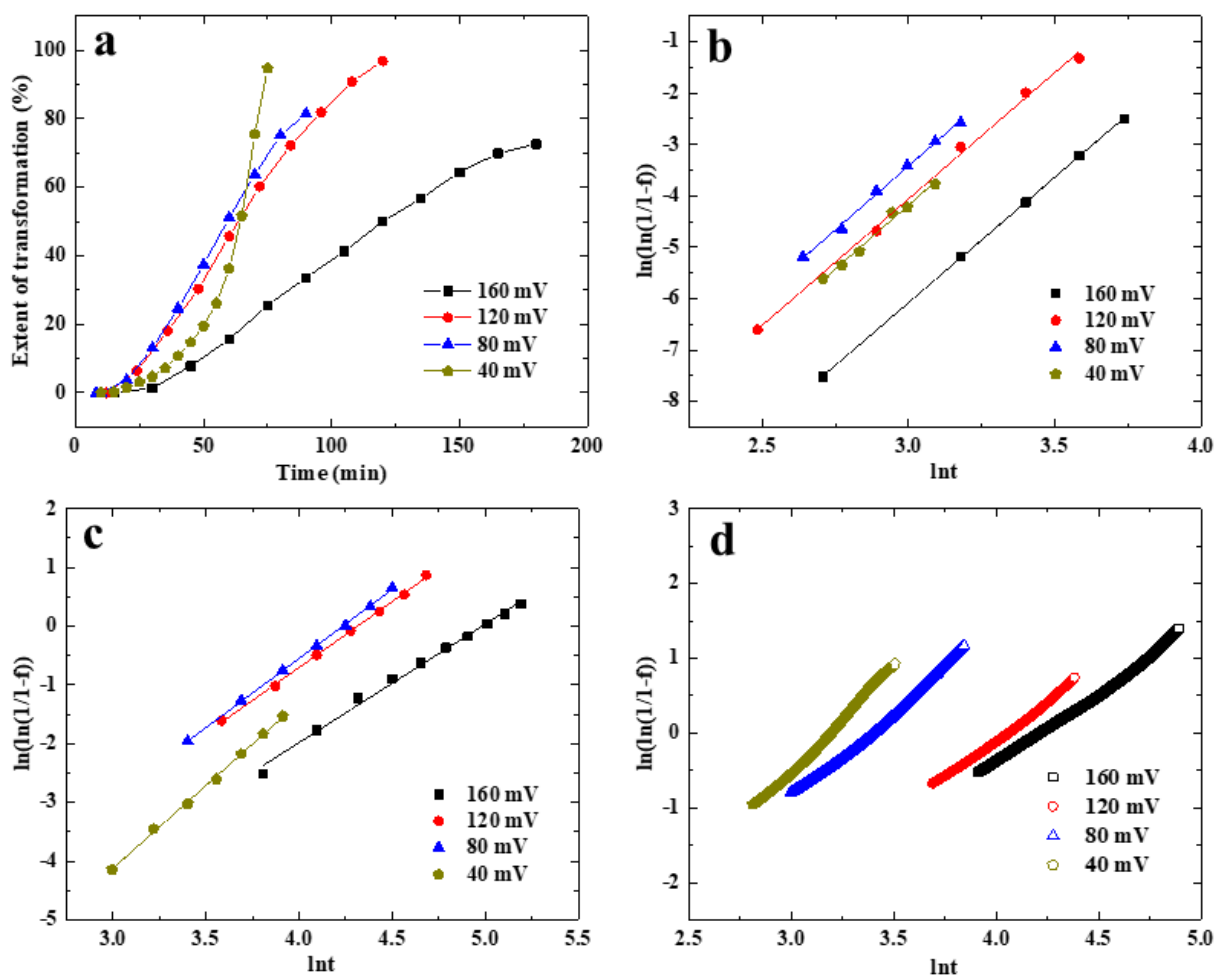


Figure S3.7. (a) the typical isothermal transformation plot measured from the *operando* images; (b) Avrami exponential analysis of the logarithm transformation for the two different linear regimes: (b) regime 1 and (c) regime 2; (d) the same analysis for coin cells using electrochemical data; the Avrami exponents ( $n$ ) are determined by the slopes at 160 mV, 120 mV, 80 mV, and 40 mV

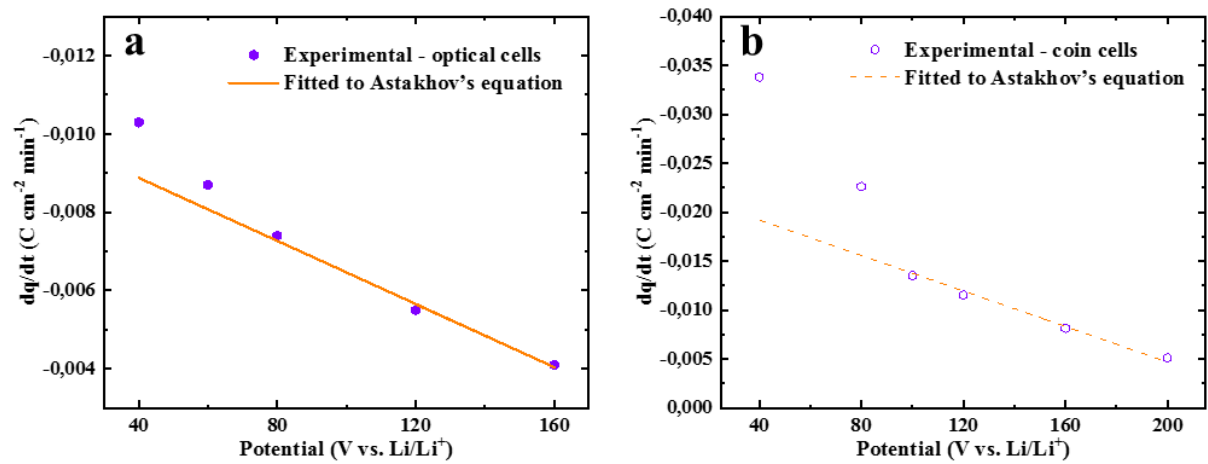


Figure S3.8. The experimental  $dq/dt$  rate and the data fitted by Astakhov's equation vs. the electrode potential during the formation of the  $\beta$ -phase  $LiAl$  for (a) optical cells and (b) coin cells

## Supplementary Tables

Table S3.1. The time required for the Al films in coin cells and in optical cells to be nucleated under various applied potentials

<b>Potential (mV)</b>	<b>Nucleation time (coin cell) (min)</b>	<b>Nucleation time (optical cell) (min)</b>
200	1.98	n/a
160	1.13	4.45
120	0.87	2.68
100	0.28	n/a
80	0.45	1.87
60	n/a	2.15
40	0.45	1.95

Table S3.2. The corresponding C rates of the plateau current during potentiostatic tests at different applied potentials

<b>Potential (mV)</b>	<b>Peak/plateau current (mA)</b>	<b>C rate</b>
200	~0.1-0.15	~C/5
160	~0.25-0.3	~C/2
120	~0.35-0.4	~C/1.5
100	~0.5	~1C
80	~0.9	~2C
40	~1.5	~3C

Table S3.3. The calculated slopes of the linear regime of the  $\Delta q/\Delta t$  relationships and the corresponding kinetic factors ( $L$ ) of the optical cells and the coin cells

<b>Potential (mV)</b>	<b><math>dq/dt</math> – coin cell (C cm<sup>-2</sup> min<sup>-1</sup>)</b>	<b><math>L_{\text{coin cell}}</math> (mol K V<sup>-1</sup> cm<sup>-2</sup> min<sup>-1</sup>)</b>	<b><math>dq/dt</math> – Optical cell (C cm<sup>-2</sup> min<sup>-1</sup>)</b>	<b><math>L_{\text{optical cell}}</math> (mol K V<sup>-1</sup> cm<sup>-2</sup> min<sup>-1</sup>)</b>
200	-0.0051	-0.00026	n/a	n/a
160	-0.0082	-0.00025	-0.0041	-0.000126
120	-0.0115	-0.00026	-0.0055	-0.000124
100	-0.0135	-0.00026	n/a	n/a
80	-0.0227	-0.00038	-0.0074	-0.000127
60	n/a	n/a	-0.0087	-0.000135
40	-0.0338	-0.00048	-0.00103	-0.000144

\*n/a – not applicable

### Astakhov's equation

Geronov et al. have reported Astakhov's equation and applied it to analyze the charge vs. time relationship of reaction-controlled electrochemical processes, reads

$$Q = \frac{L}{T} (RT \ln a_M^{z+} - zFE + \mu^0 - \mu) t, \quad (\text{S3.1})$$

where  $L$  is a kinetic factor,  $T$  is the cell temperature,  $R$  is the gas constant,  $a_M^{z+}$  is the activity of the ion in the electrolyte (here:  $\text{Li}^+$  with  $z = 1$ ),  $E$  is the applied potential,  $\mu^0$  and  $\mu$  are the chemical potentials of the new phase and the inserting metal, respectively.

If we assume that the transport in the electrolyte is so fast that changes in the electrolyte concentration can be neglected, the equation can be rewritten as:

$$Q = -\frac{LzF}{T} (E - E_{v=0}) t = -P \eta_p t, \quad (\text{S3.2})$$

with the parameter  $P = \frac{LzF}{T}$  and the overpotential  $\eta_p = E - E_{v=0}$ . At the potential  $E_{v=0}$ , the phase boundary does not move yet.  $E_{v=0}$  can be obtained from the plateau potential for the galvanostatic formation of the  $\beta$  phase by extrapolating it to zero current, it is ca. 0.26 V vs.  $\text{Li}/\text{Li}^+$ [24]. Above  $E_{v=0}$ , the phase transformation does not propagate. This can be supported by Figure S1c, which shows no phase transformation current at 300 mV vs.  $\text{Li}/\text{Li}^+$ .

Although the obtained kinetic factors ( $L$ ) are quite similar in the potential range from 160 mV to 80 mV for the optical cells and from 200 mV to 100 mV for the coin cells, the similarities do not hold if the applied potential approaches lower levels. The details are shown in Figure S3.8 and listed in Table S3.3. As can be noticed, the kinetic factor of the coin cells starts drifting when the applied potential is lower than 100 mV (80 mV for the optical cell), and all the  $L$  values are significantly larger than the ones obtained from the optical cells. This difference is probably resulted from the different cell architectures, of which the coin cells benefit from the commercially available assembly with minimized internal resistances.

Therefore, extra overpotentials are required in the case of optical cells to compensate for the relatively high resistance as well as the possible side reactions caused by the unique design.

Since our data can hardly agree with the Astakhov's equation, specifically at lower applied potentials (i.e. higher overpotentials), it highlights the necessity of using Avrami analysis for our thin film samples where 2D growth dominates the phase transition process. As for the analysis done by Geronov et al. that fits this Astakhov's equation well,[55] it can be explained by the bulk Al wires used in their study where the main growth mechanism is quasi 1D and the area of phase interface is constant.

## Avrami Analysis

The JMKA equation:[69-71]

$$f = 1 - \exp(-kt^n) \quad (\text{S3.3})$$

can be used then, e.g., by using the rearrangement of eq 4 which yields

$$\ln[-\ln(1-f)] = \ln(k) + n \ln(t), \quad (\text{S3.4})$$

where  $f$  is the volume fraction of  $\beta$ -phase LiAl, e.g., as measured from the *operando* images,  $t$  is the time after the potential jump,  $k$  is a rate constant parameter, and  $n$  is an exponential term that represents the geometry of the phase transition. The value of  $n$  is determined by elucidating the relationship between  $\ln[-\ln(1-f)]$  and  $\ln(t)$  which is expected to be linear, and the slope is considered as the Avrami exponent  $n$ . For  $n=1-2$ ,  $n=2-3$  and  $n=3-4$  the phase transformation occurs by 1D, 2D and 3D growth, respectively, with the lower values for the instantaneous nucleation and the higher values for progressive nucleation.[72]

By fitting the phase transformation data to Avrami equation, and a straight line should be expected. In fact, they seem to exhibit two different linearities as described in the main text. It can be seen from Figure S3.7b and S3.6c that the regime 1 is significantly shorter (less than 15 minutes) than the regime 2 (1-3 hours). However, the Avrami analysis of regime 1 yields exponential terms of close to 5, regardless of the applied potential, which already exceed the highest  $n=3-4$  described above.  $n=5$  can be explained by a  $t^3$ -dependence of the nucleation rate. Through a parabolic fitting between the  $\beta$  phase patch number and the corresponding time point, it is suggested that the nucleation rate is not constant and speeds up initially during this regime 1 (Figure S3.4). Subsequently, 2D growth is expected when the phase growth along z-axis is completed ( $\sim 1\mu\text{m}$ ). The 2D growth mechanism is caused by the thin film nature since the finite thickness causes a reduction of the Avrami exponent (from 3D to 2D).[72, 73] It should be noted that the electrochemical data of the optical cells are skipped here owing to the specific architecture that may accompany side reactions.

## Appendix II – Supporting Information of Chapter 4

### Supplementary Figures

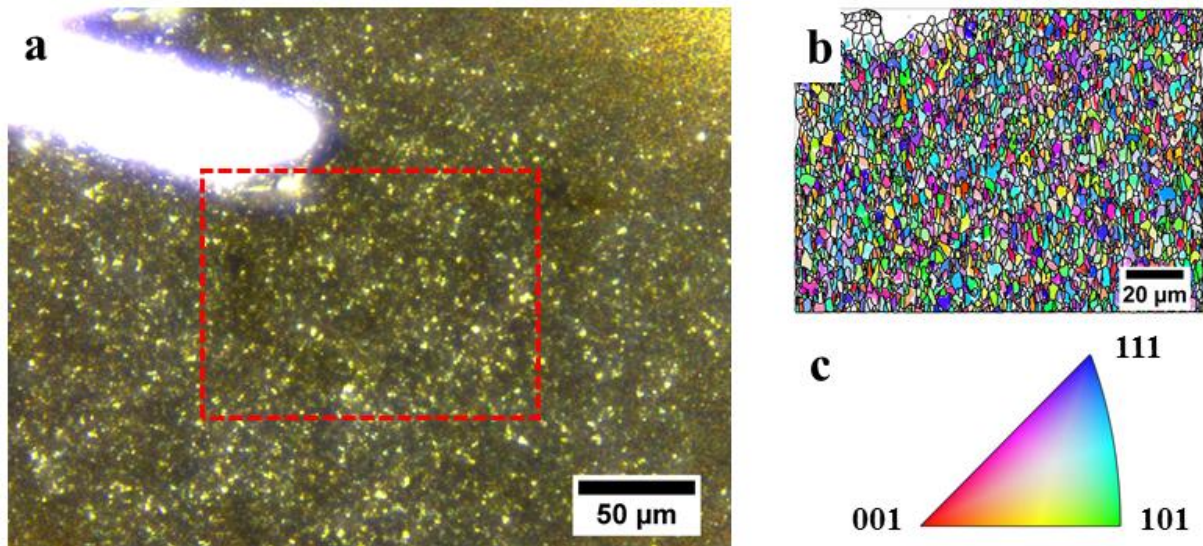


Figure S4.1. (a) a light microscopic image (400x) taken from the pristine surface of the Al thin films (red dashed circle) of the sample 2; (b) the corresponding EBSD crystallographic orientation map that represents the grain textures within the area highlighted by the red dashed rectangle; (c) the inverse pole figure (IPF) colour key.

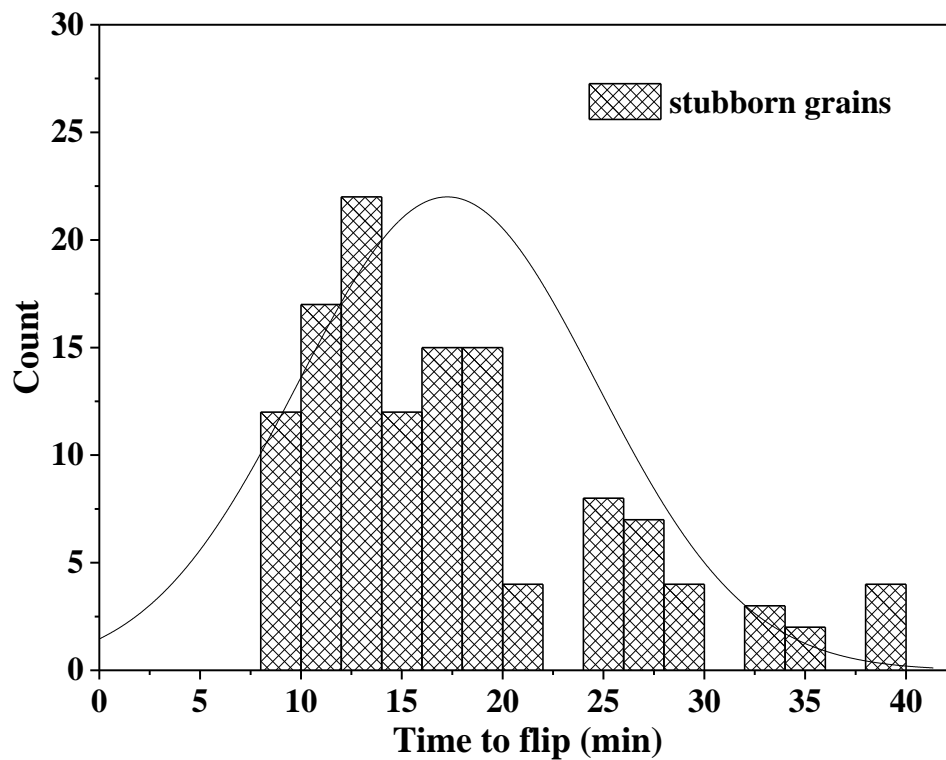


Figure S4.2. Histogram of the extra time required for all selected stubborn grains to be lithiated.

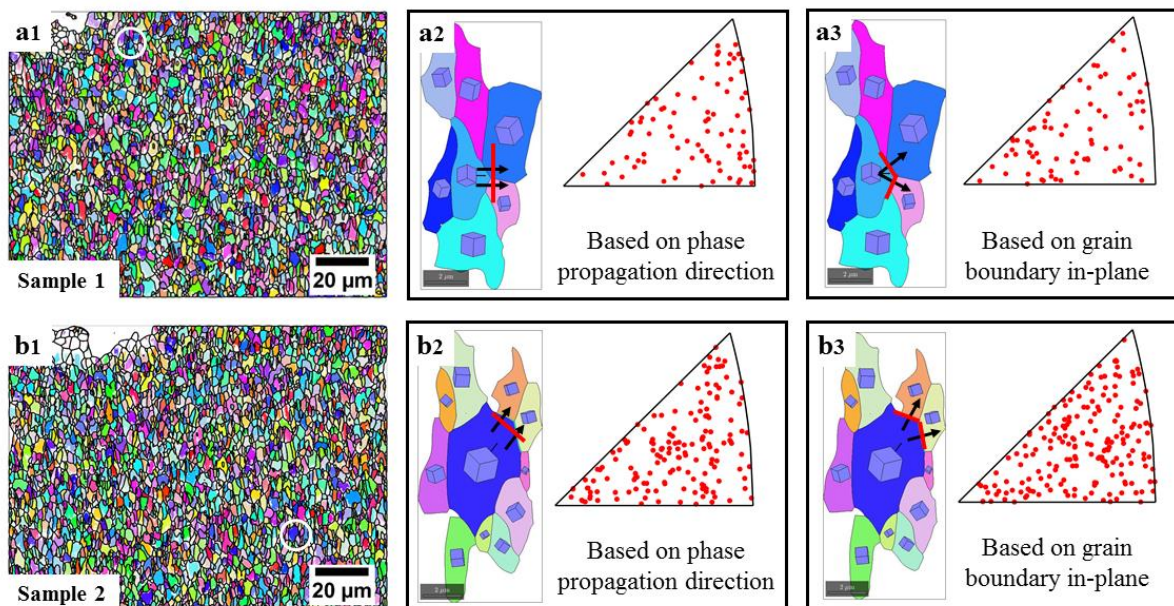


Figure S4.3. In-plane crystallographic orientations of the stubborn grains of sample 1 and sample 2, which exhibit randomness.

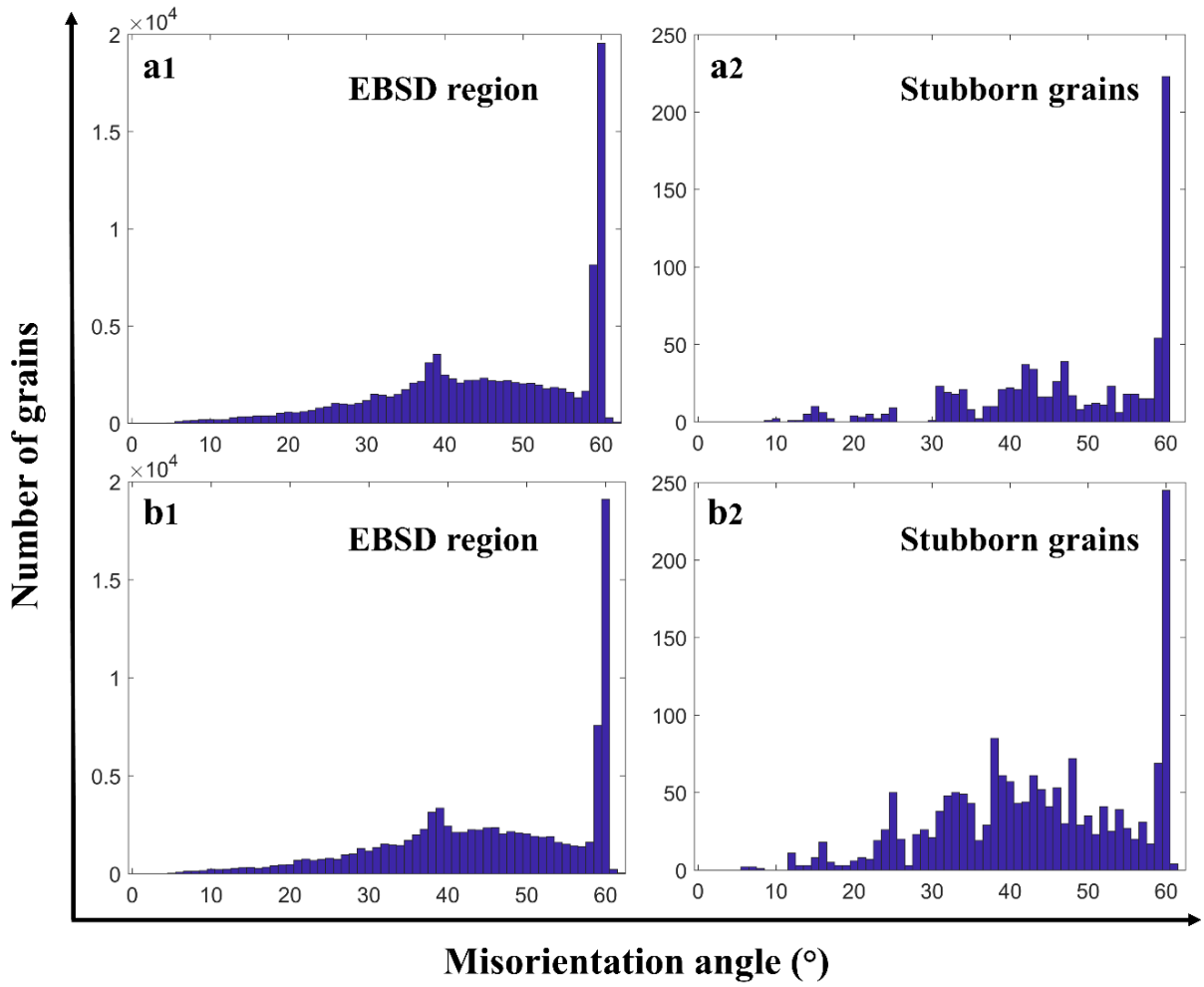
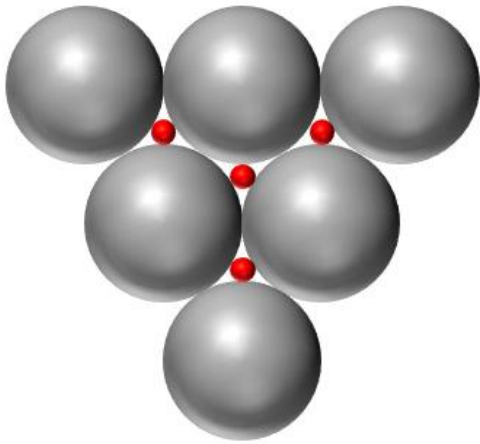
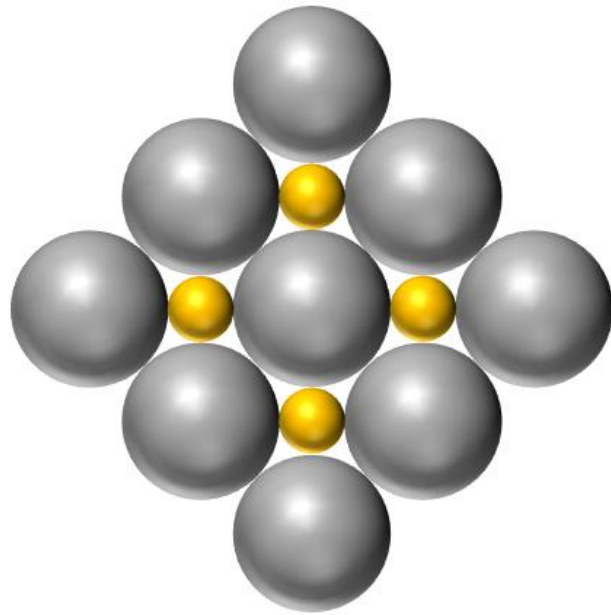


Figure S4.4. Distribution histograms of grain boundaries classified based on their misorientation angles of (a1, b1) the grains in the EBSD regions and (a2, b2) the selected stubborn grains for both samples.

● Al atom



**<111> plane**



**<100> plane**

Figure S4.5. Schematic overview of a  $\langle 111 \rangle$  plane and a  $\langle 100 \rangle$  plane of a fcc metal (Al in our case) with close-packing of equal spheres. The red and the yellow spheres indicate the space between the atoms within the given planes. Please note that the red spheres are within the  $\langle 111 \rangle$  plane and between three Al atoms, and not in the middle of the tetrahedral voids of the fcc structure.

## **In-plane orientation and grain boundaries**

Since the *operando* videos reveal that the  $\beta$  phase propagation occurs two-dimensionally (see the online version of [81]), it is reasonable then to speculate that the in-plane crystallinity and interfaces might matter during the lateral expansion. Therefore, the crystalline planes of the selected stubborn grains along the in-plane propagation directions in addition to the z-axis information were summarized in Figure S4.3, of which two sets of data have been achieved. The in-plane orientations of the stubborn grains have been extracted either directly based on the  $\beta$  phase propagation direction (Figure S4.3a2 and Figure S4.3b2) or on the grain boundaries perpendicular to its propagation route (Figure S4.3a3 and Figure S4.3b3). As can be seen, no preferred texture can be observed for those stubborn grains in both cases, indicating that the in-plane orientations of the grains do not significantly affect the phase propagation.

Although the grain boundaries did not seem to play a primary role based on the in-plane analysis, they are reported to be of vital importance in various structure formation processes, including diffusion, grain growth and recrystallization.[115] Therefore, the information of grain boundaries is also extracted for those selected stubborn grains from the EBSD analysis. Figure S4.4 illustrate the grain boundary character distribution in both samples as measured by means of EBSD. The grain boundary misorientation angle distribution is summarized in Figure S4.4a1 and Figure S4.4b1. Both histograms show that ~20% of the grain boundaries have a misorientation angle of  $60^\circ$  while most grains fall into the angle regime between  $30^\circ$  and  $60^\circ$ . Similarly, the distribution of misorientation angles among the selected stubborn grains is also plotted for comparisons. It can be seen that the histograms in Figure S4.4a2 and Figure S4.4b2 generally follow the same trend as the whole EBSD regions for both samples, suggesting that misorientation angles of the grain boundaries are likely not one of the decisive factors that affect the  $\alpha$  to  $\beta$  phase transformation in such a Li-Al system.

## Interatomic voids

As illustrated in Figure S4.5, one can estimate the space of the interatomic voids in a close-packing of equal spheres with a fcc lattice by using the following equations:

$$\text{For a } \langle 100 \rangle \text{ plane: } r_{\langle 100 \rangle} = (\sqrt{2} - 1)R \approx 0.414 R \quad (\text{S4.1})$$

$$\text{For a } \langle 111 \rangle \text{ plane: } r_{\langle 111 \rangle} = \left(\frac{2\sqrt{3}}{3} - 1\right)R \approx 0.155 R \quad (\text{S4.2})$$

Where  $R$  is the radius of the atoms and  $r$  is the radius of the voids between the atoms within the plane, indicated by the red and the yellow spheres in Figure S4.5.

For Al, the lattice parameter  $a$  is 404.95 pm, the resulting atomic radius is  $R = \frac{a}{2\sqrt{2}} = 143.17$  pm. Correspondingly,  $r_{\langle 100 \rangle} \approx 59$  pm and  $r_{\langle 111 \rangle} \approx 22$  pm. The ionic radius of  $\text{Li}^+$  might be as small as 59 pm for a coordination number of 4 and assuming an oxygen radius of 140 pm, but for a coordination number of 6, a  $\text{Li}^+$  radius of 0.90 pm has been published. Therefore, the Li ion does hardly fit into an octahedral void, and it is too large to pass through the  $r_{\langle 111 \rangle}$  voids between three Al atoms. In an fcc lattice, interstitial diffusion in all directions requires a passage through  $r_{\langle 111 \rangle}$  voids. Therefore, interstitial diffusion is not possible for Li in Al, and it occurs via voids in the Al lattice. This explains the low diffusion coefficient Li in the  $\alpha$  phase Al. Since the diffusion in the  $\alpha$  phase is slow compared to the propagation rate of the  $\alpha/\beta$  interface, it can be assumed that its influence on the kinetics of the process is negligible: The lithiation of the  $\alpha$  phase remains negligible, and practically all of the Li atoms required for the propagation are transported through the  $\beta$  phase or the  $\alpha/\beta$  interface, but not through the  $\alpha$  phase. Nevertheless, the size of voids may still affect the nucleation of the  $\beta$  phase, during which the Li ions from the electrolyte insert into the  $\alpha$ -Al fcc structure. In this process, the Li ions do not necessarily diffuse through an octahedral void. Therefore, the larger voids may effectively decrease the activation energy required for the nucleation of the  $\beta$  phase LiAl.

## Appendix III: Supporting Information of Chapter 5

### Supplementary Figures

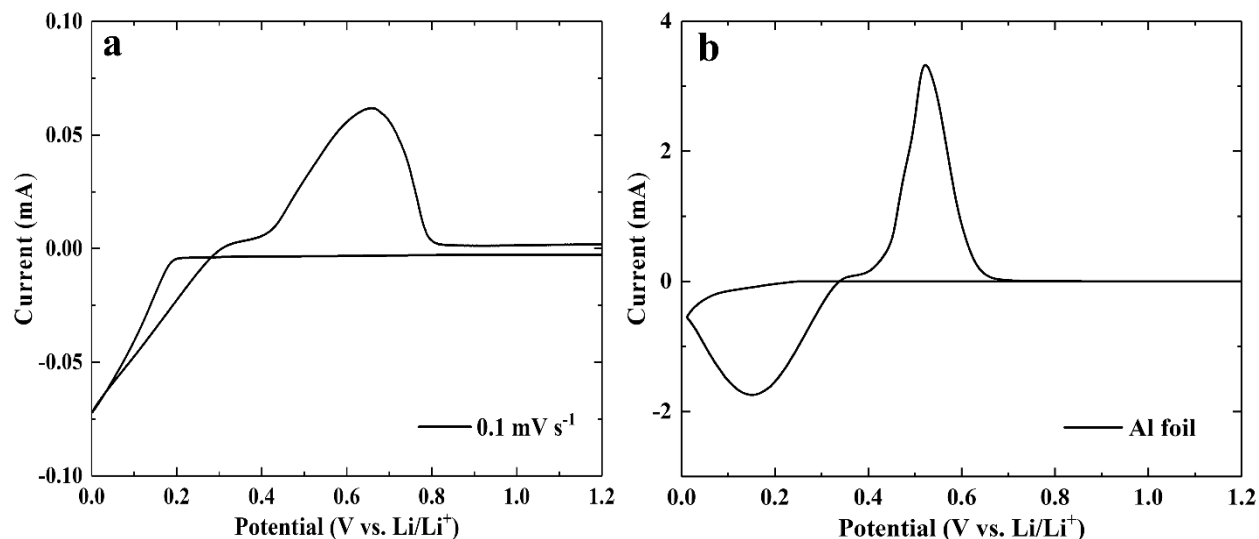


Figure S5.1. CV tests are done for (a) the same coin cell shown in Figure 1a of the manuscript, but with a ten times faster scan rate at 0.1 mV s<sup>-1</sup>, and for (b) CV test done for the same coin cell shown in Figure 1a of the manuscript, but with a piece of Al foil instead of a thin film. The scan rate was maintained at 0.01 mV s<sup>-1</sup>.

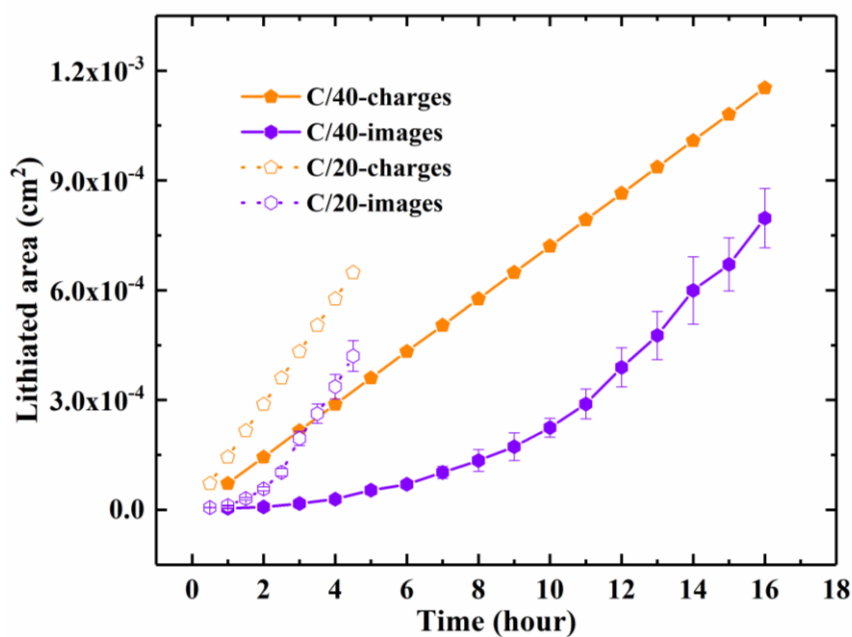


Figure S5.2. The total area (roughly proportional to the volume for the thin film geometry) of

the  $\beta$  phase patches was measured by manual evaluation of the images obtained during the first lithiation and plotted in conjunction with the estimated area calculated from electrical charges.

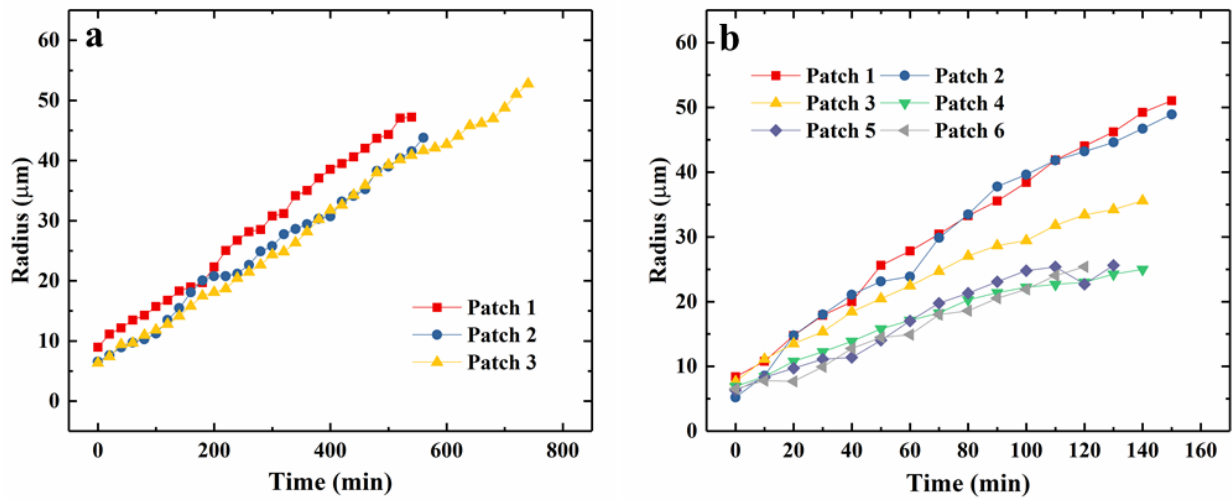


Figure S5.3. Radius vs. time relations of the  $\beta$  phase single patches under galvanostatic mode for (a) C/40 and (b) C/20. All available nuclei within the observed region were selected for the analysis.

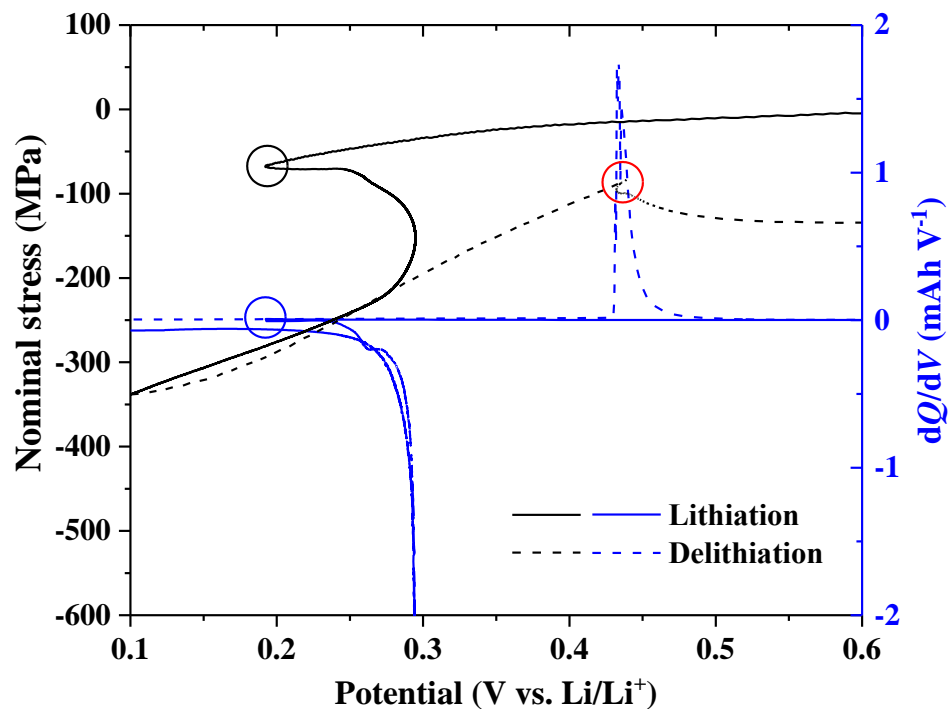


Figure S5.4. Incremental capacity analysis (ICA) for the second cycle.

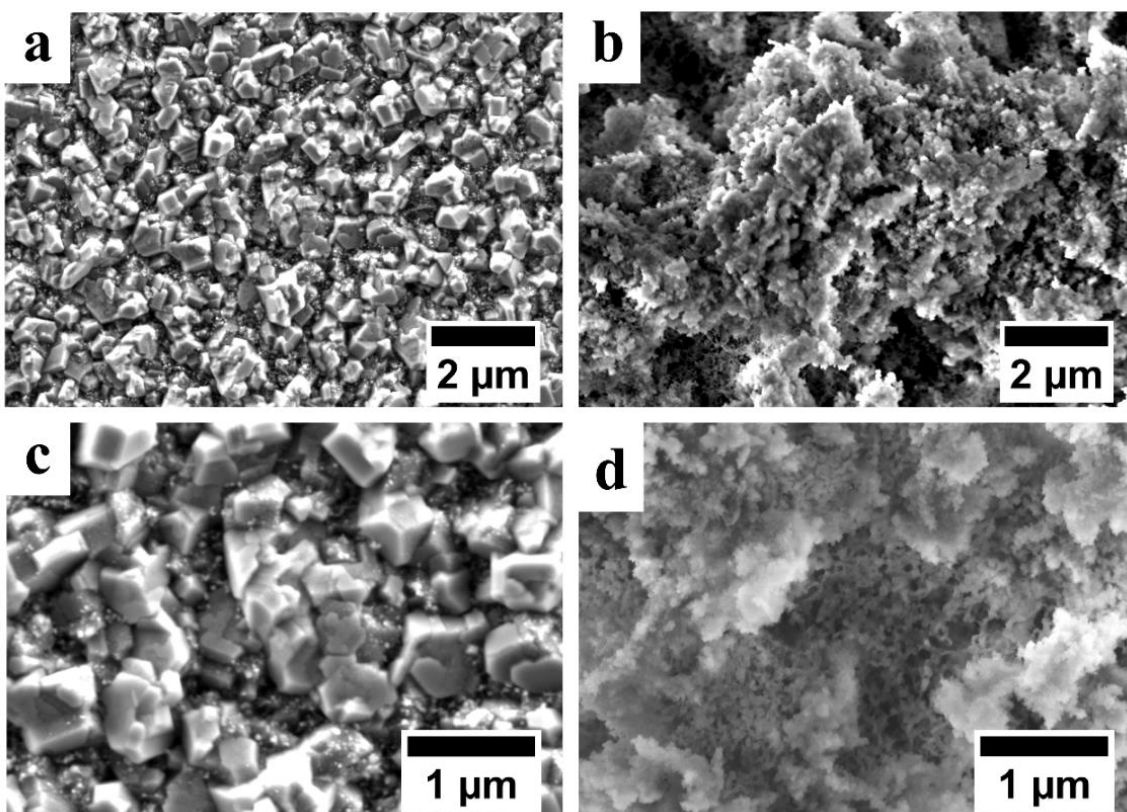


Figure S5.5. SEM images supplementing Figure 6 of the paper: the surface morphology of (a), (c) the pristine, and the cycled ( $\times 10$ ) cantilever.

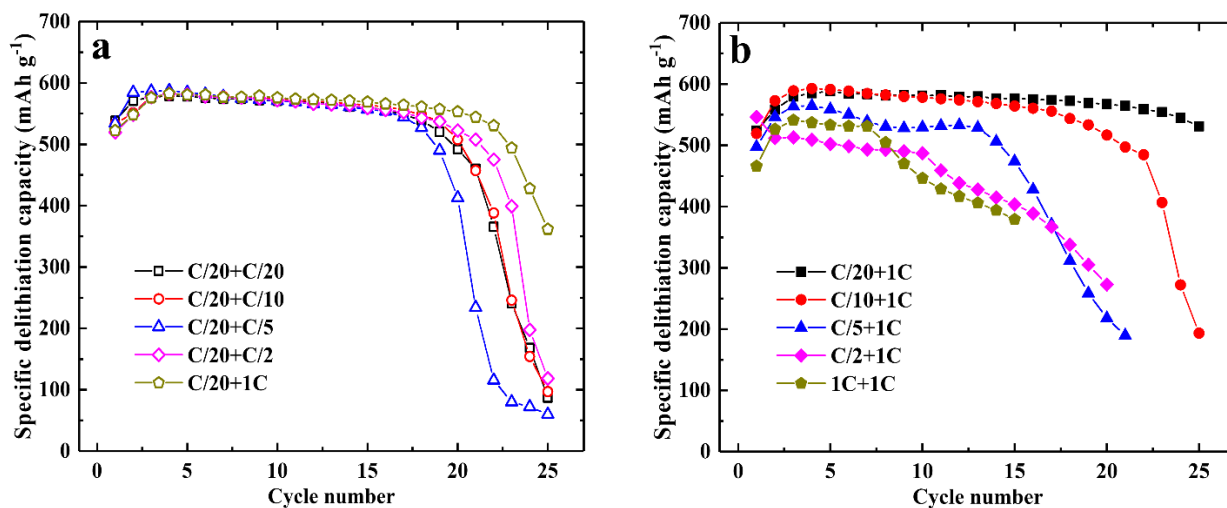


Figure S5.6. Galvanostatic cycling performances of Al thin film anodes obtained (a) at a fixed lithiation rate of C/20 coupled with various delithiation rates and (b) at various lithiation rates coupled with a fixed delithiation rate of 1C.

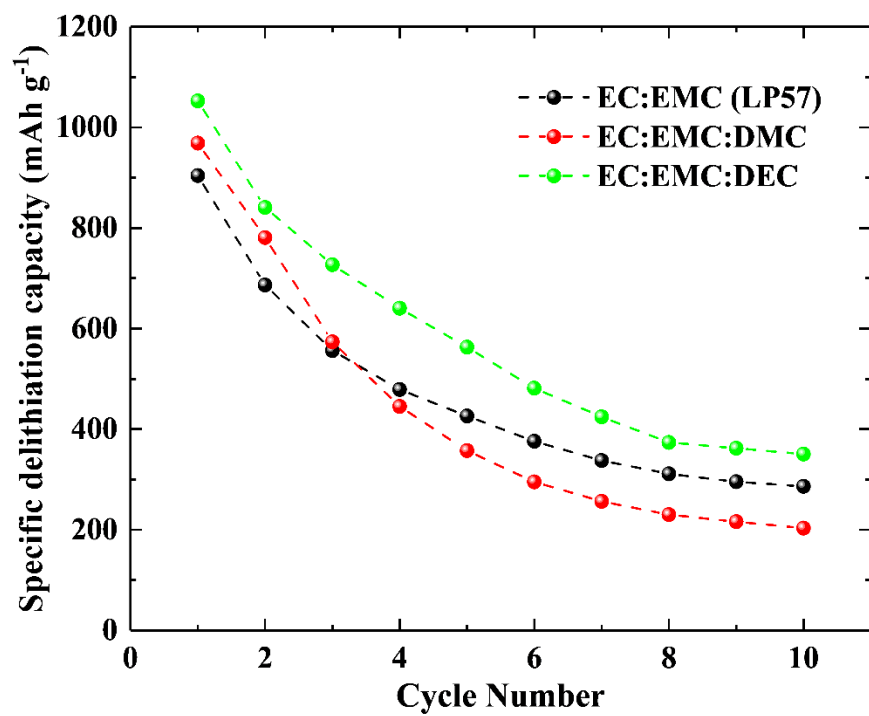


Figure S5.7. The cycling performance of Al thin films sputtered on Cu foil current collectors. The coin cells with Li metals as counter electrodes are used here to carry out the GCD cycling tests at C/20.

### Incremental Capacity Analysis (ICA)

As shown in Figure 5.5, the stress-potential curve exhibits a dip (black circle) before the compressive stress built-up, equivalent to the potential dip observed in the potential-capacity curve (i.e., nucleation potential). This nucleation is an almost instantaneous step that does not consume much of the electric charge (mostly SEI and/or oxides lithiation) and thus is revealed in the  $dQ/dV$  curve as a potential-jump from the open circuit to the nucleation ( $\sim 0.15$  V) indicated by the blue circle. Afterward, the mechanical stress is developing at a constant potential, corresponding to the lithiation plateau potential where the phase transformation occurs. Likewise, a sharp lithiation peak is also observed in the  $dQ/dV$  profile at  $\sim 0.27$  V.

In Figure 5.5b, for all cycles except the first one, noticeable compressive stress already starts accumulating prior to the nucleation of the  $\beta$  phase, coinciding with the abrupt stress drop at the beginning of the 2<sup>nd</sup> and the 3<sup>rd</sup> cycle in stress-capacity plot in Figure 5a (indicated by a dashed rectangle). This quick stress accumulation before nucleation is probably a result from (1) secondary SEI formation that comes from the surface area which is getting larger during each delithiation step, mainly related to newly formed nanoporosity, and from (2) reduction processes within the existing SEI which is partially oxidized during delithiation. Previous studies, including *ex-situ* SEM[32] and *operando* light microscopy,[50] points out the inhomogeneous distribution of the  $\beta$  phase, resulting in the insular patches surrounded by the  $\alpha$  phase. The ductility of Al may effectively accommodate some of the mechanical stresses developed from the volume expansion due to the Li insertion. The constant potential results in a perfectly straight stress profile versus potential in Figure 5.5c. After a complete cycle (i.e. for the second and the following cycles), however, the potential vs. time does not show a long flat plateau during lithiation (Figure 5.5b); correspondingly, the stress vs. potential in Figure S5.4 is curved and not a straight line anymore (Figure 5.5c). During the first cycle, overpotential is required for nucleation, which vanishes as soon as the nucleation has occurred and  $\alpha$  and  $\beta$

patches are in equilibrium. However, to move the phase boundary during the lithiation, an additional and a quite constant overpotential is required due to the mechanical work that must be done. In the second cycle, the maximum potential of the plateau is higher than that during the first cycle, i.e. the total overpotential is smaller. This might be related to smaller overpotentials caused by the porous structure which does not need the same amount of mechanical work to accommodate the expanding volume as the pristine bulk solid Al.

## Coin Cell Demonstration

A series of proof-of-concept experiments have been done using coin cells to assess how mechanical stress affects the cycling stability of Al anodes. The extent of lithiation (~55.6%) as same as the one used in the previous study is chosen, such that the generated data is comparable.[50] As demonstrated in Figure S5.6a, a C/20 lithiation rate combined with the delithiation rates that cover a whole range between C/20 and 1C all exhibit a similar cycling performance (i.e. no clear trend can be observed). As for lithiation, in agreement with the study mentioned, Figure S5.6b confirms that lithiation rates play a more crucial role in the cycling life of Al anodes. A simplified and clarified plot is made (Figure 5.8). A GCD rate of C/20 demonstrates similar cycling performance (~25 cycles) in comparison to that of C/20 lithiation plus 1C delithiation, supporting that the degradation mechanisms are not heavily dependent on the delithiation rate. However, if the lithiation rate is adjusted to match the 1C delithiation, the cell can only function for 15 cycles due to the mechanical effect 1 described in the article.

Information regarding mechanical effects is beneficial for understanding the origin of the capacity fading of Al-based anodes. Firstly, the lithiation rate is expected to be vital because it determines whether the generated stresses can be properly accommodated and/or released by the ductile Al when the two phases coexist. For high rates of lithiation, the large stresses cannot be released by Al deformation, and the fast volume changes result in mechanical defects like cracks. Secondly, the cracks observed for thin films (Figure 5.2) always form almost instantly after turning the current over (i.e., the beginning of delithiation) and cannot be avoided by slowing down the GCD rate to C/40. Therefore, the delithiation rate should not be as important as the lithiation one, since crack formation and delamination in thin film electrodes seem inevitable. Nevertheless, these degradation mechanisms might not be relevant for bulk Al electrodes (i.e., Al foils) where a rigid interface does not exist by omitting the usage of a Cu foil current collector.

## Appendix IV – Supporting Information of Chapter 7

### Supplementary Figures

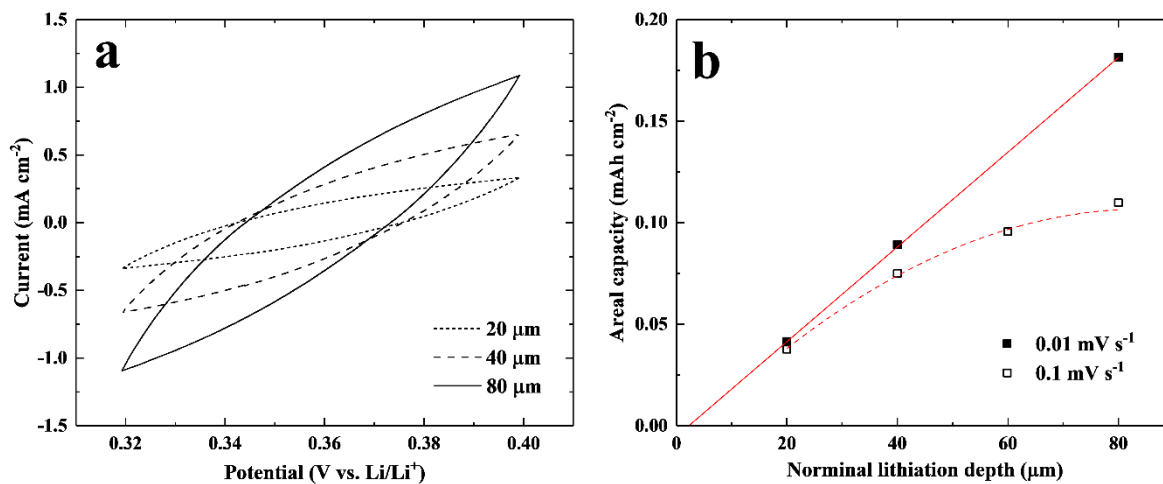


Figure S7.1. (a) The CV cycling ( $0.1 \text{ mV s}^{-1}$ ) within the determined Li solubility range while maintaining the  $\beta$ -LiAl structure for the Al foils with various nominal prelithiation depth. (b) The areal capacity integrated from the cyclic voltammograms as a function of the prelithiation depth.

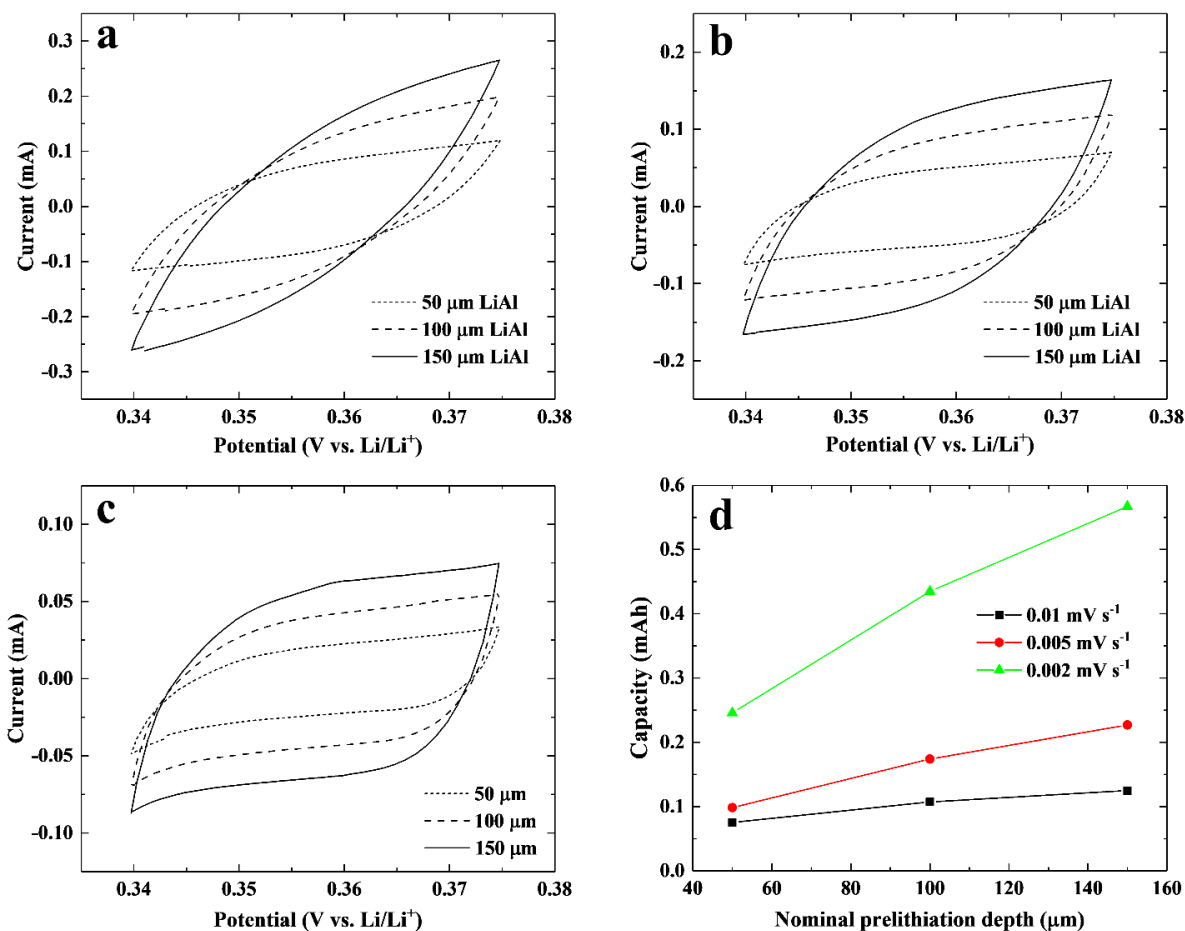


Figure S7.2. Cyclic voltammograms obtained from the Al foils with various prelithiation depths at the scan rate of (a)  $0.01 \text{ mV s}^{-1}$ , (b)  $0.005 \text{ mV s}^{-1}$ , and (c)  $0.002 \text{ mV s}^{-1}$ . (d) The capacities are calculated by integrating the CV areas and plotted against nominal lithiation depth.

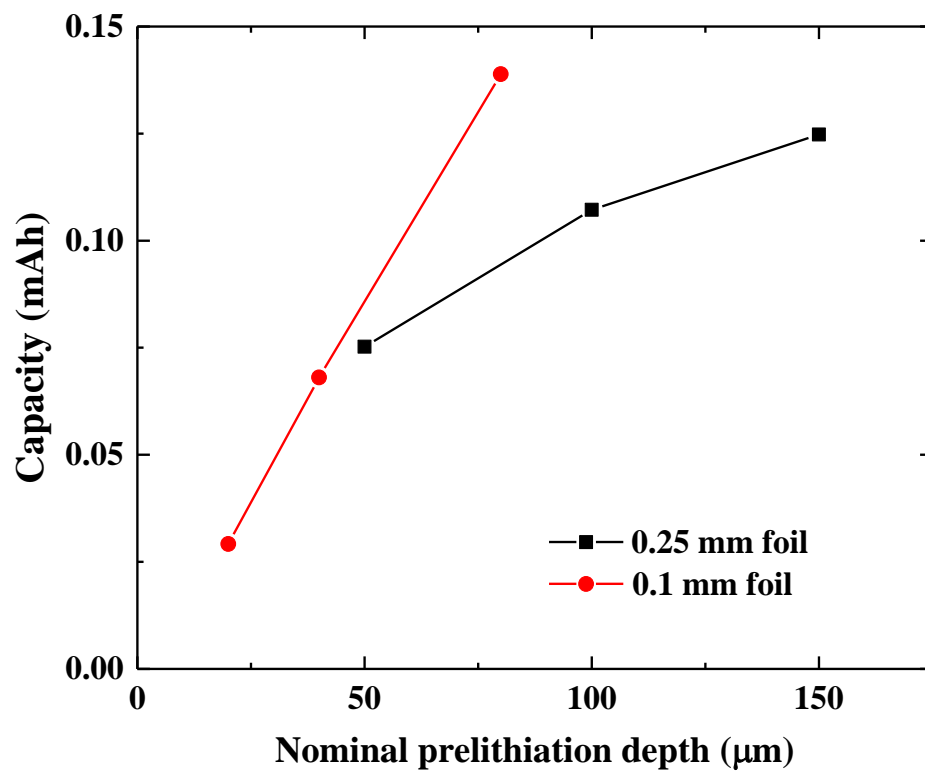


Figure S7.3. The capacities calculated from 0.1 mm and a 0.25 mm thick Al foil with various nominal prelithiation depths.